Die approbierte Originalversion dieser Diplom-/Masterarbeit ist in der Hauptbibliothek der Technischen Universität Wien aufgestellt und zugänglich.

http://www.ub.tuwien.ac.at

The approved original version of this diploma or master thesis is available at the main library of the Vienna University of Technology.

http://www.ub.tuwien.ac.at/eng

Unterschrift Betreuer

TECHNISCHE UNIVERSITÄT WIEN

DIPLOMARBEIT

Evaluation of Motion Compensation techniques for cardiac PET imaging

ausgeführt am Institut für Angewandte Physik (E 134)
der Technischen Universität Wien

in Zusammenarbeit mit dem

Zentrum für Medizinische Physik und Biomedizinische Technik
der Medizinischen Universität Wien

unter der Anleitung von

Ao.Univ.-Prof. DI Dr. Martin Gröschl
(Technische Universität Wien)

und
als verantwortlich mitwirkendem Universitätsassistenten

Jacobo Cal-González, PhD
(Center for Medical Physics and Biomedical Engineering)
(Medizinische Universität Wien)

durch

Alexader P. Berger
Linzerstraße 425
A-1140 Wien

Wien, 21. März 2018
Ort, Datum

Unterschrift Student

Abstract

Introduction: Positron Emission Tomography (PET) allows for high resolution 3D imaging of functional processes into the patient body. However, respiratory and cardiac motion of the patient impairs image quality of cardiac PET scans by motion-added blurring of the PET activity distribution in the heart. As a result, spatial resolution of PET images is reduced and quantitative measures are biased.

Aim: The study, conducted in this thesis, focuses on the comparative evaluation of the performance and accuracy of different Motion Compensation (MoCo) techniques in PET acquisitions with simulated respiratory and cardiac motion. The main focus was set on the performance of the following MoCo techniques: (1) Projection Based Motion Compensation (P-MoCo), which incorporates the motion-information before the image reconstruction, (2) Motion-Compensated Image Reconstruction (MCIR) in which the motion compensation is performed during the image reconstruction-process and (3) Reconstruct-Transform-Average (RTA) that incorporates it after image reconstruction, in PET acquisitions with respiratory and cardiac motion.

Materials and Methods: Different motion models, from simplistic 1D-axial motion to complex 3D cardio-respiratory motion models have been used in the simulations involving a Extended Cardiac-torso (XCAT) phantom as well as a numerical phantom consisting of a series of MR-based 4D PET/MR datasets. Furthermore, we included some preliminary evaluations of the performance of the MoCo approaches in four patient datasets acquired in a Biograph mMR PET/MR system. Signal-to-Noise Ratio (SNR), Contrast to Noise Ratio (CNR), Lesion to Background Ratio (L2B) ratio as well as Myocardium to Background Ratio (M2B) ratio were used as figures-of-merit to evaluate the performance of the MoCo approaches involving breakdown analysis, stability analysis and separability analysis.

Results: For XCAT Phantom data a direct comparison of the stability of performance of P-MoCo, MCIR and RTA throughout the full range of respiratory

motion complexity (1D-2D) was conducted, giving comparable absolute differences of $15 \cdot 10^{-3}$, $16 \cdot 10^{-3}$ and $19 \cdot 10^{-3}$ in terms of $M2Li_{1D}$ and $M2Li_{2D}$ for MCIR, RTA and P-MoCo. For the numerical phantom stability of the MoCo approaches was tested by means of total difference of LBR_{1D} and LBR_{3D} of $49 \cdot 10^{-3}$ for MCIR, of $72 \cdot 10^{-3}$ for RTA but of $497 \cdot 10^{-3}$ for P-MoCo, that cannot be compared to the latter two MoCo approaches. Unsurpassed performance of Gated reconstructions for both patient datasets including the tracers FDG and NH_3 were found. P-MoCo and RTA lead to an overall better image quality in terms of myocardium definition, M2B ratios as well as noise properties, than static OSEM reconstructions. Noise properties of the images were analysed leading to an on average 60 % higher noise in single gate reconstructions than in P-MoCo, RTA and static OSEM reconstructions.

Conclusion: The findings in this thesis highly suggest that P-MoCo is a good and useful tool for respiratory motion compensation, yielding to comparable results as approved methods like MCIR or RTA, but cannot handle complex motion like a mixture of respiratory and cardiac motion in two and three dimensions. Further, the findings suggest that P-MoCo is capable of reconstructing patient-data, yielding to comparable results as standard methods like RTA. According to the findings of the first datasets, the performance of P-MoCo may vary with different tracers.

Kurzfassung

Einleitung: Die in dieser Arbeit durchgeführte Studie konzentriert sich auf die vergleichende Bewertung der Leistung und Genauigkeit verschiedener Bewegungskompensationstechniken (MoCo-Techniken) bei PET-Aufnahmen mit simulierter Atmungs- und Herzbewegung. Der Hauptfokus lag auf der Durchführung und Leistungsevaluierung der folgenden MoCo-Techniken: (1) P-MoCo, die die Bewegungsinformation vor der Bildrekonstruktion einführt, (2) MCIR, in der die Bewegungskompensation während des Bildrekonstruktionsprozesses durchgeführt wird und (3) RTA, die die Bewegungsinformation nach der Bildrekonstruktion in das System einführt.

Materialien und Methoden: Verschiedene Bewegungsmodelle, startend von vereinfachten 1D-Axialbewegunsmodellen bis hin zu komplexen 3D-kardio- respiratorischen Bewegungsmodellen, wurden in den Simulationen mit einem XCAT Phantom sowie einem MR-basierten numerischen Phantom, bestehend aus einer Reihe an 4D PET/MR Datensätzen, verwendet. Darüber hinaus wurden einige vorläufige Leistungsevaluierungen der MoCo-Ansätze an vier Patientendatensätzen durchgeführt, die mittels eines Biograph mMR PET/MR-Systems aufgenommen wurden. Signal-Rausch-, Kontrast-Rausch-, Läsions-Hintergrund- sowie Myokard-Hintergrund-Verhältnis wurden als Leistungsmerkmale herangezogen, um die Leistung der MoCo-Ansätze mittels der Analyse von Zusammenbruch, Stabilität und Trennbarkeit umfassend zu bewerten sowie zu charakterisieren.

Ergebnisse: Für XCAT-Phantom-Daten wurde ein direkter Vergleich der Stabilität der Leistung von P-MoCo, MCIR und RTA über den gesamten Bereich der Atmungsbewegungskomplexität (1D-2D) durchgeführt, was vergleichbare absolute Unterschiede von $15 \cdot 10^{-3}$, $16 \cdot 10^{-3}$ und $19 \cdot 10^{-3}$ im Bezug auf $M2Li_{1D}$ und $M2Li_{2D}$ für MCIR, RTA und P-MoCo lieferte. Für das numerische Phantom wurde die Stabilität der MoCo-Ansätze mittels Totaldifferenz von LBR_{1D} und LBR_{3D} zu $49 \cdot 10^{-3}$ für MCIR, zu $72 \cdot 10^{-3}$ für RTA, aber zu $497 \cdot 10^{-3}$ für P-MoCo getestet, was nicht mit den beiden letztgenannten MoCo-Ansätzen verglichen werden kann. Weiters wurde eine unübertroffene Leistung von einzelnen Gated-Rekonstruktionen

für beide Patienten-Datensätze einschließlich der Tracer FDG und NH_3 gefunden. P-MoCo und RTA führten insgesamt zu einer besseren Bildqualität als statische OSEM-Rekonstruktionen, hinsichtlich der Myokarddefinition, M2B-Verhältnissen sowie Rauscheigenschaften. Die Rauscheigenschaften der Bilder wurden analysiert, was zu einem um 60 % höheren Rauschen bei Einzelgaterekonstruktionen führte als bei P-MoCo, RTA und statischen OSEM-Rekonstruktionen.

Fazit: Die Ergebnisse dieser Arbeit legen nahe, dass P-MoCo ein gutes und nützliches Werkzeug für die Atembewegungskompensation ist, die zu vergleichbaren Ergebnissen zugelassener Methoden wie MCIR oder RTA führt. P-MoCo kann jedoch komplexe Bewegungen, bestehend aus einer Mischung von Atmungs- und Herzbewegung in zwei und drei Dimensionen, nicht bewältigen. Darüber hinaus legen die Ergebnisse nahe, dass P-MoCo in der Lage ist, Patientendaten zu rekonstruieren, was zu vergleichbaren Ergebnissen anerkannter Methoden wie RTA führt. Ergebnisse der ersten Patienten-Datensätze legen nahe, dass die Leistung von P-MoCo mit verschiedenen Tracern variieren kann.

Acknowledgements

First of all, I want to thank my thesis advisors Martin Gröschl and Jacobo Cal-González, who gave me the opportunity of writing this thesis.

Moreover I want to thank Thomas Beyer for giving me the chance of working in the QIMP working group at the Center of Medical Physics and Biomedical Engineering at the Medical University of Vienna.

My honest thanks to Jacobo Cal-González who introduced me to this topic, proofread the whole thesis and was an extraordinarily helpful and cooperative source of expert knowledge.

Furthermore, I want to thank my colleagues from Technical Physics at TU Wien, my colleagues from Center of Medical Physics and Biomedical Engineering at the Medical University of Vienna for not only adding me in their working groups, but also giving me the feeling of being welcome and a friend.

Finally, I want to thank my family, especially my parents who offered me the chance to study physics, always providing me with unconditional patience and motivational force.

Special thanks to my girlfriend - not only for helping me with the design of some of the tables in this thesis - but also for her constant smiles, good mood, emotional support and encouraging words whenever I needed them.

Contents

List of figures **1**

List of tables **3**

List of abbreviations **4**

1 Introduction **6**

2 Theoretical Background and PET Principles **8**
2.1 PET Physics 8
2.1.1 Positron Emission and Annihilation 8
2.1.2 PET Radionuclides 11
2.1.3 Gamma Ray Interaction with Matter 13
2.1.4 PET detectors 15
2.1.5 Image Formation 19
2.2 Hybrid Technology 22
2.2.1 PET/CT System 22
2.2.2 PET/MR System 24
2.3 Image Reconstruction 24
2.3.1 Analytic Methods 24
2.3.2 Iterative Methods 26
2.4 Standard Data Corrections and Quantification 27
2.4.1 Attenuation 28
2.4.2 Scatter 28
2.4.3 Randoms 29
2.5 Motion Compensation 29
2.5.1 Motion Compensation Techniques 31
2.5.2 Projection-Based Motion Compensation 32
2.5.3 Motion Compensated Image Reconstruction 33
2.5.4 Reconstruct-Transform-Average 34

3 Methodology **36**
3.1 Biograph mMR 36
3.2 Motion Compensation Approaches 37
3.2.1 Projection-Based Motion Compensation 38

3.2.2 Motion Compensated Image Reconstruction . . . 39
3.2.3 Reconstruct-Transform-Average . . . 39
3.3 Phantom Data . . . 40
3.3.1 XCAT Phantom . . . 41
3.3.2 Numerical Phantom . . . 42
3.4 Image Quality Analysis . . . 44
3.4.1 Bias-Analysis . . . 44
3.4.2 Breakdown-Analysis . . . 45
3.4.3 Stability-Analysis . . . 46
3.5 Patient Data . . . 46

4 Results **48**
4.1 XCAT Phantom . . . 48
4.1.1 Reconstructed Images . . . 48
4.1.2 Bias Analysis . . . 51
4.1.3 Stability Analysis . . . 52
4.2 Numerical Phantom . . . 54
4.2.1 Reconstructed Images . . . 54
4.2.2 Bias Analysis . . . 57
4.2.3 Stability Analysis . . . 59
4.2.4 Separability Analysis . . . 60
4.3 Patient Data . . . 61
4.3.1 Reconstructed Images . . . 61
4.3.2 Myocardium to Background Ratio and Noise Properties . . . 64

5 Summary and Discussion **67**
5.1 Summary of Results . . . 67
5.2 Discussion of XCAT-Phantom Results . . . 69
5.3 Discussion of Numerical-Phantom Results . . . 69
5.4 Discussion of Patient Data Results . . . 70
5.5 Comparison of XCAT-Phantom and Numerical-Phantom . . . 71
5.6 Comparison of Phantom-Data studies and Patient Data studies . . . 72

6 Conclusion and Outlook **73**

Bibliography **74**

List of figures

Fig. 2.1 Feynman Diagram of the β^+ decay 10
Fig. 2.2 Feynman Diagram of electron (e^-) positron (e^+) Annihilation . . 10
Fig. 2.3 β^+ spectra of radioisotopes used in PET with normalized maxima 11
Fig. 2.4 Schematic of the Photoelectric Effect 14
Fig. 2.5 Schematic of the Compton Effect 14
Fig. 2.6 Gamma-Ray-Interaction 15
Fig. 2.7 Schematic of a Scintillation Detector in combination with a Photo Multiplier Tube 16
Fig. 2.8 Schematic of a Avalanche Photodiode (APD) 17
Fig. 2.9 Schematic of a Silicon Photomultiplier(SiPM) 18
Fig. 2.10 Different types of possible events that can be recorded by a PET ring-system (Bailey et al., 2005) 19
Fig. 2.11 Visualisation of a line of response (LOR) and a projection $p(s, \phi)$ 21
Fig. 2.12 Comparison of conventional PET and Time of Flight (TOF) PET 23
Fig. 2.13 Scheme of Filtered Back Projection (FBP) Algorithm 25
Fig. 2.14 Maximum-Likelihood Expectation Maximization (MLEM) Algorithm 26
Fig. 2.15 Effect of respiratory and cardiac motion on PET image quality - (A) Blurring effect due to cardiac motion and (B) Motion-induced artifact due to miss-registratio 30
Fig. 2.16 Simplified process of List-Mode Motion Compensation 32
Fig. 2.17 Simplified flowchart of Motion Compensated Image Reconstruction (MCIR) 33
Fig. 2.18 Simplified flowchart of Reconstruct-Transform-Average (RTA) . . 34

Fig. 3.1 Siemens Biograph mMR 36
Fig. 3.2 Motion Compensation Approaches listed according to the timing of incorporation of the motion information into the image reconstruction process 37
Fig. 3.3 Simplified flowchart of Projection-Based Motion Compensation (P-MoCo) 38
Fig. 3.4 Simulated motion of the XCAT phantom 41
Fig. 3.5 The 4D extended cardiac-torso (XCAT) phantom 42
Fig. 3.6 Numerical Phantom 42
Fig. 3.7 Flow-chart of the dual-tracer PET/MRI protocol 47

Fig. 4.1 XCAT Phantom - Comparison of OSEM, RTA, MCIR, P-MoCo, Gated and No-Motion for 1D and 2D movement with corresponding Line Profiles 49
Fig. 4.2 XCAT Phantom - Myocardium to Liver and Myocardium to Lumen Ratio for 1D and 2D movement of OSEM, RTA, MCIR, P-MoCo, Gated and No-Motion 50
Fig. 4.3 XCAT Phantom - Bias analysis for 1D and 2D movement of OSEM, RTA, MCIR, P-MoCo, Gated and No-Motion 51
Fig. 4.4 XCAT Phantom - Stability of Myocardium to Liver (M2Li) Ratio 1D, 2D and 3D movement of RTA, MCIR and P-MoCo for 1D and 2D movement 52
Fig. 4.5 Numerical Phantom - Comparison of OSEM, RTA, MCIR, P-MoCo, Gated and No-Motion for 1D movement with corresponding Line Profile 54
Fig. 4.6 Numerical Phantom - Comparison of OSEM, RTA, MCIR, P-MoCo, Gated and No-Motion for 2D movement with corresponding Line Profile 55
Fig. 4.7 Numerical Phantom - Comparison of OSEM, RTA, MCIR, P-MoCo, Gated and No-Motion for 3D movement with corresponding Line Profile 56
Fig. 4.8 Numerical Phantom - Maximum Lesion to Background (LBR_{max}) for 1D, 2D and 3D movement of OSEM, RTA, MCIR, P-MoCo, Gated and No-Motion 57
Fig. 4.9 Numerical Phantom - Lesion to Background (LBR) and Bias analysis for 1D, 2D and 3D movement of OSEM, RTA, MCIR, P-MoCo, Gated and No-Motion 58
Fig. 4.10 Numerical Phantom - Comparison of stability of Lesion to Background (LBR) of RTA, MCIR and P-MoCo for Lesion and Myocardium with 1D, 2D and 3D movement 59
Fig. 4.11 Numerical Phantom - Separability study for 1D, 2D and 3D movement of OSEM, RTA, MCIR, P-MoCo, Gated and No-Motion 60
Fig. 4.12 Patient A - Comparison of OSEM, RTA, P-MoCo and Gated Reconstruction for the two tracers FDG and NH_3 62
Fig. 4.13 Patient B - FDG and NH3 - Line Profile 63
Fig. 4.14 Myocardium to Background (M2B) for Patient A and B of OSEM, RTA, P-MoCo and Gated Reconstruction for FDG and NH_3 tracers 65

List of tables

Table 2.1 Isotope production reactions, maximum range (R_{max}) and mean range (R_{mean}) of positrons is in water of commonly used PET radiotracers 12
Table 2.2 Selection of positron-emitting radionuclides used in PET 12

Table 3.1 Specifications of the Siemens Biograph mMR 37
Table 3.2 Overview of simulated motion parameters for XCAT Phantom and Numerical Phantom 43

Table 4.1 Patient Datasets A and B - Myocardium to Background Ratio measured at the maximum iteration number of 105 iterations and the respective percentage of noise measured in the image 64
Table 4.2 Patient Datasets A and B - Mean Myocardium to Background Ratio measured at the maximum iteration number of 105 iterations ($M2B_{mean}$) with corresponding standard deviation and the respective mean percentage of noise ($Noise_{mean}$) with corresponding standard deviation. 66

List of abbreviations

APD Avalanche Photodiode

CNR Contrast to Noise Ratio

CT Computed Tomography

CTW Coincidence Time Window

FBP Filtered Back Projection

FDG Fluorine-18 labeled 2-flouro-2-deoxy-D-glucose

FOV Field of View

FWHM Full Width at Half Maximum

HU Hounsfield units

IQ Image Quality

IR Image Reconstruction

L2B Lesion to Background Ratio

LM List Mode

LM-EM List-Mode Expectation Maximization

LOR Line of Response

M2B Myocardium to Background Ratio

MCIR Motion-Compensated Image Reconstruction

MIRT Medical Image Registration Toolbox

ML-EM Maximum-Likelihood Expectation Maximization

MoCo Motion Compensation

MRI Magnetic Resonance Imaging

OSEM Ordered Subsets Expectation Maximization

OSMAPOSL Ordered Subsets Maximum a posteriori One-step-late

PET Positron Emission Tomography

P-MoCo Projection Based Motion Compensation

PMT Photo Multiplier Tube

ROI Region of Interest

RTA Reconstruct-Transform-Average

SiPM Silicon Photomultiplier

SNR Signal-to-Noise Ratio

STIR Software for Tomographic Image Reconstruction

SUV Standardized Uptake Value

TOF Time of Flight

XCAT Extended Cardiac-torso

1. Introduction

I was born not knowing and have had only a little time to change that here and there.

Richard Feynman

The very first PET scanner was developed by Phelps and colleagues in the late 70s (Phelps et al., 1975; Ter-Pogossian et al., 1975). Since then, PET developed to be an important tool for nuclear medicine applications in the area of functional imaging. While other anatomic imaging techniques like Computed Tomography (CT) or Magnetic Resonance Imaging (MRI) use X-rays or strong magnetic fields for imaging, PET allows for the three-dimensional mapping of positron-emitting radio pharmaceuticals that are injected into the patient body before examination.

The coverage of applications across various clinical sectors is enormous in PET, spreading from neurology to psychiatry, cardiology and oncology. From the neurology point of view, PET is used for the detection of brain tumors (Tai and Piccini, 2004) as well as early recognition of risks of epilepsy or dementias. In cardiology, PET is employed for diagnosis of myocardial perfusion and viability (Bengel et al., 2009), among other applications. In oncology, important progress in possibilities of diagnosis, detection and monitoring of therapy response (Bailey et al., 2005) can be attributed to PET.

When imaging the thoracic area, involuntary patient movements like breathing (Nehmeh and Erdi, 2008; Kesner et al., 2014) or complex contractions of the heart (Sengupta et al., 2006) degrades the quantitative accuracy of the PET images (Munoz et al., 2016; Kolbitsch et al., 2017). Movement of the patient primarily results in the overlapping of normal and abnormal areas of the obtained PET image. This unwanted effect causes a reduction of the image contrast, blurring and a loss of sharp edges, leading to biased quantitative measures and reduction of the spatial resolution of PET images (Catana, 2015; Gillman et al., 2017). Therefore patient motion leads to a reduction of reliability in clinical image interpretation.

Objective: To counteract the motion-implied PET performance losses, different MoCo methods were developed and proposed in the literature (Rahmim et al., 2013; Feng et al., 2016). These techniques can be classified as: 1 - List-Mode Motion Compensation (LM- MoCo), which incorporates the motion-information before the image reconstruction (Livieratos et al., 2005). 2 - MCIR, in which the motion compensation is performed during the image reconstruction-process (Polycarpou et al., 2012) and 3 - the RTA method that incorporates it after image reconstruction (Picard, 1997). The aim of this thesis is to evaluate, using simulated data, the performance and accuracy of these MoCo techniques in PET acquisitions with respiratory and cardiac motion. Furthermore, we also included some preliminary evaluations of the performance of the MoCo approaches in real patient data.

Structure: Physical and technical basics of PET imaging, including an overview of hybrid technology, analytic- and iterative image reconstruction methods and fundamental principles of motion compensation are described in chapter 2. Chapter 3 introduces the Biograph mMR system, gives a brief overview over the used motion compensation approaches, including projection-based MoCo (P-Moco), motion compensated Image reconstruction (MCIR) as well as the Reconstruct Transform Average (RTA) method. Further, phantom data and image quality analysis are described and a short introduction to patient data concludes the chapter. On this basis, chapter 4, gives deep and comparative insights in the obtained results from numerical phantom data, XCAT phantom data as well as a brief look at patient data. Finally, Chapter 5 gives a summary and discussion of the results and chapter 6 presents the main conclusions of this master thesis.

2. Theoretical Background and PET Principles

This chapter provides a general introduction to PET. Section 2.1 introduces fundamental physical principles of PET, section 2.2 provides an overview of hybrid technology including PET/CT and PET/MR, section 2.3 highlights different analytic- and iterative image reconstruction methods, section 2.4 focuses on data correction and quantification and section 2.5 introduces fundamental principles of motion compensation.

2.1 PET Physics

This section presents the the most fundamental physical principles of PET. Starting from the process of positron emission, the subsequent interaction with matter and the detectors are discussed. Furthermore, a discussion on image formation, including a classification of coincidence events, is given.

2.1.1 Positron Emission and Annihilation

Positrons (e^+) are antiparticles of electrons (e^-) with identical mass[i] and spin quantum number[ii], but opposite electric charge[iii]. They where theorised 1928 (Dirac, P. A. M., 1928) and discovered 1932 (Anderson, C. D., 1933). Positrons are produced naturally in β^+ decays of radioactive isotopes or in interactions of gamma quanta with matter (see section 2.1.3).

[i] $m_e = 9.109 \times 10^{-31}\,\mathrm{kg}$
[ii] $s_{e^\pm} = 1/2$
[iii] $q_{e^+} = 1\,e$

Theorised (1928): With the attempt of explaining the Zeeman effect, Paul Dirac proposed the Dirac Equation[iv]

$$\left(c\,\alpha_i p_i + mc^2\beta\right)\Psi\left(r_i,t\right) = i\hbar\frac{\partial}{\partial t}\Psi\left(r_i,t\right) \tag{2.1}$$

with the matrix-inputs[v]

$$\alpha_{i=1,2,3} = \begin{pmatrix} 0 & \sigma_i \\ \sigma_i & 0 \end{pmatrix} \quad \beta = \begin{pmatrix} \mathbb{1}_2 & 0 \\ 0 & -\mathbb{1}_2 \end{pmatrix}$$

in 1928. The Dirac equation unifies quantum mechanics, special relativity and the - *at that time new* - concept of electron spin by replacing the 3D wave function $\Psi\left(r_{i=xyz}\right)$ with a four-component wave function $\Psi\left(r_{i=xyz},t\right)$ of form

$$\Psi\left(r_i,t\right) = \begin{pmatrix} \Psi_1\left(r_i,t\right) \\ \Psi_2\left(r_i,t\right) \\ \Psi_3\left(r_i,t\right) \\ \Psi_4\left(r_i,t\right) \end{pmatrix} = \begin{pmatrix} \Psi_A\left(r_i,t\right) \\ \Psi_B\left(r_i,t\right) \end{pmatrix} \quad with \begin{cases} \Psi_A\left(r_i,t\right) = \begin{pmatrix} \Psi_1\left(r_i,t\right) \\ \Psi_2\left(r_i,t\right) \end{pmatrix} \\ \Psi_B\left(r_i,t\right) = \begin{pmatrix} \Psi_3\left(r_i,t\right) \\ \Psi_4\left(r_i,t\right) \end{pmatrix} \end{cases} \tag{2.2}$$

called spinor. Solving 2.1 with 2.2 leads to a coupled system of differential equations, that can be solved for a resting particle[vi] to the plane waves

$$i\hbar\partial_t\Psi_A\left(r_i,t\right) = +mc^2\Psi_A\left(r_i,t\right) \quad \Rightarrow \quad \Psi_A\left(r_i,t\right) = \Psi_{A0}\cdot e^{-\frac{i}{\hbar}mc^2t} \tag{2.3}$$

$$i\hbar\partial_t\Psi_B\left(r_i,t\right) = -mc^2\Psi_B\left(r_i,t\right) \quad \Rightarrow \quad \Psi_B\left(r_i,t\right) = \Psi_{B0}\cdot e^{\frac{i}{\hbar}mc^2t} \tag{2.4}$$

with positive-energy solutions, corresponding to electrons, and negative-energy solutions, corresponding to antiparticles of the electron, the so called positrons.

Discovery (1932): By passing cosmic rays through a cloud chamber and a lead plate, Carl David Anderson discovered the positron 1932, when analysing the particles curvature in a magnetic field that matches the mass-to-charge ratio of an electron, but in a direction that implies a positive charge. Anderson won the Nobel prize in Physics for this discovery in 1936.

The β^+ decay: Beta decay (β-decay) is a type of radioactive decay in which, besides other by-products, an electron (in the β^- decay) or positron (in the β^+ decay) as well as a neutrino are emitted (Fermi E., 1934). This process is a direct consequence of the weak force which can enable a change of quark flavour by the exchange of a intermediate vector-boson (W^+, W^- or Z^0).

[iv] with the dirac-matrices $\gamma_0 = \gamma^0 = \beta$ and $\gamma_i = \alpha_i\beta = -\gamma^i$, 2.1 can be rewritten to the better-known covariant form $\left(i\gamma^\mu\partial_\mu - \kappa\right)\Psi = 0$

[v] Here, $\sigma_{i=1,2,3}$ denote the pauli-matrices

[vi] The resting particle is defined by $p_i = 0$ with initial condition $\Psi_A\left(r_i,t=0\right) = \Psi_{A0}$ and $\Psi_B\left(r_i,t=0\right) = \Psi_{B0}$

Baryons are combinations of quarks, which exist in the six types up, down, top, bottom, strange and charm which are called flavours. Protons (p^+) are build of two up- and one down quark (uud), neutrons (n^0) of two down- and only one up quark (udd).

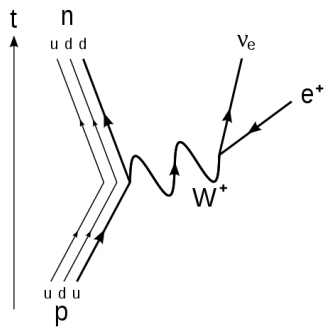

Figure 2.1: Feynman Diagram of the β^+ decay - A proton (p^+) is converted to a neutron (n^0), a positron (e^+) and a electron neutrino (ν_e) via the intermediate W^+-boson

As can be seen in the Feynman diagram of the β^+ decay (2.1), a p^+ is converted to a n^0, a positron (e^+) and a electron neutrino (ν_e).

$$p^+ \rightarrow n^0 + e^+ + \nu_e + \delta Q \tag{2.5}$$

This process takes place via the intermediate W^+-boson and the related flavour-change $u \rightarrow d$ of the p^+. The released energy δQ is shared by the e^+ and ν_e in the form of kinetic energy.

In general, the β^+ decay decreases the atomic number Z of the parent nucleus X by one (Konya and Nagy, 2012)

$${}^{\mathrm{A}}_{\mathrm{Z}}\mathrm{X} \longrightarrow {}^{\mathrm{A}}_{\mathrm{Z-1}}\mathrm{X} + e^+ + \nu_e + \delta Q \tag{2.6}$$

To enable β^+ decay, the mass-difference of parent and daughter atom has to exceed twice the electron mass, since the masses of the released e^+ and e^- reduce the released energy δQ by 1022 keV. As the available energy is shared by the e^+ and ν_e, e^+ are emitted in a continuous spectrum. Figure 2.3 shows the typical emission spectra for several radionuclides commonly used in PET (see section 2.1.2).

Annihilation: After the p^+ travels a finite distance (the so called positron range - see table 2.1) and looses kinetic energy by means of inelastic scattering, annihilation occurs. As indicated in the corresponding Feynman diagram (figure 2.2), annihilation results in the emission of two photons (γ), each with energy equal to the rest energy of the e^+ and e^- (511 keV). The two γ are basically emitted in opposite directions, however, there exists an angular uncertainty of γ-emission of about 0.5°, due to non-zero momentum of positronium.

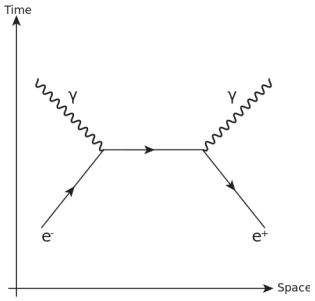

Figure 2.2: Feynman Diagram of Annihilation - an electron (e^-) and a positron (e^+) annihilate to two photons (γ)

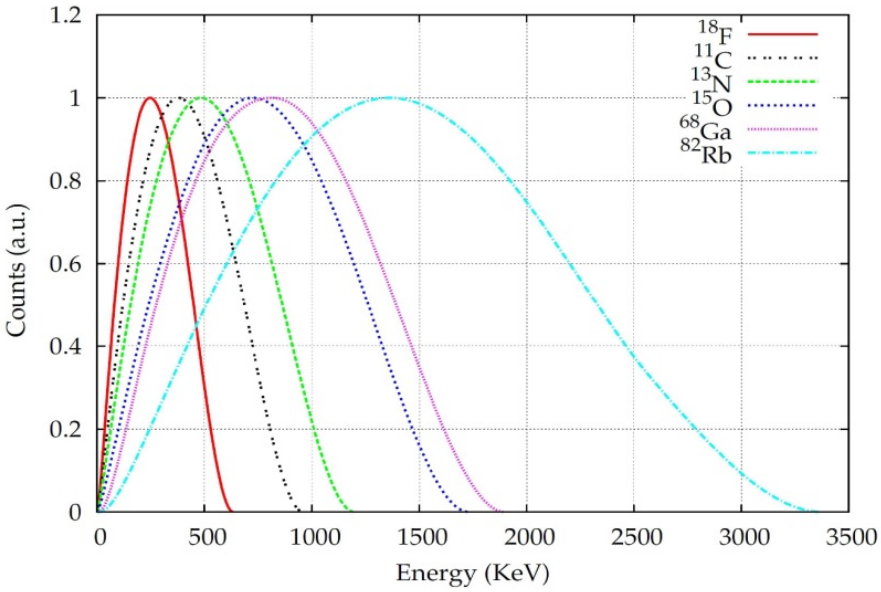

Figure 2.3: β^+ spectra of radioisotopes used in PET with normalized maxima (Cal-González, 2014)

Finite positron ranges limit PET by means of the the fundamental spatial resolution of the system, angular uncertainty of γ-emission can cause a Gaussian blurring.

2.1.2 PET Radionuclides

PET imaging is dependent on positron-emitting biomolecules that are injected into the patient body before examination. In nuclear medicine, three principal methods of production of such radioisotopes exist. They can either be produced by (i) separation of the by-product produced during fission, (ii) from neutron irradiation in a reactor or (iii) from bombardment of a target material by charged particles from accelerators (Jadvar and Parker, 2005).

The most widely used Positron-emitting Radionuclides in PET (see table 2.2) are produced in cyclotron accelerators or specific generators. Most low-molecular-weight PET radioisotopes like Carbon-11, Nitrogen-13, Oxygen-15 and Fluorine-18 are produced by charged particle bombardment in cyclotrons (Alauddin, 2012). Other radionuclides like Gallium-68 or Rubidium-82 are obtained as decay products from parent isotopes. Selected isotope production reactions are shown in table 2.1.

A frequently used radio tracer in PET is **Fluorine-18 labeled 2-flouro-2-deoxy-D-glucose (FDG)** that uses the high Glucose Metabolic Rate of most cancers for imaging (Hoh, 2007). FDG is used in oncology in terms of Standardized Uptake Value (SUV) of ^{18}F-FDG in tumor cells (Lucignani et al., 2004). Moreover, FDG

Table 2.1: Isotope production reactions, maximum range (R_{max}) and mean range (R_{mean}) of positrons is in water of commonly used PET radiotracers (Sonzogni, 2016; NIST, 2018)

Isotope	**Production Reaction**	R_{max} [mm]	R_{mean} [mm]
^{11}C	^{14}N (p,α) ^{11}C	4.2	1.2
^{13}N	^{16}O (p,α) ^{13}N	5.5	1.8
^{15}O	^{14}N (d,n) ^{15}O	8.4	3.0
^{18}F	^{18}O (p,n) ^{18}F	2.4	0.6
^{38}K	^{38}Ar (p,n) ^{38}K	3.6	2.6
^{62}Cu	^{62}Ni (p,n) ^{62}Cu	6.1	4.4
^{64}Cu	^{64}Ni (p,n) ^{64}Cu	2.5	0.7
^{68}Ga	^{68}Zn (p,n) ^{68}Ga	2.7	1.2
^{82}Rb	^{82}Sr (p,n) ^{82}Rb	14.1	5.9
^{89}Zr	^{89}Y (p,n) ^{89}Zr	3.8	1.3
^{124}I	^{124}Te (p,n) ^{124}I	8.7	3.5

Table 2.2: Selection of positron-emitting radionuclides used in PET (Sonzogni, 2016; Jadvar and Parker, 2005) - All values denoted with * correspond to mean values

Radio-nuclide	**Half-life** [min]	β^+ **Branching fraction*** [%]	β^+ **Energy*** [keV]	**Production**	β^+ **Dose*** [MeV/Bq-s]
^{11}C	20.36	99.80	385.7	Cyclotron	0.385
^{13}N	9.97	99.80	491.8	Cyclotron	0.491
^{15}O	2.03	99.90	735.3	Cyclotron	0.735
^{18}F	109.7	96.70	249.8	Cyclotron	0.242
^{38}K	7.64	99.92	2323.0	Cyclotron	2.321
^{62}Cu	9.67	97.83	1319.0	Generator	1.290
^{64}Cu	762.0	17.60	278.0	Cyclotron	0.049
^{68}Ga	67.71	88.90	829.5	Generator	0.738
^{82}Rb	1.258	95.40	1479.0	Generator	1.411
^{124}I	6013.0	22.70	820.0	Cyclotron	0.186
^{89}Zr	4705.0	1.53	470.0	Cyclotron	0.007

can be used for the assessment of glucose metabolism in the heart, lungs, and the brain. Because of the complexity of radiopharmaceutical development on-site, the clinical impact of PET was limited until the mid 1990s. FDG's comparatively long half life of 109.7 min and the large number of clinical indications helped PET to reach a critical volume, so that full-time operation of a PET scanner becomes reasonable as a pure clinical facility (Jadvar and Parker, 2005).

Besides others, **Nitrogen-13-labeled Ammonia** is used for myocardial perfusion imaging because of good diffusion across cell membranes through glutamine syntheses to ^{13}N-glutamine (Maddahi and Packard, 2014; Kuhle et al., 1992). The assessment of myocardial perfusion with **Oxygen-15-labeled water** (^{15}O-water) is an established technique in cardiac PET, using ^{15}O-water's high extraction fraction that is independent of flow rate (Bergmann et al., 2000). The usage of ^{13}N ammonia or ^{15}O-water is limited by need for an on-site or nearby cyclotron due to half-lives ranging from 2-10 minutes.

Another commonly used PET radiotracer is **Rubidium-82**. Due to its rapid uptake in cardiac muscle cell (Alvarez-Diez et al., 1999). ^{82}Rb is not dependent on on-site cyclotrons since it is obtained as decay product from Strontium-82. The difficult handling of ^{82}Rb's short half-life of about 75 seconds can be overcome by commercial services that allow the sharing of the strontium generator between more than one facility. This is possible due to ^{82}Sr's comparably long half-life of about 25-days.

2.1.3 Gamma Ray Interaction with Matter

Gamma ray interaction with matter is described by three main processes, whose interaction probabilities depend on their energy, and results in a characteristic background spectrum for any gamma detector. The probabilities of the three mainly contributing processes, Photoelectric effect (μ_{photo}), Compton scattering ($\mu_{compton}$) and Pair production (μ_{pair}), add up to the linear attenuation coefficient

$$\mu_{total} = \mu_{photo} + \mu_{compton} + \mu_{pair} \tag{2.7}$$

All three processes relevant for PET are described in the following:

Photoelectric Effect - The photoelectric effect is relevant for energies up to 100 keV (see figure 2.6). The total energy of an incident photon with energy $h\nu$ is absorbed by an atom and causing latter to emit an electron with a kinetic energy (2.8), as illustrated in figure 2.5. The kinetic energy consists of the photon's energy deducting the binding energy needed to ionize the same electron (Williams, 1991).

$$E_{kin} = h \cdot \nu - E_{bind} \tag{2.8}$$

The emitted electron, which is identical to a beta particle, travels through matter and primarily interacts by means of (i) ionisation of other atoms or (ii) creation of bremsstrahlung with energies less than the kinetic energy of the electron. When the atom, initially ionized by the photon, has an electron hole in the K shell, an electron from an outer shell falls from its higher state in the gap and causes the atom to emit characteristic X-radiation or an Auger electron, both with short ranges caused by their low energies.

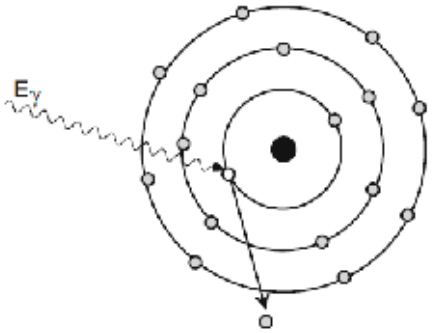

Figure 2.4: Schematic of the Photoelectric Effect

$$E_{kin} = E_{X-ray} = E_{bind}^{outher} - E_{bind}^{inner} \tag{2.9}$$

Compton Effect: The Compton effect occurs if the incident photon interacts with an electron in the outer shell of an atom by means of scattering and deposes parts of its energy. In contrast to the photoelectric effect, the scattered photon is not totally absorbed by the interaction and continues to travel through the matter. The Compton effect becomes dominant at photon energies ranging from approximately 100 Kev to 3 Mev (see figure 2.6). Its energy loss (2.10) depends on the scatter angle θ, respectively the energy of the accelerated electron.

$$E_{e^-} = E_\gamma - E'_\gamma \tag{2.10}$$

The minimal energy transfer occurs at $\theta = 0°$ which would be equivalent to no photon scattering. The maximum possible energy transfer to the electron, for a single Compton effect, occurs at $\theta = 180°$ and causes backscattering of the photon in the direction of its origin. In order to calculate the results of the scattering process, the electron is considered as a free particle. Therefore the angle θ of the scattered photon needs to be known as well as either[vii] the wavelength λ (Krane, 1988),

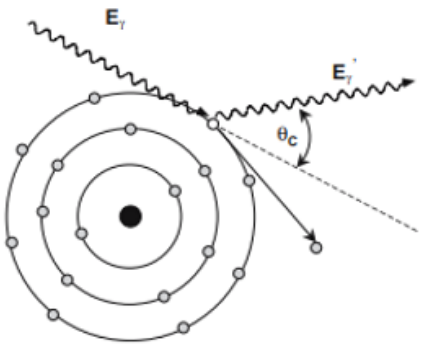

Figure 2.5: Schematic of the Compton Effect

$$\lambda' = \lambda + \frac{h}{m_0 c}(1 - cos\theta) \tag{2.11}$$

the frequency ν

$$\nu' = \frac{\nu}{1 + (\frac{h\nu}{m_0 c^2})(1 - cos\theta)} \tag{2.12}$$

[vii] $E_\gamma = \hbar\omega = h\nu = h\frac{c}{\lambda}$

or the energy E_γ

$$E'_\gamma = \frac{E_\gamma}{1 + (\frac{E_\gamma}{m_0 c^2})(1 - cos\theta)} \tag{2.13}$$

of the incident photon.

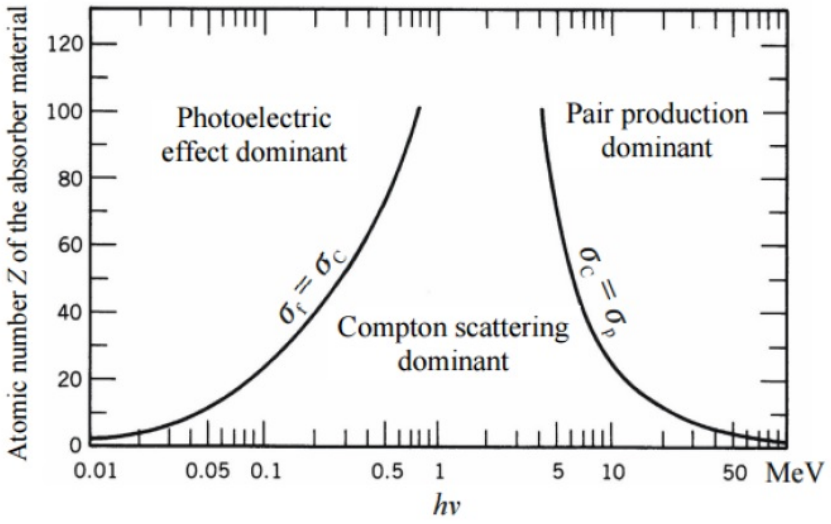

Figure 2.6: Gamma-Ray-Interaction

Pair Production: This process can only occur at photon energies above 1022 keV. The lower limit of 1022 keV consists of the rest mass of 2 electrons respectively the rest mass of an electron and a positron which are produced by conversion of the photon. Close above 1022 keV the probability of pair production is very low since the photon is more likely to lose its energy by means of Compton scattering in the outer shell than penetrating to the atoms core. However, with increasing energy (several MeV), pair production dominates the gamma ray spectrum (see figure 2.6) (Hubbel, 1969). The remaining photon energy goes into kinetic energy inputs equally shared by the positron and the electron. The produced electron triggers the same effects as described in chapter 2.1.3, the positron will annihilate with an electron and create 2 photons with 511 keV each send out in opposite directions.

2.1.4 PET detectors

Scintillation Detectors

Scintillation detectors, as the name suggests, depend on the scintillation process. Strictly speaking, the scintillation process can be broken down into three sub-processes. The ionizing radiation, absorbed by the scintillator crystal, creates (i)

electron–hole pairs in the crystal material which are related to an energy E. This energy can be (ii) transferred to a luminescent center and (iii) light emission takes place. Note that the above description is fairly general and differs between the selected scintillator materials. The detection of ionizing radiation of energy E and

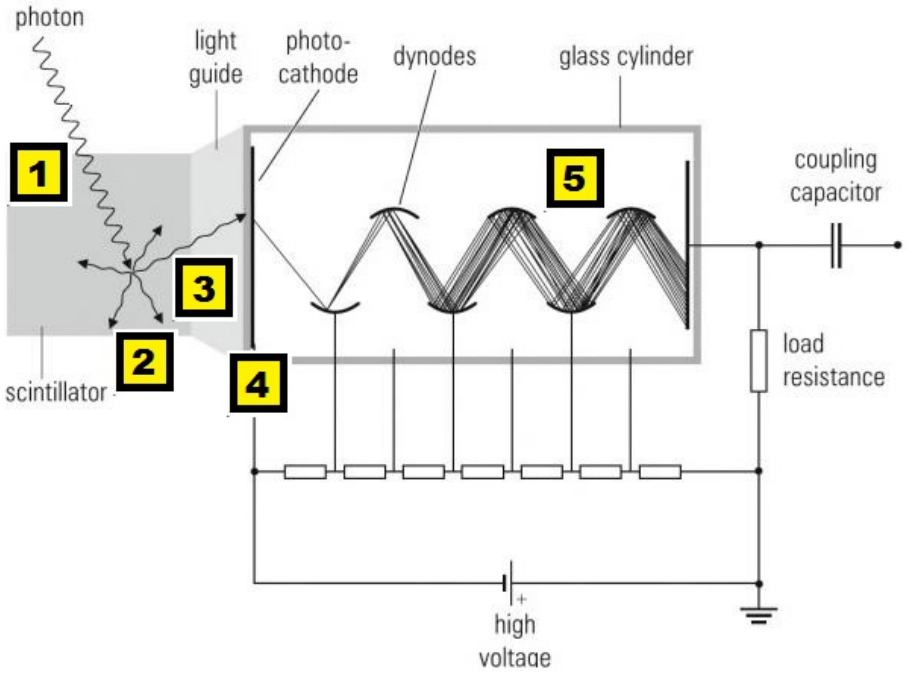

Figure 2.7: Schematic of a Scintillation Detector in combination with a Photo Multiplier Tube (PMT) (adapted and rearranged from Grupen (2010))

consequently the operation of the underlying scintillation detector principle can be broken down into five fundamental steps (Birks, 1964) which are shown in in figure 2.7 and described in the following:

Enclosed by a dense and opaque material ionizing radiation of energy E is absorbed (1) by a scintillator material, surrounded by a reflector, causing ionisation and excitation, hence starting the scintillation process (2). A certain proportion E' of the initial energy E is converted in N photons. Maximised by the reflector geometry, $N' = g \cdot N$ photons pass the scintillator material as well as the light guide and impinge on the photo cathode (3). Once more a certain proportion T of initial N' photons generate T photo electrons in interaction with the photo cathode (4). Accelerated by the potential difference between the cathode and the first dynode these T photo electrons impinge and generate P further electrons by secondary emission, hence $M = T \cdot R$ electrons[viii] interact with the next dynode causing an immense electron avalanche (5) resulting in an total electron number $M_{tot} = R^n \cdot T$ after n dynodes.

[viii] with an assumed dynode multiplication factor R

Photo Multiplier Tube (PMT) - A Dynode Photomultipier, also called Photo Multiplier Tube (PMT), converts a scintillation of visible light into a current pulse of secondary electrons. It amplifies this current, which makes an analysis of this current pulse as a function of radiation energy, absorbed by the scintillation detector, possible. Typically, gains in the order of $10^5 - 10^8$ can be reached with PMTs. Nevertheless, PMTs are unsuitable for use in combination with Magnetic Resonance scanners. This is due to deflection of the electrons between the photocathode and the dynodes in presence of magnetic fields.

Avalanche Photodiode (APD) - The Avalanche Photodiode (APD) uses the internal photoelectric effect for generation of charge carriers and the avalanche effect for amplification (see figure 2.8). APDs can be seen as the semiconductor-equivalent

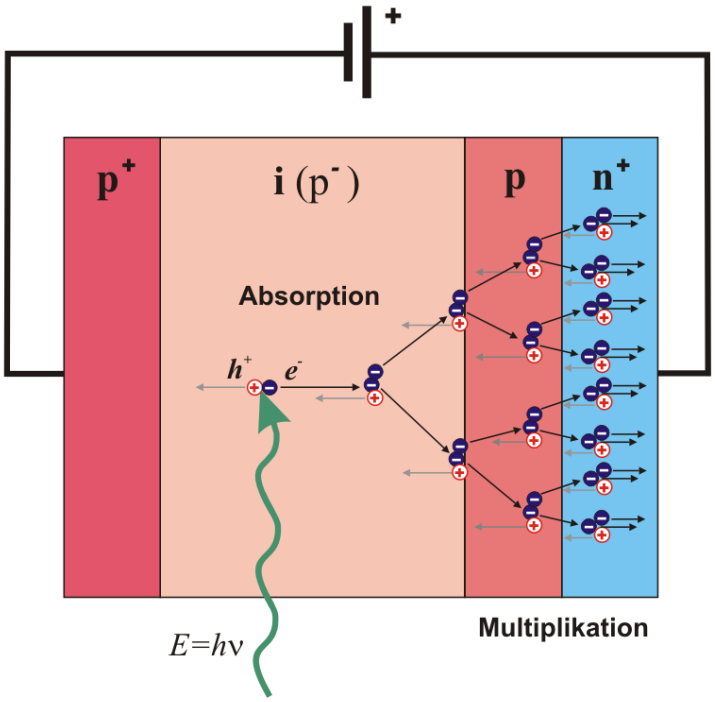

Figure 2.8: Schematic of a Avalanche Photodiode (APD) - Photons are absorbed in the fully depleted intrinsic i-layer, where they create pairs of charge carriers. Electrons are then accelerated towards the multiplication zone and cause an avalanche effect (Image under Creative-Commons license from Wikimedia-Commons (2018))

to PMTs. They consist of a low-field depleted region where photons can create electron-hole pairs. By applying a high reverse bias voltage, charge carriers can achieve energies $E' > E_g$ which are larger than the band gap energy E_g, and therefore can create new electron-hole pairs by means of impact ionization. Due to this avalanche effect, APDs can multiply electron-hole pairs which increases the initial photo current. In comparison with traditional PMT tubes, APDs present

a much lower amplification, making necessary the use of low-noise, fast front-end readout electronics (Webb et al., 1974; Pichler et al., 2006).

Silicon Photomultiplier(SiPM) - A Silicon Photomultiplier (SiPM) consists of an array of APD cells that are connected in parallel and operated in the so-called Geiger mode (above breakdown voltage) (see figure 2.9). SiPM combine the advantages of PMTs and solid-state sensors, they do not require high operating voltages, are insensitive to shocks and magnetic fields and are cooperatively smaller (Piatek, 2018). Therefore SiPMs have many attractive properties for implementing in PET. However, a non-linear response, low photon detection efficiency or high dark current are drawbacks that need to be considered (Otte et al., 2006). These drawbacks are mainly considered by high trigger threshold-levels of fully digital trigger networks (Degenhardt et al., 2009; Frach et al., 2009) or by active sensor cooling (Cabello, 2016).

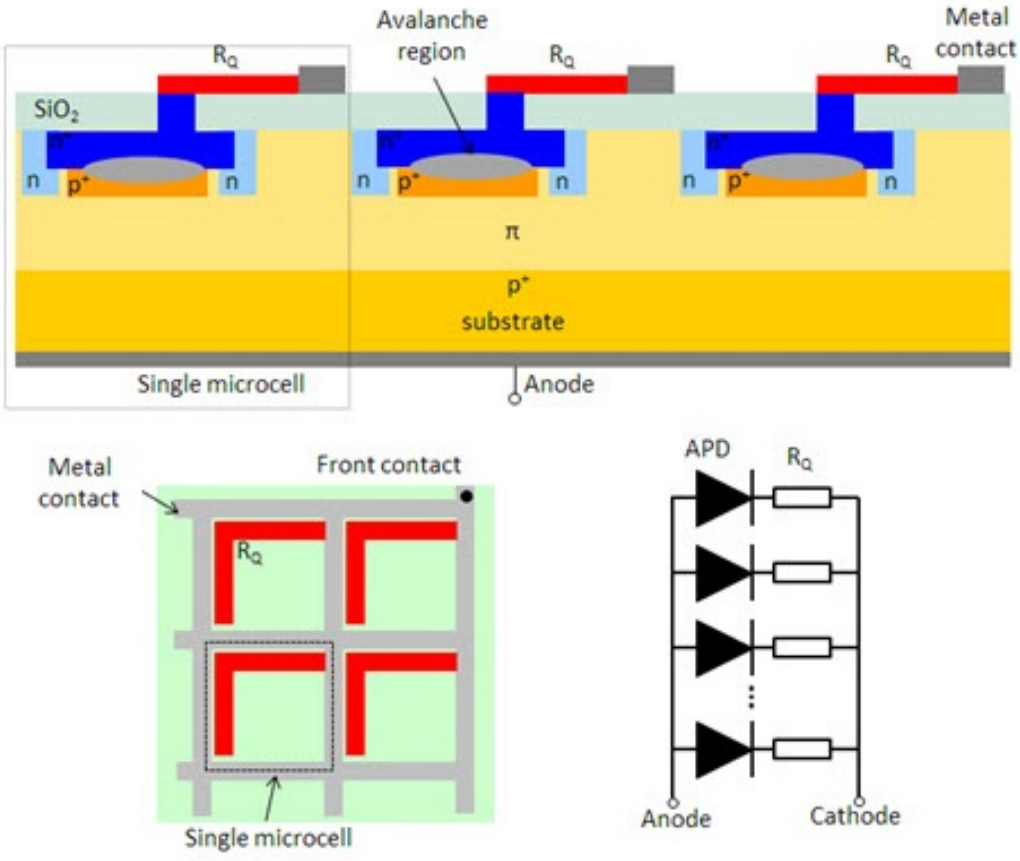

Figure 2.9: Schematic of a Silicon Photomultiplier(SiPM) - Each microcell is a series combination of an Avalanche Photodiode (APD) and a Resistor (R_Q). All of the microcells are connected in parallel - The three panels show a cross section of three microcells (top), a top view of the device (bottom left) and an equivalent electrical circuit (bottom right). (Piatek, 2018)

2.1.5 Image Formation

As already discussed in the former sections, annihilation leads to emission of two nearly collinear photons of 511 keV. In order to receive a valid event, which is referred to as *prompt event*, the detected pair of photons must meet all the following criteria:

Both photons have to be (i) registered within a *coincidence-time window*, (ii) the energy deposited of each photon has to be within a pre-defined *energy-window* and (iii) the corresponding Line of Response (LOR) has to be within a valid *acceptance-angle*. Due to a wide variety of possibilities for prompt-event generation of two photons, there are numerous possible types of detectable-events in PET acquisition.

Classification of Coincidence Events

The registration of a photon in a PET system is called a **Single event**. With a probability of 1-10% a Single event is counted as paired coincidence.

An event that derives from a single positron–electron annihilation, where the two

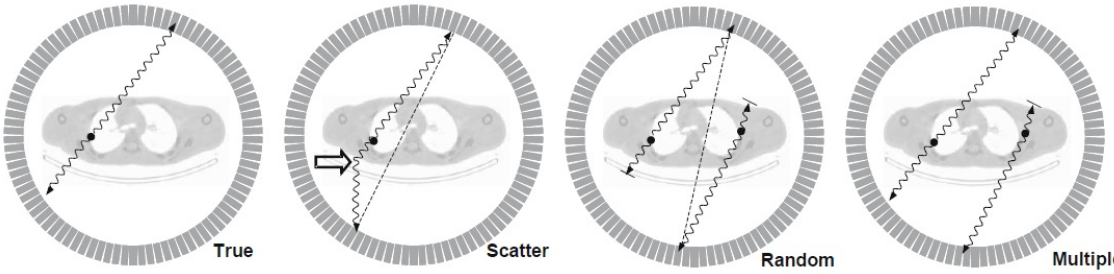

Figure 2.10: Different types of possible events that can be recorded by a PET ring-system (Bailey et al., 2005)

annihilation photons reach the detectors on opposing sides, within the coincidence-time and without interacting significantly with the surrounding atoms, is called a **True event**.

Compton scattering of one or both annihilation photons causes a loss in energy and therefore a change in direction of photon propagation. As can be seen in 2.10, the consequence of counting scattered events is a misaligned LOR that is uncorrelated with the origin of the annihilation event. Up to 30-40% of all prompts are **Scattered events** in clinical PET imaging (Vandenberghe et al., 2016b). In preclinical PET of small animals, these fraction is smaller ($\approx$ 10-15%) (Goertzen et al., 2012).

Accidentally, the decay of two completely unrelated nuclei can happen at the same time. Two of the four annihilation photons can then be counted within the coincidence-time and therefore mistakenly be considered to come from the same positron, while the other two are lost. Given the individual single event rates $r_{[\alpha,\beta]}$ for detectors α and β as well as the Coincidence Time Window (CTW) τ, the number of **Random events** is given by[ix] (Bailey et al., 2005)

$$R_{\alpha\beta} = 2\tau \cdot r_\alpha r_\beta \propto {r_\alpha}^2 \tag{2.14}$$

Random events are removed by estimation of $R_{\alpha\beta}$ by use of 2.14 or by introducing a delayed CTW. This approach is the preferred and most commonly used approach which is actually used in the Siemens systems.

When the system detects more than two events within a given CTW, a **Multiple event** takes place. Since it is not possible to determine the LOR to which the event is assigned, multiple events are usually discarded by the electronics or add additional background to the image due to incorrect computation.

Data Management in PET

In PET, two common methods of data acquisition exist. Two-dimensional (2D) acquisition mode collects data within a specific transaxial plane. This technique allows for separate reconstructions of single transaxial slices. In contrast to the 2D mode, the three-dimensional (3D) data acquisition is additionally carried out for oblique planes, which obviously raises amount of data collected. Apart from the drastic raise in required computing power, 3D mode leads to better image quality at a comparable amount of injected activity.

The organization of the data acquired in 2D- and 3D mode is of great importance for PET. Data management has to meet the requirements of (i) beeing efficient in memory space and (ii) being appropriate for reconstruction algorithms. Mainly three structures of data fulfil these requirements which are described in the next lines:

List Mode (LM): As the name implies, LM records the coordinates of each event in a data stream. This stream is stored chronically and can consist of measurement informations like deposited energy or number of detectors as well as external data like count rate, or gating information. LM can reduce data storage and processing time when N_{LOR} is much greater than the number of recorded coincidences N_{event}.

[ix] The proportionality in 2.14 can be reasonably expected by assuming $r_\alpha \approx r_\beta$, a balanced count-rate of all detectors

LOR Histograms: A *true* event has already been described as an event where two annihilation photons reach the detectors on opposing sides of the detector geometry (see section 2.1.5 and figure 2.10). An imaginary line, the so called line of response

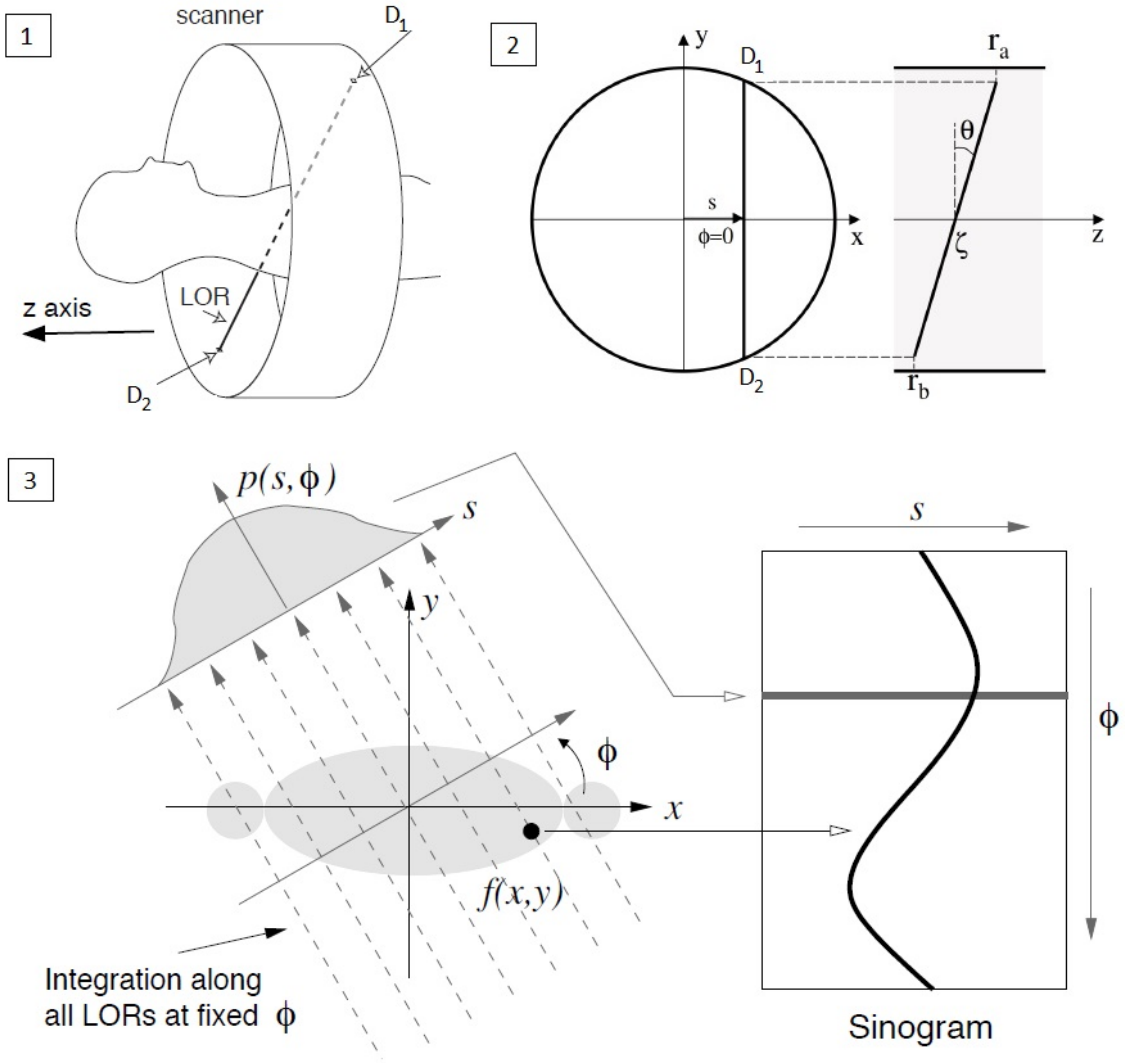

Figure 2.11: (1,2) Visualisation of a line of response (LOR) (3) Formation of a projection $p(s, \phi)$ - formed by integration along all parallel LORs at fixed angle ϕ - and a sinogram for a point source $f(x, y)$, where ϕ denotes the transaxial angle and s the radial distance from the center of the gantry (Alessio and Kinahan, 2006a)

(LOR), connects the two detectors involved in this true event and demonstrates that the annihilation took place somewhere on this line (see figure 2.11 - 1). A LOR histogram stores events for each LOR individually instead of listing all recorded coincidences with their corresponding timing information. Basically, LORs can be described in two different sets of variables, (i) with the detector pair (D_1, D_2) or (ii) with the triplet (s, ϕ, θ) consisting of radial distance, transaxial angle and axial angle (see figure 2.11 - 2).

Sinogram Data: Given a 2D activity distribution $f(x, y)$, projections of form

$$P(s, \phi) = \int_{-\infty}^{\infty} f(x, y) \; dy \tag{2.15}$$

are generated by integrating along all parallel LORs at an angle ϕ (see figure 2.11 - 3). In general, the mapping of $f(x.y) \rightarrow P(s, \phi)$ via line-integrals is called *X-ray transform*.

In 2D, these type of projections are called *Radon Transform* and consist of line-integrals over organized LORs for variable s and fixed ϕ. The matrix of all Radon transformations $P(s, \phi)$ corresponding to the angles $\phi \in [0; 2\pi]$ gives a sinogram. Therefore, sinograms plot each LOR as function of its angular orientation versus its displacement from center of gantry.

As can be seen in figure 2.11 - 3, a fixed point in object space corresponds to a sinusoidal path in the projection space. Superposition of all sinusoids forms sinograms for general objects.

2.2 Hybrid Technology

This section introduces physical basics of CT and Magnetic resonance imaging (MR) as well as the most important cornerstones in the development of PET including hybrid PET systems like PET/CT and PET/MR.

The very first PET scanner was developed by Phelps and colleagues (Phelps et al., 1975; Ter-Pogossian et al., 1975) in the 1970s. It was intended for human studies. Up to the late 90s, PET scanners were solely stand-alone devices providing good functional images but lacking anatomical information, both indispensable for clinical treatment. Since patient movement between separate CT or MR scans leads to difficulties in the co-registration process of two separate acquisitions, hybrid PET/CT systems were were developed in the late 90s (Beyer et al., 2000) to solve these issues. PET/MR systems were developed in the late 2000s (Judenhofer et al., 2008).

2.2.1 PET/CT System

Computed Tomography (CT): While a CT scan, a X-ray generator rotates around the exterminated object. Penetrating X-rays are attenuated by the object, and detected outside it. The measured attenuations are then converted into Hounsfield units (HU) that can be related to different tissue structures of the body,

finally achieving a good anatomical representation. The HU is defined as follows: In a voxel with linear attenuation μ_{VOX}, the corresponding HU value is given by

$$HU = 1000 \cdot \frac{\mu_{VOX} - \mu_{water}}{\mu_{water} - \mu_{air}} \tag{2.16}$$

where μ_{water} and μ_{air} are the linear attenuation coefficients of water and air.

PET/CT System: By combining PET and CT into a single device, a so-called PET/CT, the previously discussed lack of anatomical information of a standalone PET system can be avoided (Beyer et al., 2000; Townsend et al., 2003). Since the patient stays on the same table for both acquisitions, misalignments are reduced, image quality is increased and scanning time is minimised. Due to the demand of two CT scans, one for creating the attenuation correction map and another for anatomical imaging, patients are exposed to more radiation than in the separate scans (Huang et al., 2010).

The introduction of TOF improved the image quality of PET/CT (Akamatsu et

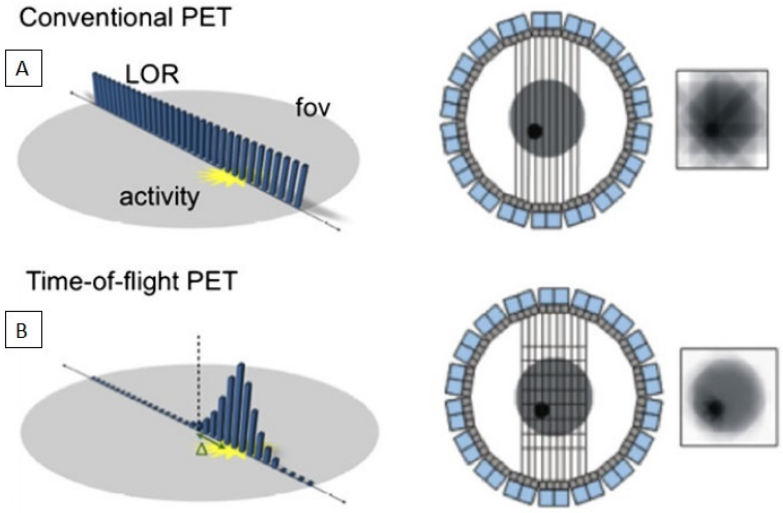

Figure 2.12: Comparison of conventional PET and TOF PET. (A) In conventional PET, there is equal probability for a recorded event along the LOR. (B)the incorporation of the time difference between the detection of photons creates a probability distribution locating the recorded event at distance Δ form the axis of the tomography (Beyer et al., 2011)

al., 2012; Vandenberghe et al., 2016a; Conti et al., 2011; Surti, 2016). TOF-PET not only takes into account the distance- and attenuation information, but adds the actual time difference between the detection of photons to the algorithm. As can be seen in figure 2.12, in conventional PET, there is equal probability for a recorded event along the LOR. Due to the incorporation of the time difference between the detection of photons, a probability distribution locating the recorded event at distance Δ form the axis of the tomography can be modeled (Beyer et al., 2011). This

leads to a higher sensitivity, signal-to-noise ratio and lesion contrast and lower image noise (Surti, 2015).

2.2.2 PET/MR System

Magnetic Resonance Imaging (MRI): Instead of X-rays, MRI uses magnetic fields to generate images. In presence of these strong magnetic fields, hydrogen atoms in the tissue are excited. These excited hydrogen atoms emit a radio frequency signal, which is measured by a receiving coil that is then processed to anatomical representations of the patients. Contrast between different tissue types is determined by the rate at which excited atoms return to the equilibrium state. (McRobbie, 2007)

PET/MR System: Another way of avoiding the lack of anatomical information of a standalone PET system is to combine PET with MR to a PET/MR system (Schlemmer et al., 2008; Pichler et al., 2006; Judenhofer et al., 2008). This reduces the radiation for the patient to solely the PET. Photomultiplier tubes (PMTs) are sensible to magnetic fields, this limitation was overcome by silicon photomultipliers (SiPMs) and avalanche photodiodes (APDs) (Lecomte, 2009). For more details see section 2.1.4.

2.3 Image Reconstruction

The aim of two-dimensional PET image reconstruction is to recover the (volume-) activity distribution that is available in image space by the use of data in projection space. The reconstruction process of tomographic imaging data is therefore mainly dependent on the mathematical tool of Fourier transformation.

In general, the related transformations from image space to projection space and vice versa can be obtained analytically or by the use of iterative algorithms. Both approaches are discussed in the following sections.

2.3.1 Analytic Methods

In this section, the basic idea of the Central Section Theorem is demonstrated, which is then used to introduce Filtered Back Projection.

Central Section Theorem: As already described in 2.1.5, the Radon transform, denoted by the operator X, is a integral operation that maps a function $f(x, y)$ on line integrals $p(s, \phi)$, called sinograms, so that

$$p(s, \phi) = (Xf(x, y))(s, \phi) \tag{2.17}$$

The central section theorem, often refereed to as the cornerstone of tomographic reconstruction, states that the 1D Fourier transform of the Radon transform 2.17 at a given angle ϕ is related to the 2D Fourier transform of the image f at the same angle ϕ by

$$P(\nu, \phi) = (\mathcal{F}p(s, \phi))(\nu, \phi) = \int_{\mathbb{R}_2} ds\ (s, \phi)\, e^{-2\pi i s\nu} \tag{2.18}$$

where ν is the frequency. By applying data for all angles $\phi \in [0; \pi]$, the complete image reconstruction process can be broken down to 2D Fourier Transformation.

Filtered Back Projection (FBP): Filtered Back Projection is a standard algorithm in analytical image reconstruction, using a filter function $h(s)$ to create filtered projections

$$p^F(s, \phi) = \int ds' p(s', \phi) \cdot h(s - s') \tag{2.19}$$

that are mapped on f by the back-projection operator $X^\star$, in a way that

$$f(x, y) = \left(X^\star p^F\right)(x, y) = \int_0^\pi d\phi\ p^F(s, \phi) \tag{2.20}$$

As can be seen in figure 2.13, FBP performs a Fourier transform of all angular

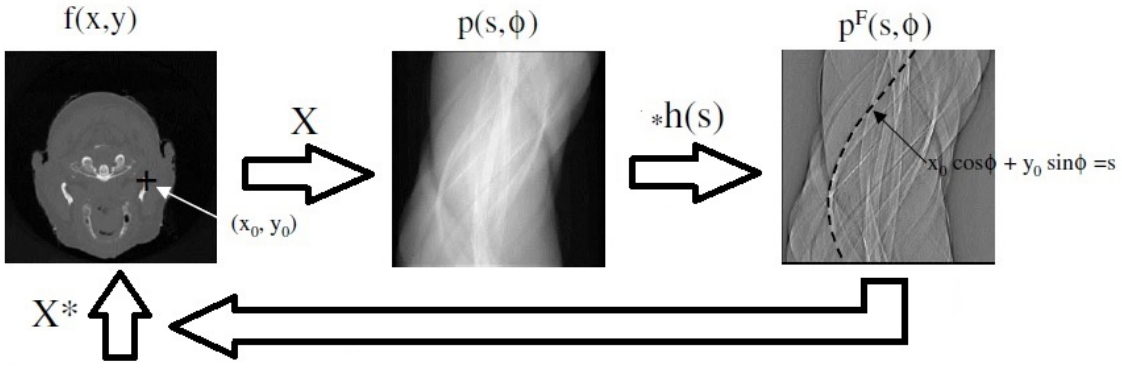

Figure 2.13: Scheme of Filtered Back Projection (FBP) Algorithm - Fourier transforms of projections are filtered in the frequency domain and back-transformed (adapted and rearranged (Bailey et al., 2005))

projections, applies a filter $h(s)$ in the frequency domain and back-transforms via

$X^{\star}$.

When handling noise free projection data, FBP leads to accurate reconstruction of activity distribution. However, the introduction of errors in image observation, FBP can quickly lead to artefacts or noise. By incorporating stochastic system-information to the solution, these issues can be overcome. This process increases the complexity and leads to the use of iterative methods of image reconstruction.

2.3.2 Iterative Methods

As already mentioned above, analytic algorithms can lead to mathematically correct solutions that are afflicted with artefacts, when dealing with noisy data. This is due to the lack of system modelling in analytic algorithms which lead to complex mathematical problems, only to be handled by iterative approaches.

Basically, the principle of any iterative algorithm is to find solutions by consecutive

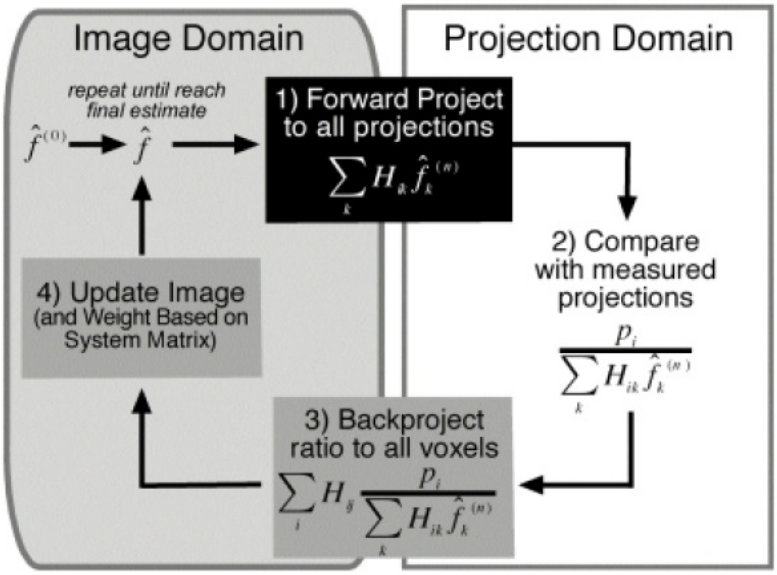

Figure 2.14: Maximum-Likelihood Expectation Maximization (MLEM) Algorithm (Alessio and Kinahan, 2006a)

estimates, that are compared to measured data sets. On basis of the comparison of estimated and available data, the current estimate is modified leading directly to a new estimate that can again be compared and modified. Iterative methods differ in the way of data comparison and correction. In direct reconstruction methods, significant changes in the algorithm need to be done when increasing the dimensionality of the system from 2D to 3D. In contrast, except for the more complex projector-backprojector pairs and the higher computation power, in iterative reconstruction algorithms, going from 2D to 3D systems does not

require significant changes in the reconstruction algorithm. A popular approach for modelling informations of system, image and data is the Ordered Subsets Expectation Maximization (OSEM) method (Hudson and Larkin, 1994) that is based on the Maximum-Likelihood Expectation Maximization (ML-EM) algorithm (Shepp and Vardi, 1994). Both are described in the following lines.

Maximum-Likelihood Expectation Maximization (ML-EM): Maximum-Likelihood Expectation Maximization is widely used in PET and includes a Poisson likelihood coast function to map the current image estimate $\hat{f}^n$ on the next estimate $\hat{f}^{n+1}$ in a way that (Alessio and Kinahan, 2006a)

$$\hat{f}_i^{n+1} = \hat{f}_i^n \underbrace{\frac{1}{\underbrace{\sum_{j=i} a_{j',i}}_{sensitivity}}}_{backprojection} \underbrace{\sum_{j=1}^{N} a_{j,i} \frac{p_j}{\underbrace{\sum_{j=i} a_{j,i'} \hat{f}_{i'}^n}_{forwardprojection}}}_{backprojection} \quad i = 1, ..., P \tag{2.21}$$

The flowchart 2.14 illustrates the basic structure of ML-EM (2.21). Starting by comparing the calculated projections of an initial guess $\hat{f}^{(0)}$ with the measured projections, correction factors are obtained in projection space. These factors are then back-projected and voxel-wise applied on the system matrix. The obtained values serve as new image estimate. Note that each iteration performs one forward and one back-projection which can affect computing time.

Ordered-Subsets Expectation Maximization (OSEM): Ordered-Subsets Expectation Maximization is an improvement of ML-EM that performs weighting and backprojecting separately (Munoz et al., 2016). OSEM reaches a similar solution X times faster than the corresponding ML-EM by dividing the projections into X subsets.

2.4 Standard Data Corrections and Quantification

Apart from photon attenuation in the patient body, there exist various other quantification errors that affect the accuracy and precision of PET measurements. These are for example count-rate losses or unwanted scattered and random coincidences. This section presents three of the most common corrections of quantification errors in PET.

2.4.1 Attenuation

As already discussed in section 2.1.5, a coincidence is dependent on simultaneous detection of both photons arising from the annihilation of a positron. Accordingly, coincidence will not occur if (i) photons are absorbed in the body or (ii) photons are scattered out of the Field of View (FOV). When defining B as the total thickness of the body, $exp(0)$ and $exp\,(-\mu B)$ in 2.22 represent the probability for near and far detectors, which leads to the number of detected coincidences (Gopal, 2010)

$$C = C_0\ e^0 e^{(-\mu B)} = C_0\ e^{(-\mu B)} \tag{2.22}$$

Correcting for photon attenuation in the body is therefore the task of estimation of the probability of photon attenuation. This needs to be done for all sources along the line of response (LOR).

The most common approaches of determining the probability of photon attenuation are (i) measuring attenuation correction by blank scans, using coincidence- or singles transmission data or (ii) calculating attenuation correction for each coincidence line. Attenuation correction maps (μ-maps) can also be acquired by computed tomography (CT) or magnetic resonance imaging (MRI) (Zaidi and Hasegawa, 2003).

While transmission scans create μ-maps by the use of sources that emit photons at similar energies to the annihilation photons (Bailey, 1998), CT scans use the attenuation of X-rays that is extrapolated to 511 keV to obtain μ-maps (Kinahan et al., 1998) while the emission scan. The fraction that is absorbed along a line of response (LOR) in a transmission scan can be used to correct the emission scan data. MR based μ-maps are calculated by the measured parameters of proton density and relaxation. Nevertheless, it needs to be stated, that the problem of MR-based attenuation correction is not straightforward, as the MR image is not directly related to photon attenuation, and therefore is not fully solved yet. This is especially true for regions other than the brain (Rausch et al., 2017; Mehranian et al., 2016; Ladefoged et al., 2017).

2.4.2 Scatter

Besides photon attenuation, photon scattering in the body or in the PET detectors need to be corrected for. Besides the, in section 2.1.3 already discussed, Compton Effect that is the most likely interaction at 511 keV, annihilation photons can undergo various other scatter-events. This wide variety leads to numerous approaches for scatter estimation and scatter correction that can be structured in four categories: (1) empirical approaches (Cherry et al., 1993, 1995), (2) methods involving energy windows (Harrison et al., 1991; Thompson, 1993), (3) convolution methods (Bailey et al., 1994; Bergstrom et al., 1983) and (4) methods that simulate

the scatter distribution via analytical or Monte Carlo simulations (Hasegawa et al., 2002; Barney et al., 1991). In general, the obtained scatter correction can be (i) subtracted from the sinogram or (ii) added in the system model, with the second option being preferable to preserve the Poisson statistical nature of data.

2.4.3 Randoms

Image quality can also be reduced by random coincidences (see section 2.1.5), that introduce a uniform background noise, leading to reduction of the image contrast. Random coincidences are proportional to the coincidence timing window and to the amount of activity within the FOV. Reduction of this timing window minimizes the collection of random coincidences. Therefore, a simple possibility of estimating the number of random coincidences involves the singles rate and the coincidence time window. In all Siemens systems a delayed CTW is used for the estimation of randoms. The obtained scatter correction can be subtracted from the prompts or added to the system model, with the second option being preferable to preserve the Poisson statistical nature of data.

2.5 Motion Compensation

Basically, patient motion can be classified in voluntary and involuntary motion processes. Voluntary movement is characterised by the conscious decision of moving for example one arm the PET acquisition is performed. Involuntary movements are caused for example by internal organs, like the pumping of the heart, that cannot be consciously controlled by the patient. In PET imaging, motion causes a degradation of image quality in terms of blurring, smearing and, thus, reduction of measured activity concentration (Liu et al., 2009).

Further, artefacts arising from motion induced misalignment of the activity concentration with the PET data can cause significant image quality and PET quantification impairment (see figure 2.15) (Lassen et al., 2017; Rausch et al., 2017; Ouyang et al., 2013). This results in a reduction of spatial resolution of the PET activity distribution and therefore a reduction of reliability in clinical image interpretation.

Respiratory motion

Respiratory motion consists of an inspiration phase where contraction of intercostal muscles and diaphragm fills the lungs with air and an expiration phase, where this process is inverted to expel air form the lungs. Breath holding is a simple but not

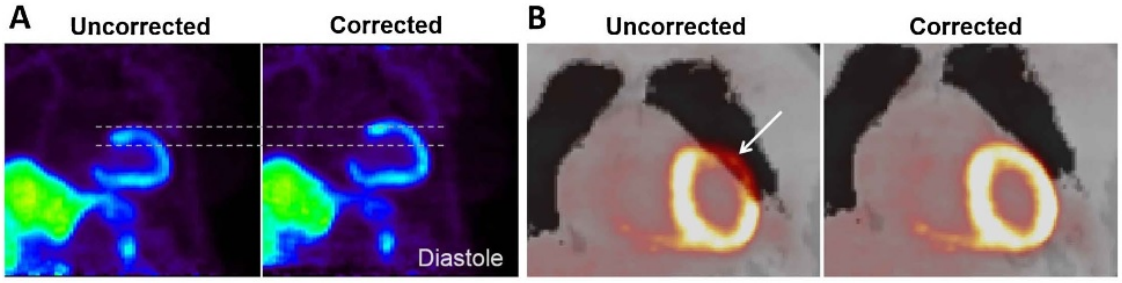

Figure 2.15: Effect of respiratory and cardiac motion on PET image quality - (A) Blurring effect due to cardiac motion and (B) Motion-induced artifact due to miss-registration (Rausch et al., 2017)

applicable way of minimizing the effects of respiratory motion, due to the long time required to perform a PET acquisition, in the order to several minutes.

Another approach is respiratory gating, where the respiratory signal is divided into bins, at the cost of increased noise in the reconstructed PET-images. This can be done as a function of time or amplitude and presented in histograms (Dawood et al., 2007; Jani et al., 2013).

Historically, hardware-based methods for motion detection have been the standard. Most common hardware-based methods use sensors, cameras or belts to track physiological characteristics related to the organ's movement and create a motion model (McClelland et al., 2013). Especially in PET/CT, advanced methods for respiratory motion tracking use the monitoring of the changes in temperature of the air in the oral area (Pepin et al., 2014). Unfortunately, most hardware-based methods for motion correction have limitations (e.g. complicated and time-consuming set-up, partially faulty controls, etc.). For this reason, alternative data-driven approaches, using the PET or the MR raw-data, have been proposed. For example, in PET/MR, motion can be derived directly from the MR data. This approach is called self-navigation and detects the breathing motion by acquiring a central profile in k-space and comparing each projection to a reference position that is obtained in the learning stage (Uribe et al., 2007).

Cardiac motion

Cardiac motion is a very complex motion that involves longitudinal and radial contractions as well as rotations (Sengupta et al., 2006). In a similar way to the gating of respiratory motion, also cardiac motion can be divided into short frames to reduce the effect of motion. It needs to be stressed, that motion effects can be reduced using these approaches, but at the same time the SNR in the resulting images is lowered.

Several methods for minimizing cardiac motion for PET/MR have been proposed (Scott et al., 2009). Nevertheless Electrocardiography (ECG)-based gating is the most widely used in PET. For this approach, electrocardiography data is used, that is measured while the PET examination.

Another method, called cardiac self-gating, eliminates the use for (ECG)-based gating by obtaining a cardiac signal directly from the MR data (Larson et al., 2004). Similarly to the respiratory self-navigation approach, also cardiac self-gating uses profiles of the k-space to model the cardiac motion (Crowe et al., 2004).

2.5.1 Motion Compensation Techniques

Approaches towards respiratory and/or cardiac gating are commonly used to reduce motion-induced blurring in PET images, whereby the emission data is divided into gates that correspond to different respiratory or cardiac phases. Therefore, the simplest approach (and most used in clinical routine) is respiratory and/or cardiac gating, at the cost of increased noise in the reconstructed PET-images. However, a more preferable solution is to perform motion compensation (MoCo) using the full data-acquisition, both to reduce acquisition times and to improve the signal-to-noise ratios in the PET images.

All Motion Compensation (MoCo) techniques rely on the existence of information about patient motion. Basically, MoCo techniques can be classified according to the type and timing of incorporation of the motion information into the image reconstruction (IR) process (Rahmim et al., 2013; Feng et al., 2016).

Pre-reconstruction techniques: Pre-reconstruction techniques incorporate the motion information before the IR process. By the use of nearest neighbour interpolation, a specific LOR is transformed and assigned to another LOR. This is done by a transformation matrix that is derived from the input of the motion-information (Lassen et al., 2015; Livieratos et al., 2005).

Reconstruction techniques: Reconstruction techniques incorporate the motion information while the IR process. Linear interpolation is used to calculate a so-called motion-warping operator that is combined with the original system matrix, resulting in an updated system-matrix, containing motion-information (Tsoumpas et al., 2013; Polycarpou et al., 2012).

Post-reconstruction techniques: Post-reconstruction techniques incorporate the motion information after the IR process. Already reconstructed images are shifted to a common reference frame. The shifts are given by the motion fields. The final image is given by the sum of all shifted pictures (Picard, 1997).

Popular motion compensation approaches of the above-listed will be discussed in more detail in the following sections. Section 2.5.2 highlights list-mode- and sinogram-based approaches, that are examples of the pre-reconstruction technique, section 2.5.3 gives an overview of the reconstruction technique Motion Compensated Image Reconstruction and section 2.5.4 discusses the post-reconstruction technique Reconstruct-Transform-Average.

2.5.2 Projection-Based Motion Compensation

P-MoCo belongs to the category of so-called pre-reconstruction techniques, therefore P-MoCo incorporates the motion information before the image reconstruction (IR) process. There exist mainly two approaches to correct for motion before the IR process, namely (i) histogram/sinogram based approaches or (ii) List-Mode based approaches.

One popular approach of List-Mode Motion Compensation, the so-called List-Mode

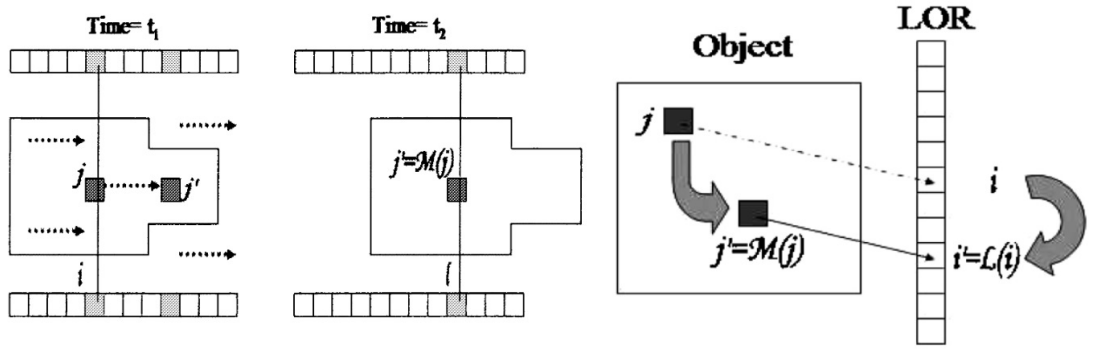

Figure 2.16: Simplified process of List-Mode Motion Compensation (Rahmim et al., 2004) - List-Mode Motion Compensation shifts a LOR i', generated originally by an event in voxel j, that is due to motion translated to voxel $j' = \mathcal{M}(j)$, back to the position $i = \mathcal{L}^{-1}(i)$ that corresponds to the position where the LOR would have been detected if the object had not moved.

Expectation Maximization (LM-EM), works directly with LOR coordinates. It basically shifts a LOR i', generated originally by an event in voxel j, that is due to motion translated to $j' = \mathcal{M}(j)$, back to the position $i = \mathcal{L}^{-1}(i)$ that corresponds to the position where the LOR would have been detected if the object had not moved (Rahmim et al., 2004). This process is further illustrated in figure 2.16. After LM-EM, the reorganized LM-data is therefore corrected for motion and can be further

processed.

A closely related process can be used for histogram/sinogram based approaches. As the LM gives the sinogram bin of each coincidence event, the only difference lies in the movement of the data. While list-mode based approaches move the projected data event-by-event, histogram/sinogram based approaches move the already histogrammed data.

2.5.3 Motion Compensated Image Reconstruction

Motion Compensated Image Reconstruction (MCIR) belongs to the category of reconstruction techniques, therefore MCIR incorporates the motion information while the IR process. The standard Ordered-Subsets Expectation Maximization (OSEM)

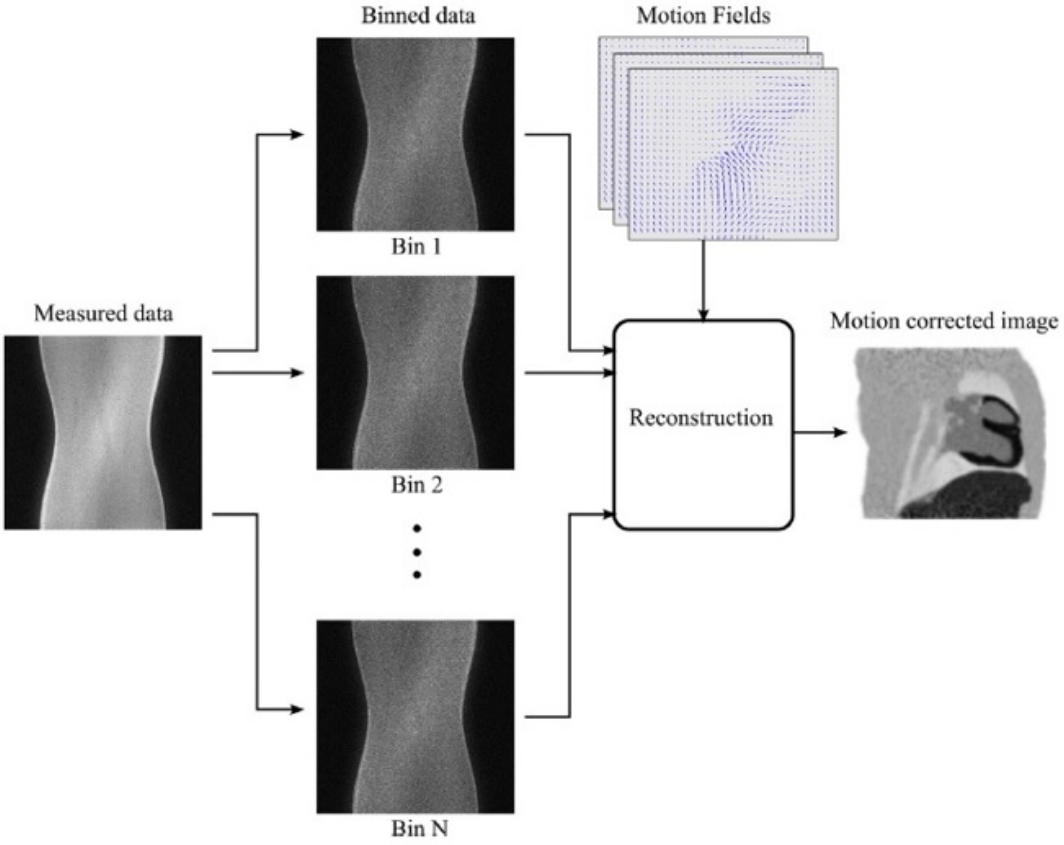

Figure 2.17: Simplified flowchart of Motion Compensated Image Reconstruction (MCIR) from (Munoz et al., 2016) - Measured sinogram data is binned into N bins that are reconstructed to a motion corrected image, using a reconstruction an algorithm with a system matrix that is modified with motion fields

algorithm, that is already discussed in chapter 2.3.2, can be updated to the MCIR

algorithm by including motion information in the system matrix (Polycarpou et al., 2012).

Figure 2.17 sketches the basic concept of MCIR. The measured PET sinogram data is binned in N individual motion-free frames, so called bins. This is done to alleviate reconstruction time. Every bin is then reconstructed in a way that motion information is directly incorporated while the reconstruction process by updating the PET system matrix. The incorporation of motion information therefore modifies the emission and attenuation maps. After the reconstruction process with the modified system matrix, a motion corrected image is obtained.

2.5.4 Reconstruct-Transform-Average

Reconstruct-Transform-Average (RTA) belongs to the post-reconstruction techniques, therefore RTA incorporates the motion information after the IR process. Figure 2.18 sketches the basic concept of RTA. Again, the measured PET sinogram

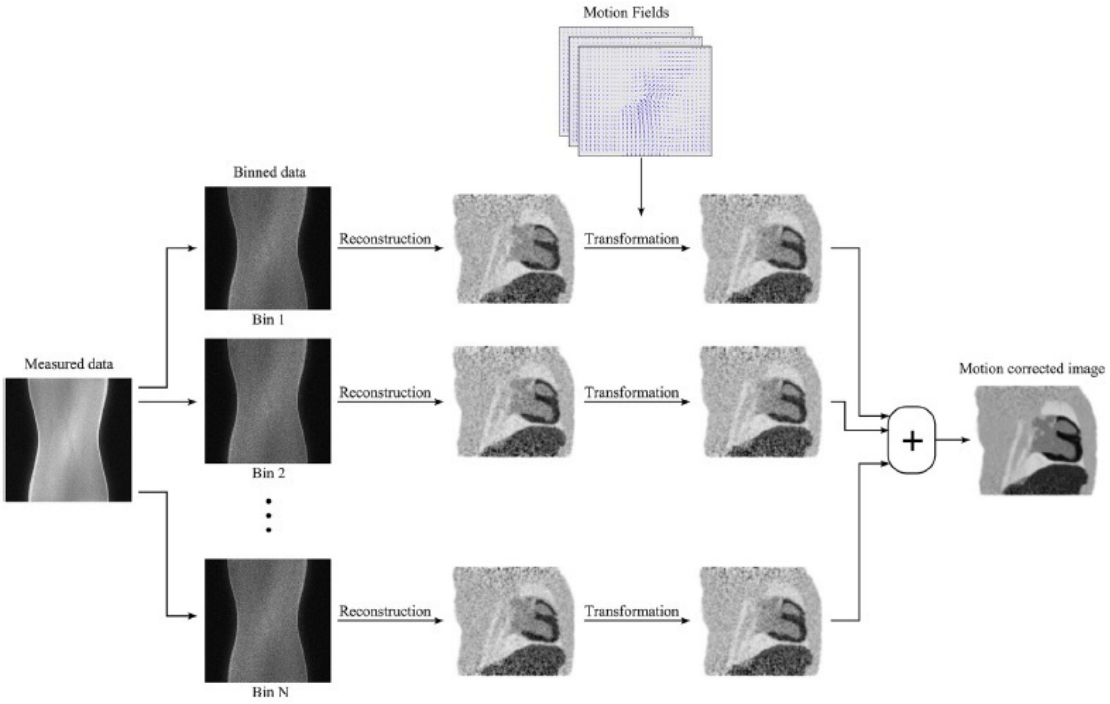

Figure 2.18: Simplified flowchart of Reconstruct-Transform-Average (RTA) from (Munoz et al., 2016) - Measured sinogram data is binned into N bins that are individually reconstructed and warped to a reference bin by transforms with inverted motion fields. Averaging leads to the motion compensated image

data is binned in N individual motion-free frames. Each frame is then reconstructed independently, using a standard image reconstruction algorithm, providing N indi-

vidual reconstructed bins. After the reconstruction, the motion information is applied. This is done by warping $N-1$ reconstructed bins from different motion states to a pre-selected common reference bin N_0 by the use of inverse motion field transformations. In the last step, all bins are averaged to obtain the final motion-corrected image (Picard, 1997).

3. Methodology

This chapter introduces the Biograph mMR system (section 3.1), gives a brief overview over the used motion compensation approaches (section 3.2), includig Projection Based Motion Compensation (P-Moco), Motion Compensated Image Reconstruction (MCIR) as well as the Reconstruct Transform Average (RTA) method. Phantom data, including Numerical phantom and the XCAT phantom, are highlighted (section 3.3) and image quality analysis (section 3.4) are described. Finally, a short introduction to the evaluated patient data (section 3.5) concludes this chapter.

3.1 Biograph mMR

The Siemens Biograph mMR system (figure 3.1), located at Allgemeines Krankenhaus (AKH) Wien, was used. Biograph mMR is the first clinical simultaneous PET/MR hybrid system (Delso et al.; 2011).

The PET component consists of 448 detector blocks, arranged in 8 detector rings of 56 detector blocks each. Every block is built of 8×8 crystal elements with 3×3 avalanche photodiodes (APD). In total, Biograph mMR consists of 64 crystal rings, providing an axial and radial field of view (FOV) of 258 mm and 588 mm.

Figure 3.1: Siemens Biograph mMR (Muzic, DiFilippo, 2014)

The MR component is a compilation of a 3 T niobium-titanium superconductor magnet, a radio-frequency body coil with peak power of 35 kW and a whole-body gradient coil system. A detailed information of all

specifications of the Siemens Biograph mMR can be found in table 3.1.

Table 3.1: Specifications of the Siemens Biograph mMR (from Delso et al. (2011))

MR component	
Magnet	3 T
Gradient coil: strength	$45\,\mathrm{mT\,m^{-1}}$
Gradient coil: slew rate	$200\,\mathrm{mT\,m^{-1}\,s^{-1}}$
Radiofrequency coil: peak power:	35 kW
Radiofrequency coil: transmitter bandwidth	800 kHz
PET component	
Detector rings	8
Axial spacing	0.40625 mm
Detector blocks (per detector ring)	56
Crystal elements (per detector block)	8×8
Size of crystal elements [mm×mm×mm]	4×4×20
Avalanche photodiodes (per detector block)	3×3
Axial FOV [mm]	258

3.2 Motion Compensation Approaches

As already discussed in chapter 2.5, to compensate for patient motion, different motion compensation (MoCo) methods were developed and proposed in the literature. They can be classified as Pre-reconstruction-, Reconstruction- and Post-reconstruction techniques, according to the timing of incorporation of the motion information into the Image Reconstruction (IR) process (see figure 3.2).

Three MoCo approaches were chosen and tested on different phantom- and motion

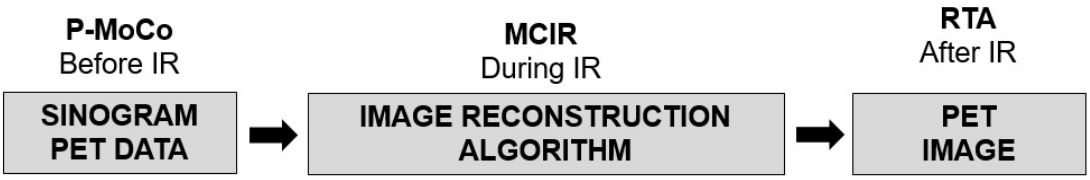

Figure 3.2: Different Motion Compensation Approaches listed according to the timing of incorporation of the motion information into the image reconstruction (IR) process (top) combined with an oversimplified flowchart of PET image reconstruction (bottom) - Projection-Based Motion Compensation (P- MoCo) incorporates the motion-information before the IR process, Motion-Compensated Image Reconstruction (MCIR) incorporates the motion-information during the IR process and Reconstruct-Transform- Average (RTA) incorporates the motion-information after the IR process

models: *Projection-Based Motion Compensation* (P- MoCo) that incorporates the motion-information before the IR process, *Motion-Compensated Image Reconstruction* (MCIR) that incorporates the motion-information during the IR process and *Reconstruct-Transform- Average* (RTA) which incorporates the motion-information after the IR process. All approaches are described in detail in the following sections.

3.2.1 Projection-Based Motion Compensation

Projection-Based Motion Compensation (P-MoCo) incorporates the motion information before the image reconstruction process. Figure 3.3 sketches the basic concept of P-MoCo. P-MoCo can be divided in four main steps. Starting from (i) *ideal sinogram projections*, the motion fields are incorporated by the (ii) *co-registration process*, leading to a (iii) *motion-compensated sinogram*. This sinogram can then be (iv) *reconstructed using a standard reconstruction algorithm*. In the next lines these four steps are further specified.

P-MoCo is a completely data driven approach which automatically extracts the

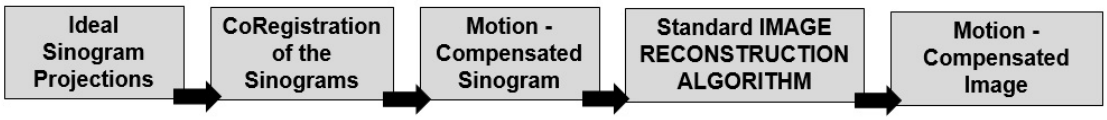

Figure 3.3: Simplified flowchart of Projection-Based Motion Compensation (P-MoCo) - Ideal sinogram projections are co-registered with the motion fields to obtain a motion compensated sinogram that is then processed with the OSEM algorithm

respiratory signal from the LM file. The extracted respiratory signal is then used for gating. In a further step, respiratory motion vector fields are extracted from the gated data. The extracted respiratory motion fields are then applied to the prompt and delayed events in the original LM, to create a new LM file that is now compensated for motion. After normalisation, respiratory-motion compensated sinograms are obtained (Lassen et al., 2018).

This respiratory-motion compensated sinograms was reconstructed using a standard reconstruction algorithm. Here, the Ordered-Subsets Expectation Maximization (OSEM) algorithm was used to obtain the motion compensated image. This was done with the well-known iterative algorithm Ordered Subsets Maximum a posteriori One-step-late (OSMAPOSL) (Green, 1990a,b) which is freely available within the Software for Tomographic Image Reconstruction (STIR) library (Thielemans et al., 2012).

3.2.2 Motion Compensated Image Reconstruction

The Motion Compensated Image Reconstruction (MCIR) approach, that incorporates the motion-information during the IR process, is based on an iterative algorithm with a common regularization approach, namely the OSMAPOSL (Green, 1990a,b). OSMAPOSL was extended to include motion information in order to reconstruct all gates into one reference frame (Tsoumpas et al., 2013). Equation 3.2 describes the incorporation the motion compensation within the system matrix (Tsoumpas et al., 2013)

$$\Lambda_{\nu}^{(s+1)} = \Lambda_{\nu}^{(s)} \frac{1}{\sum_{b\in S_l,g}\sum_{\acute{\nu}} \hat{W}^{-1}_{\acute{\nu}g\to\nu} P_{\acute{\nu}b} A_{bg} + \beta \Delta_{\Lambda_\nu} E_{\nu}^{(s)}} \times \sum_{b\in S_l,g}\sum_{\acute{\nu}} \left(\hat{W}^{-1}_{\acute{\nu}g\to\nu} P_{\acute{\nu}b} \frac{Y_{bg}}{\sum_{\acute{\nu}} P_{b\tilde{\nu}} \sum_{\check{\nu}} \hat{W}_{\check{\nu}\to\tilde{\nu}g} \Lambda_{\check{\nu}}^{(s)} + \frac{B_{bg}}{A_{bg}}} \right) \tag{3.1}$$

Here, $\Lambda_{\nu}^{(s)}$ is the estimated radioactivity at voxel ν and sub-iteration s, Y_{bg} is the number of measured coincident photons of each detector pair b that belongs to the l^{th} subset S and gate g. S_l is the l^{th} subset of the projection space, which is divided into a total of L subsets and s is the sub-iteration number. $P_{b\nu}$ is the system projection matrix, A_{bg} the attenuation coefficient for bin b and gate g and finally B_{bg} corresponds to the background term (e.g. scatter) for bin b and gate g.

The MCIR approach makes use of so-called warping operations $\hat{W}$ and $\hat{W}^{-1}$ that move the activity form one location to another. $\hat{W}$ represents the forward warping operations of the image that moves the activity from voxel ν' to voxel ν, using the motion fields and linear interpolation. $\hat{W}^{-1}$ represents the backward warping operations. Therefore $\hat{W}^{-1}$ acts to warp all gates to the reference gate, while $\hat{W}$ acts the opposite way.

The motion vector fields that are incorporated in equation 3.2 were estimated from the co-registration of previously reconstructed gated PET images to a chosen reference gate. This co-registration process was done in Matlab, using the Medical Image Registration Toolbox (MIRT) software (Myronenko and Song, 2010).

3.2.3 Reconstruct-Transform-Average

The Reconstruct-Transform-Average (RTA) approach used for motion correction incorporates the motion-information after the IR process and consists of the independent reconstructions of each frame, that are then transformed to a reference frame and averaged (Picard, 1997).

The independent reconstructions of each gate were calculated by (Tsoumpas et al., 2013)

$$\Lambda_{\nu g}^{(s+1)} = \Lambda_{\nu g}^{(s)} \frac{1}{\sum_{b \in S_l} P_{\nu b} A_{bg} + \beta_g \Delta_{\Lambda_{\nu g}} E_{\nu}^{(s)}} \sum_{b \in S_l} P_{b\nu} \frac{Y_{bg}}{\sum_{\tilde{\nu}} P_{b\tilde{\nu}} \Lambda_{\tilde{\nu} g}^{(s)} + \frac{B_{bg}}{A_{bg}}} \tag{3.2}$$

where

$$\beta_g \Delta_{\Lambda_{\nu g}} E_{\nu}^{(s)} \stackrel{def}{=} \beta_g \frac{\Lambda_{\nu g}^{(s)} - M_{\nu}^{(s)}}{M_{\nu}^{(s)}} \tag{3.3}$$

$\Lambda_{\nu g}^{(s)}$ corresponds to the estimated radioactivity at voxel ν and gate g at sub-iteration s, Y_{bg} is the number of measured coincident photons of each detector pair b that belongs to the l^{th} subset S and gate g. S_l is the l^{th} subset of the projection space. $P_{\nu b}$ is the system projection matrix, A_{bg} the attenuation coefficient for bin b and gate g and finally B_{bg} corresponds to the background term (e.g. scatter) for bin b and gate g. In equation 3.3, β_g are the penalization factors that were set to zero for the reconstructions .

Equation 3.4 describes the transformation step that is followed after reconstruction of all gates

$$\Lambda_{\nu} = \frac{1}{G} \sum_{g} \sum_{\nu'} \hat{W}_{\nu' g \rightarrow \nu}^{-1} \Lambda_{\nu' g} \tag{3.4}$$

Here, G denotes the total number of gates and $\hat{W}^{-1}$ denotes the represents the backward warping operation that moves the activity from voxel ν' to voxel ν, using the motion fields and linear interpolation.

Again, the motion vector fields that are incorporated in equation 3.4 were estimated from the co-registration of previously reconstructed gated PET images to a chosen reference gate. This co-registration process was done in Matlab, using the MIRT software (Myronenko and Song, 2010).

3.3 Phantom Data

Simulated acquisitions of a 4D XCAT phantom (Segars et al., 2010), as well as a numerical phantom obtained from real MR acquisitions (Tsoumpas et al., 2011), were used for the evaluation of the motion compensation (MoCo) approaches described in chapter 3.2. Both phantoms and the simulated motion patterns are described in more detail in the sections below.

3.3.1 XCAT Phantom

It is well known, that voxelized phantoms were very realistic, limited in their abilities to model patient motion. Mathematical models, on the other hand, are due to their mathematical definitions flexible to model patient data, but are limited realistic due to the simplicity of the used equations.

The 4D extended cardiac-torso (XCAT) phantom is a whole-body adult male and female model (see figure 3.5) overcomes these limitations by combining the advantages of both types of phantoms. This computational phantom is able to simulate different respiratory and cardiac motion models.

Different respiratory motion patterns were applied on the XCAT phantom, that differ in the complexity level of motion. As can be seen in figure 3.4 and table 3.2, one-dimensional motion was simulated as 2 cm superior-inferior heart motion and two-dimensional movement of the heart was simulated as a combination of 2 cm superior-inferior and 1 cm anterior-posterior heart motion.

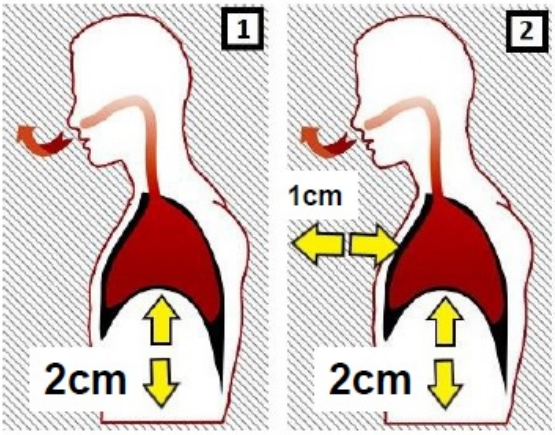

Figure 3.4: Simulated motion of the XCAT phantom - (1) 1D motion 2 cm superior-inferior heart motion, (2) 2D motion a combination of 2 cm superior-inferior and 1 cm anterior-posterior heart motion

The following SUV values were used in both simulations: soft tissue = 2, liver = 7, myocardium = 18, lumen = 5, ribs 3. The respiratory motion was simulated for 5 gates, including both randoms, scatter and Poisson noise, to mimic a patient acquisition (Tsoumpas et al., 2011; Cal-González et al., 2017).

Simulated acquisitions of the XCAT phantom, including different complexity levels of motion, were reconstructed using Ordered Subset Expectation Maximization (OSEM), Motion-Compensated Image Reconstruction (MCIR), Reconstruct-Transform-Average (RTA) and Projection-Based Motion Compensation (P-MoCo). Furthermore, every single gate was reconstructed using OSEM (OSEM-gated) and also a static acquisition without any motion (No Motion) was simulated and evaluated. The simulated reconstructions were performed using the Software for Tomographic Image Reconstruction (STIR) (Thielemans et al., 2012).

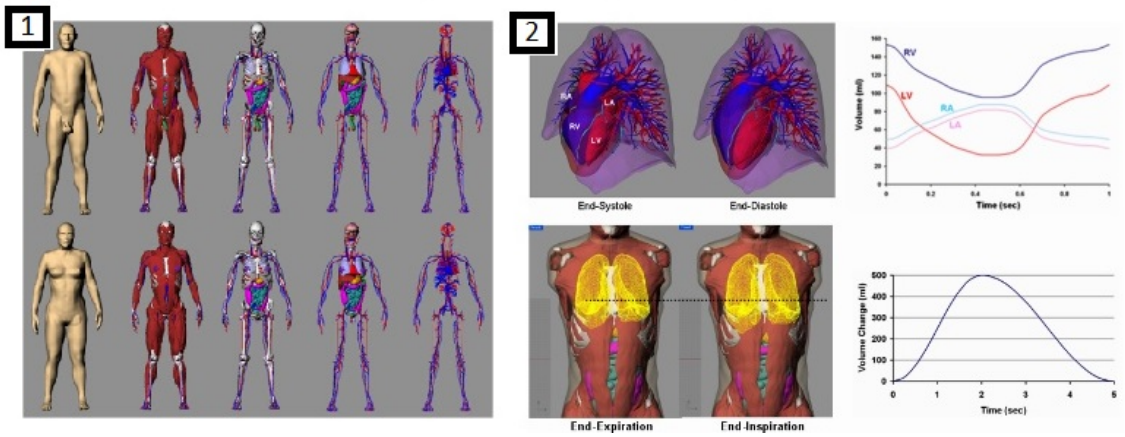

Figure 3.5: The 4D extended cardiac-torso (XCAT) phantom - (1) Levels of detail of male (top) and female (bottom) anatomies of the XCAT, (2) Cardiac and respiratory motions of the XCAT (Segars et al., 2010)

3.3.2 Numerical Phantom

The numerical phantom is a series of MR-based 4D PET/MR datasets (Tsoumpas et al., 2011a). This thorax phantom is capable of mimicking respiratory and cardiac motion. It contains two spherical hot lesions, simulating atherosclerotic plaque lesions, and one cold lesion within the myocardium, which mimics an infarcted area with reduced FDG uptake (see figure 3.6).

Different respiratory motion patterns were applied on the numerical phantom, that

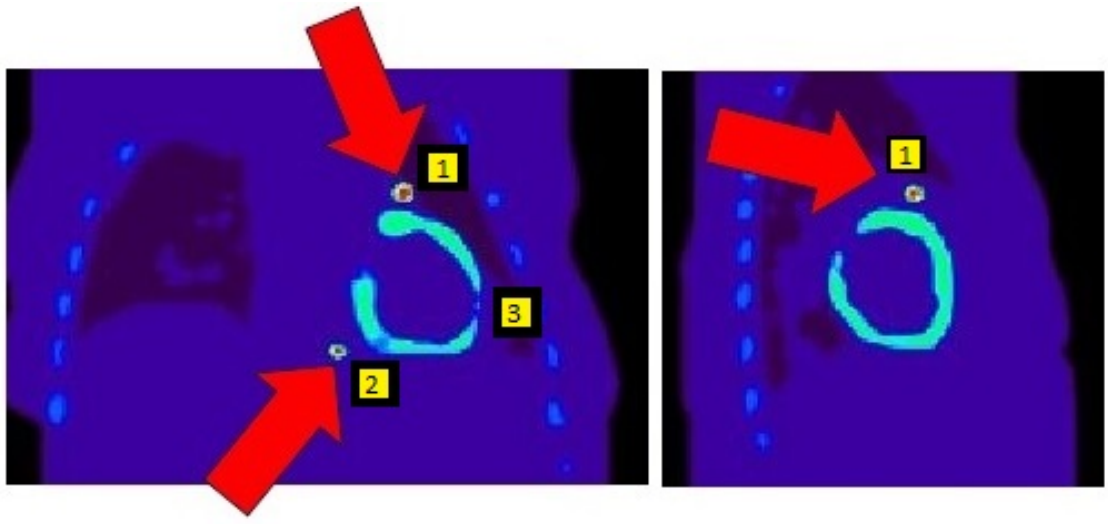

Figure 3.6: Numerical Phantom - Coronal and Sagital plane of the thorax phantom with highlighted lesions - (1,2) spherical hot lesions, simulating atherosclerotic plaque lesions and (3) cold lesion within the myocardium that mimics an infarcted area with reduced FDG uptake

differ in the complexity level of motion. First, a simple approach to respiratory motion consisting of one-dimensional respiratory motion solely in the axial direction. Then two more sophisticated approaches to respiratory motion, involving respiratory and cardiac motion in two and three spatial dimensions (see table 3.2). Cardiac motion is clearly visible since the appearence of the heart in different gates changes cardiac phases.

As described in Cal-González et al. (2017), Attenuation maps were created, using an ultra-short time-echo (UTE) sequence. The simulated motion vector fields were estimated using a dynamic MR sequence (35 dynamic frames, 0.7 s duration each) during normal breathing. FDG-PET standardized uptake values (SUV) were assigned to the segmented regions of the MR images. Scatter was simulated analytically using the single scatter simulation formula (Watson, 2000), random events summing in total a 30 % of the simulated counts, were approximated as a uniform background. Poisson noise was included to simulate a levels of 500 million counts.

The numerical phantom, including different complexity levels of motion, was re-

Table 3.2: Overview of simulated motion parameters for XCAT Phantom and Numerical Phantom - For XCAT Phantom the total simulated myocardium motion is listed, for Numerical Phantom simulated motion of hot lesion 1 and hot lesion 2 as well as simulated upper and lower myocardium motion is listed

Phantom (Region)	Motion	Axial Movement	Anterior-Posterior Movement
XCAT (tot. Myoc.)	Respiratory (1D)	2.00 cm	0.00 cm
	Respiratory (2D)	2.00 cm	1.00 cm
Numerical (Hot Les. nr. 1)	Respiratory (1D)	0.68 cm	0.00 cm
	Respiratory-Cardiac (2D/3D)	1.21 cm	0.97 cm
Numerical (Hot Les. nr. 2)	Respiratory (1D)	0.75 cm	0.00 cm
	Respiratory-Cardiac (2D/3D)	1.03 cm	0.43 cm
Numerical (upper Myoc.)	Respiratory (1D)	1.29 cm	0.00 cm
	Respiratory-Cardiac (2D/3D)	0.69 cm	1.03 cm
Numerical (lower Myoc.)	Respiratory (1D)	0.63 cm	0.00 cm
	Respiratory-Cardiac (2D/3D)	0.35 cm	0.48 cm

constructed using Ordered Subset Expectation Maximization (OSEM), Motion-Compensated Image Reconstruction (MCIR), Reconstruct-Transform-Average (RTA)

and Projection-Based Motion Compensation (P-MoCo). Furthermore, every single gate was reconstructed using OSEM (OSEM-gated). For the sake of comparison, also a static image (No Motion) was evaluated. The simulated reconstructions were performed using the Software for Tomographic Image Reconstruction (STIR) (Thielemans et al., 2012).

3.4 Image Quality Analysis

To evaluate the effect of the motion compensation (MoCo) approaches for the different motion patterns, all PET images are quantified by the use of different figures of merit, including SNR, L2B or M2B. Besides this, a bias- as well as a breakdown analysis was performed which will be discussed in the next sections.

All MoCo approaches described in section 3.2 were performed by using 5 iteration-cycles with 21 subsets each, adding up to a total number of 105 sub-iterations. After each iteration (every 21^st sub-iteration), reconstructed images were stored and different figures of merit (see sections below) were calculated to comparatively evaluate the performance and convergence of the implemented algorithms for the numerical phantom and the XCAT phantom. Moreover, Full Width at Half Maximum (FWHM) Gaussian filtering was applied after each iteration in all reconstructions.

3.4.1 Bias-Analysis

A Region of Interest (ROI) analysis of the heart was performed with the motion-corrected images of the numerical phantom and the XCAT phantom by segmenting the lesions and the myocardium. A reference frame was chosen as background, using the lumen region of the heart or the liver. The corresponding mean activity 3.5 measured within the segmented area A_{SEG} of the ROI is

$$S_{\xi=L,M,B} = \sum_{VOX_\xi \in A_{SEG}} VOX_\xi \tag{3.5}$$

where VOX_ξ is the measured activity of one voxel of the tissue-type ξ in A_{SEG}. Therefore S_L is the measured activity within the segmented lesion, S_M the measured activity within the segmented myocardium and S_B the measured activity within the segmented background.

CNR was calculated as the absolute difference $|S_{\xi=L,M} - S_B|$ divided by the standard deviation σ_B

$$CNR = \frac{|S_{L,M} - S_B|}{\sigma_B} \tag{3.6}$$

and SNR was calculated as a measure of the logarithmic fraction of $S_{\xi=L,M}$ and the root mean square (RMS) of the measured activity within the segmented background

$$SNR = 20 \cdot log_{10}\left(\frac{S_{L,M}}{RMS\,(S_B)}\right) \tag{3.7}$$

Also a bias analysis was performed. The activity bias within the segmented lesions was calculated by comparison to a reference image

$$bias\ (\%) = \left(\frac{mean\,(S_L) - mean\,(S_{REF})}{mean\,(S_{REF})}\right) \cdot 100 \tag{3.8}$$

The figures of merit for the XCAT phantom were calculated by means of a Myocardium to Background Ratio (M2B) where S_{My} is measured activity within the segmented myocardium and $S_{B=Li,Lu}$ corresponds to measured activity within the segmented background region in the liver ($S_{B=Li}$) or the lumen($S_{B=Lu}$).

3.4.2 Breakdown-Analysis

In another part of the Image Quality (IQ) analysis, a breakdown analysis was performed. This includes the computation of lesion-to-background-ratio (L2B).

The performance of the MoCo approaches in different stages of simulated motion-complexity was tested using the mean activity $mean\,(S_L)$ within the segmented lesion for the Numerical Phantom and the mean activity $mean\,(S_{My})$ within the segmented Myocardium for the XCAT Phantom, and comparing them to the mean value of the selected background regions for the respective phantom

$$L2B = \frac{mean\,(S_L)}{mean\,(S_B)} \quad \text{or} \quad M2B = \frac{mean\,(S_{My})}{mean\,(S_{B=Li,Lu})} \tag{3.9}$$

To highlight the performance breakdown of the MoCo approaches in different stages of simulated motion-complexity, the maximum activity of 3.9 within the segmented lesion S_L was used for the Numerical Phantom

$$L2B_{max} = \frac{max\,(S_L)}{mean\,(S_B)} \quad \text{or} \quad M2B_{max} = \frac{max\,(S_{My})}{mean\,(S_{B=Li,Lu})} \tag{3.10}$$

or the the maximum activity of 3.10 within the segmented myocardium S_{My} was used for the XCAT Phantom, and compared to the mean value of the selected background regions for the respective phantom.

3.4.3 Stability-Analysis

In a concluding part of the image quality analysis, a stability analysis was performed. This includes the computation of a the absolute differences

$$\Delta L2B_{2D-1D}(X_i) = abs\left[L2B_{2D}(s) - L2B_{1D}(s)\right]_{s_{max}} \tag{3.11}$$

$$\Delta L2B_{3D-1D}(X_i) = abs\left[L2B_{3D}(s) - L2B_{1D}(s)\right]_{s_{max}} \tag{3.12}$$

of L2B 3.9 for the Numerical Phantom, or the absolute differences

$$\Delta M2B_{2D-1D}(X_i) = abs\left[M2B_{2D}(s) - M2B_{1D}(s)\right]_{s_{max}} \tag{3.13}$$

of M2B 3.9 for the XCAT Phantom, for different dimensions, evaluated at the last subiteration s_{max}, that are directly liked to the stability of the motion-compensation approach X_i.

The stability-criteria was selected as follows - The MoCo-approach X_i is stable compared to the approach X_j, if the absolute difference of L2B or M2B for different dimensions are in a comparable range ζ, therefore

$$L2B_{2D-1D}\left(X_i\right) \approx L2B_{3D-1D}\left(X_i\right) \approx L2B_{2D-1D}\left(X_j\right) \approx L2B_{3D-1D}\left(X_j\right) \approx \zeta \tag{3.14}$$

for the Numerical Phantom and

$$M2B_{2D-1D}\left(X_i\right) \approx M2B_{2D-1D}\left(X_j\right) \approx \zeta \tag{3.15}$$

for the XCAT Phantom.

3.5 Patient Data

Besides the in-depth-analysis of two simulated phantoms, capable of respiratory motion or cardiac motion, two patients were selected for a proof of concept analysis.

The selected patients were scanned using the fully-integrated PET/MR system Siemens Biograph mMR (see section 3.1). With all patients, myocardial perfusion imaging was done employing the tracer NH_3 with activities of 845 ± 133 MBq. Also metabolism studies were employed using the tracer FDG with the activity of 339 ± 31 MBq. To enable a good distribution of the tracer in the myocardium, all studies of motion-compensation evaluated on PET-emission data from the last 10 minutes of the acquisitions. For a detailed description of the imaging protocol see Lassen et al. (2018) and figure 3.7.

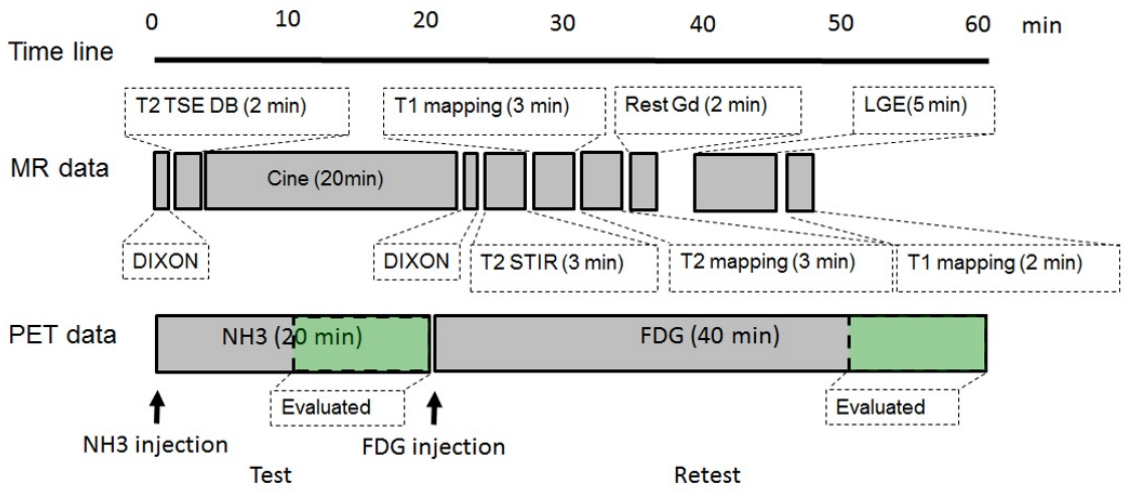

Figure 3.7: Flow-chart of the dual-tracer PET/MRI protocol - consisting of a simultaneous acquisitions of PET-based myocardial perfusion imaging employing NH_3 and cine-acquisitions in the MR system. Myocardial viability was assessed through simultaneous acquisitions of PET employing FDG, rest and late-gadolinium enhancement imaging protocols (Lassen et al., 2018)

Therefore, a total of four patient data-sets were reconstructed, using Ordered Subset Expectation Maximization (OSEM), Reconstruct-Transform-Average (RTA) and Projection-Based Motion Compensation (P-MoCo). Furthermore, every single gate was reconstructed using OSEM (OSEM-gated). No Motion Compensated Image Reconstruction (MCIR) evaluations were included in the patient datasets, due to unexpected artefacts observed in some of the reconstructions. All reconstructions were performed using the Software for Tomographic Image Reconstruction (STIR) (Thielemans et al., 2012).

To be consistent with the former phantom studies, all reconstructions were performed by using 5 iteration-cycles with 21 subsets each, adding up to a total number of 105 sub-iterations. After each iteration (every 21^{st} sub-iteration), reconstructed images were stored and different figures of merit (see sections below) were calculated to comparatively evaluate the performance and convergence of the implemented algorithms. Again, FWHM Gaussian filtering was applied after each iteration in all reconstructions.

The performance of the different MoCo methods for patient-data was tested in terms of the ratio of mean activity $mean\,(S_{My})$ within the segmented Myocardium and mean activity $mean\,(S_{B=Lu})$ of the selected background region (lumen) for the respective phantom (see equation 3.9).

4. Results

In this chapter, the main results of the conducted motion compensations are presented. Section 4.1 discusses the results from the XCAT phantom simulations, section 4.2 discusses the performance of the motion compensation in numerical phantom simulations and finally, section 4.3 shows the results from the analysis of patient data.

4.1 XCAT Phantom

A comparison of reconstructed images of the 4D extended cardiac-torso (XCAT) phantom for different levels of respiratory motion complexity (1D-2D) is presented in this section. First, a comparison of Ordered Subset Expectation Maximization (OSEM), Motion-Compensated Image Reconstruction (MCIR), Reconstruct-Transform-Average (RTA) and Projection-Based Motion Compensation (P-MoCo), single gates (OSEM-gated) and static images (No-Motion) is presented (section 4.1.1). Furthermore, the performance of the MoCo methods is tested by means of a bias analysis (section 4.1.2) as well as a stability-analysis (section 4.1.3).

4.1.1 Reconstructed Images

Figure 4.1 illustrates coronal plane slices of the reconstructed images of the XCAT phantom with corresponding cardiac Line Profiles for different levels of motion complexity. In contrast to the numerical phantom (see section 4.2) that is capable of simulation respiratory and cardiac motion, the XCAT phantom only performs respiratory motion of different complexity levels. Simple one dimensional (1D) superior-inferior heart motion, as well as complex two dimensional (2D) heart motion including a mixture of superior-inferior and anterior-posterior plane motion (for details see section 3.3.1) was analysed.

A visual inspection and comparison of the reconstructed images (figure 4.1) leads to

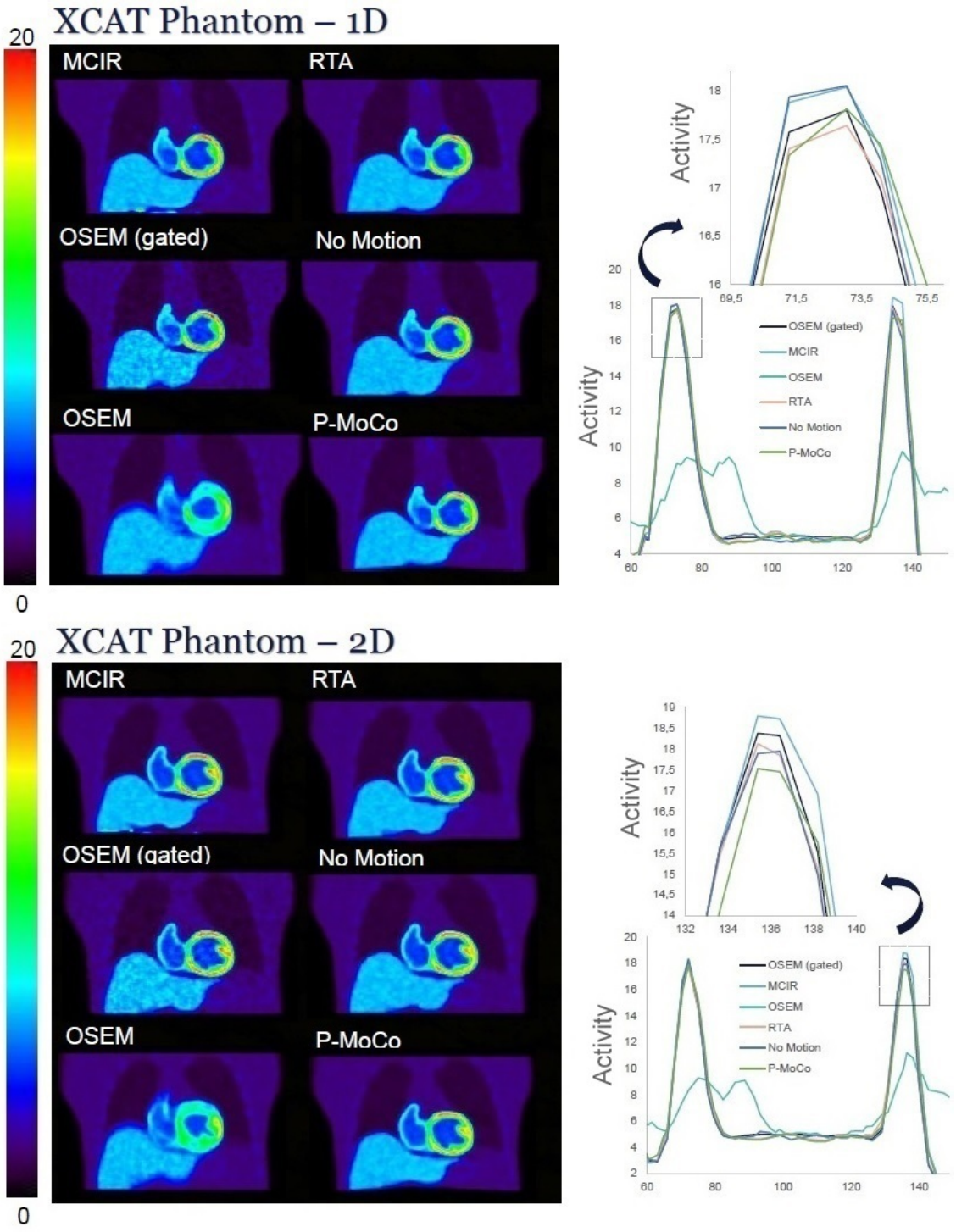

Figure 4.1: Numerical Phantom - Comparison of OSEM, RTA, MCIR, P-MoCo, Gated and No-Motion for 3D movement with corresponding Line Profile

the subjective and qualitative statement that P-MoCo, MCIR and RTA yield good image quality. In terms of image contrast, the blurring of the activity distribution

or the noise, P-MoCo, MCIR and RTA seem comparable to Gated and No-Motion images. Solely OSEM Reconstructed images show clear losses of image quality, with

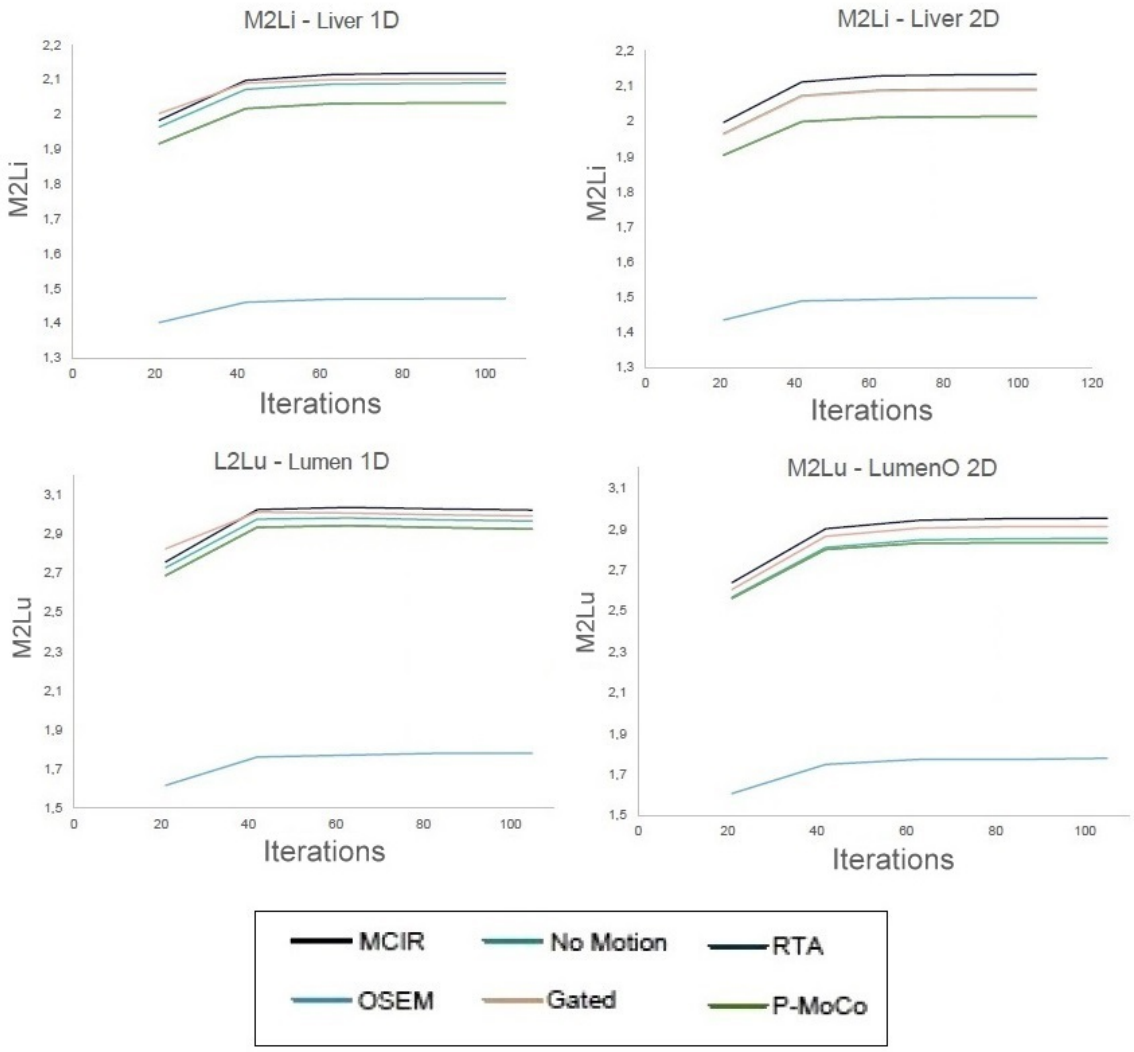

Figure 4.2: XCAT Phantom - Myocardium to Liver and Myocardium to Lumen Ratio for 1D and 2D movement of OSEM, RTA, MCIR, P-MoCo, Gated and No-Motion

significant losses in the contrast of the image.

After visual inspection, a quantitative analysis of line profiles through the myocardium was conducted. Image blurring and noise in the OSEM reconstruction was directly validated by the comparison of the width of the line profiles of the different MoCo approaches. OSEM differs up to 44 % in FWHM of the myocardium peak in the 1D line profile and even up to 63 % of the myocardium peak in the 2D line profile. Furthermore it turned out that the maximum activity of OSEM reconstructions nearly halved in comparison to the other MoCo approaches. Besides OSEM all other reconstructions yield a comparable range in terms of activity.

Closer analysis of the maximum activity reveals a comparable performance of MCIR and No-Motion as well as P- MoCo and Gated followed by RTA. This is valid for simple 1D respiratory motion. For the more realistic 2D respiratory motion MCIR and RTA surpass the maximum activity of P-MoCo.

4.1.2 Bias Analysis

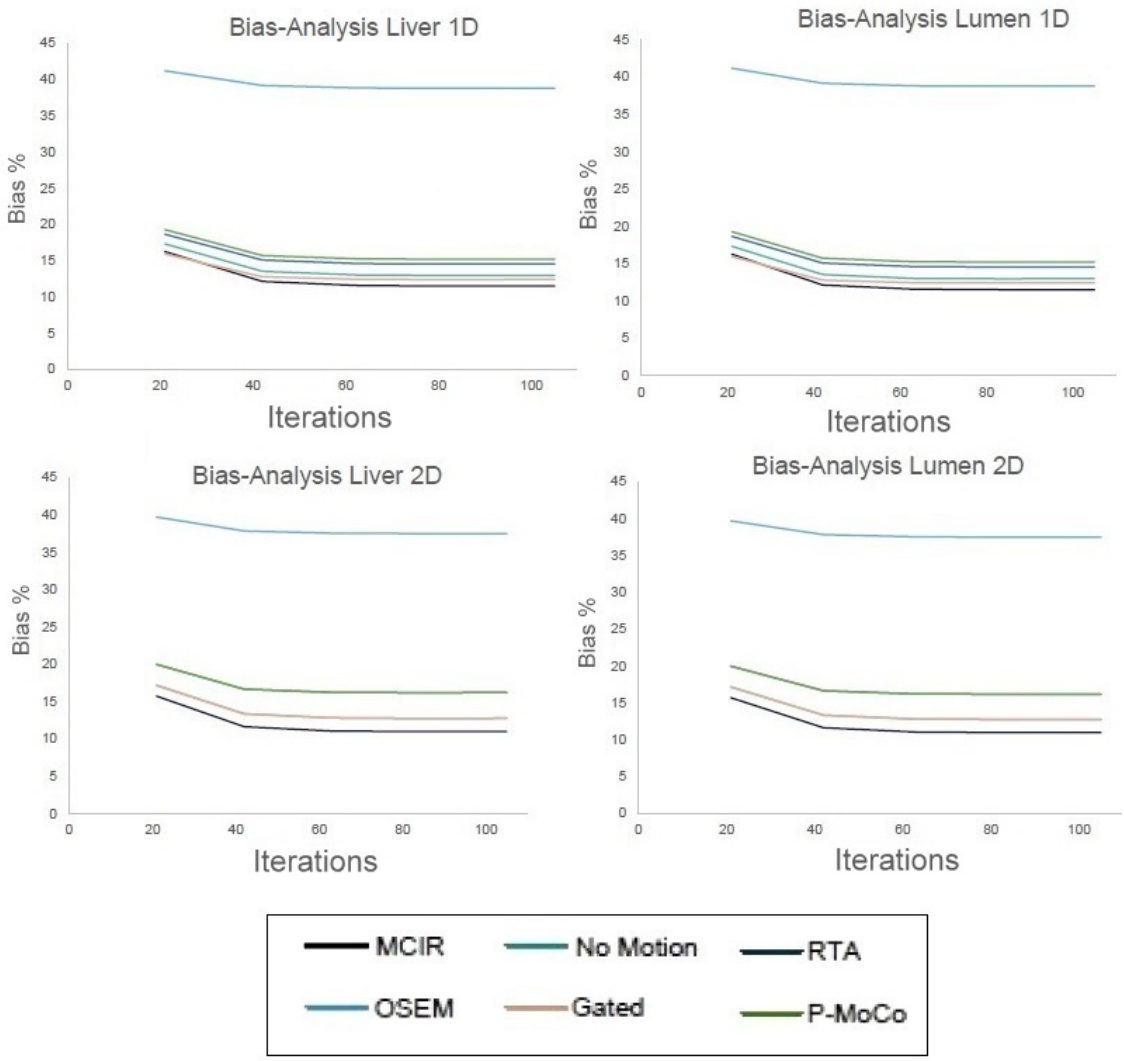

Figure 4.3: XCAT Phantom - Bias analysis for 1D and 2D movement of OSEM, RTA, MCIR, P-MoCo, Gated and No-Motion

In a further analysis step, the performance of the different MoCo approaches was tested by means of reference to different tissue types, namely lumen and liver. Myocardium-to-Liver (M2Li) ratio and Myocardium-to-Lumen (M2Lu) ratio analysis as well as Bias analysis for lumen and liver was conducted and compared. Both

image quality measures were implemented for 1D and 2D respiratory motion. A comparison of M2Li and M2Lu are given in figure 4.2. The outcome of the bias analysis for lumen and liver can be found in figure 4.3.

When analysing solely the myocardium and liver contributions in plots 4.2 and 4.3 one can conclude that MCIR, No-Motion and Gated yield comparable image quality for 1D-motion, for 2D respiratory motion only MCIR and No-Motion give comparable results. The performance of P-Moco and RTA for 1D-motion and 2D-motion is nearly identical. This behaviour was also obtained by analysing solely myocardium and lumen. Also in this measurement set-up, image quality of MCIR surpasses the nearly identical image quality of P-MoCo and RTA.

4.1.3 Stability Analysis

In a concluding analysis step, the evidence that MCIR, RTA and P-MoCo performance is not affected by simple 1D and complex 2D respiratory motion was validated by a stability analysis.

A direct comparison of the performance of P-MoCo, MCIR and RTA throughout the

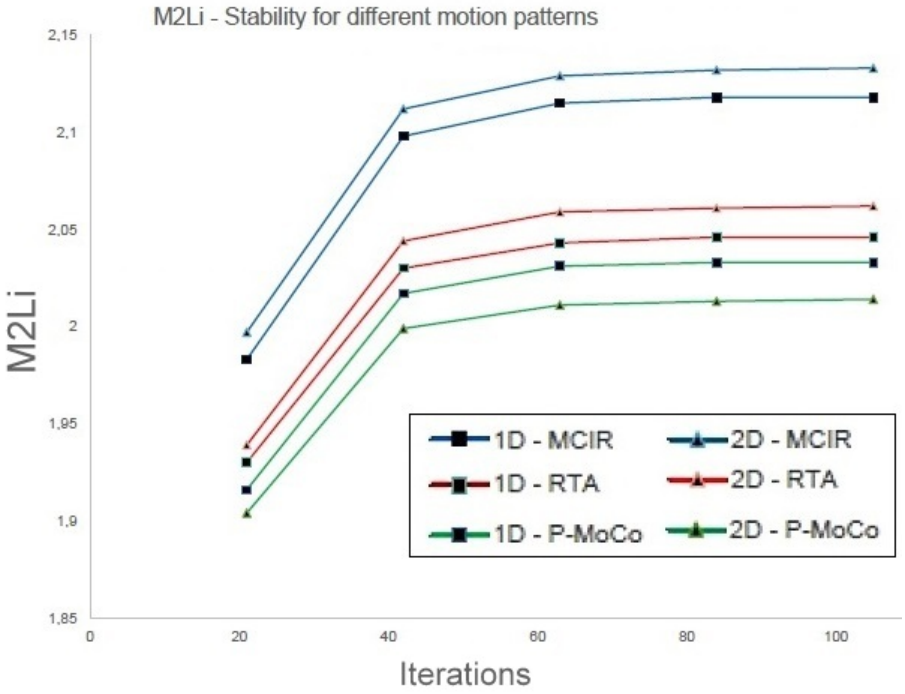

Figure 4.4: XCAT Phantom - Stability of Myocardium to Liver (M2Li) Ratio of RTA, MCIR and P-MoCo for 1D and 2D movement

full range of respiratory motion complexity (1D-2D) can be seen in figure 4.4. The

absolute difference of $M2Li_{1D}$ and $M2Li_{2D}$ in figure 4.4 stays nearly constant for all MoCo approaches. For MCIR an absolute difference of $15 \cdot 10^{-3}$ was measured, for RTA an absolute difference of $16 \cdot 10^{-3}$ was obtained and P-MoCo leaded to an absolute difference of $19 \cdot 10^{-3}$.

4.2 Numerical Phantom

In this section, a comparison of reconstructed images of the numerical phantom for different levels of motion complexity (1D-3D) are presented. In detail, a comparison of Ordered Subset Expectation Maximization (OSEM), Motion-Compensated Image Reconstruction (MCIR), Reconstruct-Transform-Average (RTA) and Projection-Based Motion Compensation (P-MoCo), single gates (OSEM-gated) and static images (No-Motion) is presented (section 4.2.1). Furthermore, the performance of the different MoCo approaches is tested by means of bias, stability and separability analyses (sections 4.2.2, 4.2.3 and 4.2.4).

4.2.1 Reconstructed Images

Figure 4.5, 4.6 and 4.7 illustrate coronal views of the reconstructed images of the numerical phantom with corresponding cardiac Line Profiles for different levels of motion complexity. One dimensional motion represents simple respiratory motion in the

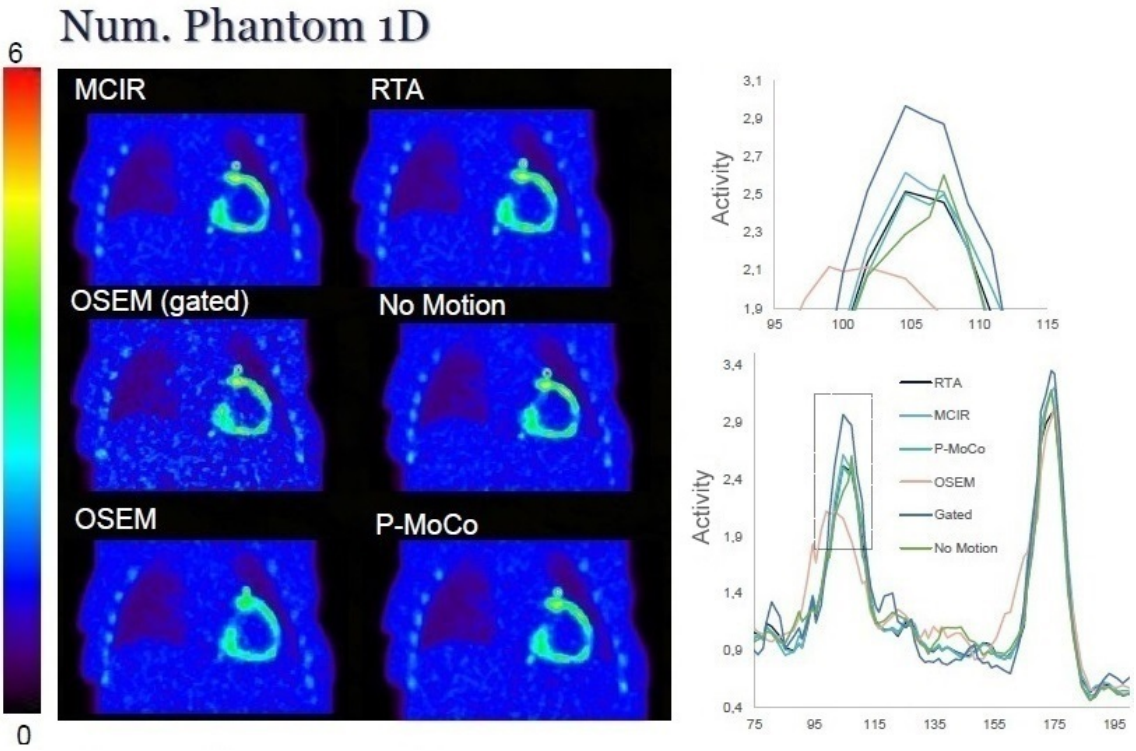

Figure 4.5: Numerical Phantom - Comparison of OSEM, RTA, MCIR, P-MoCo, Gated and No-Motion for 1D movement with corresponding Line Profile

coronal plane, two- and three dimensional motion represents complex respiratory- and cardiac motion patterns in coronal and sagital plane.

In a first analysis step, visual inspection and comparison of the reconstructed images leads to subjective and qualitative statements, that are then, in a second analysis step, supported by the quantitative analysis of obtained Line Profiles.

Visual inspection and comparison of the reconstructed images leads to the following

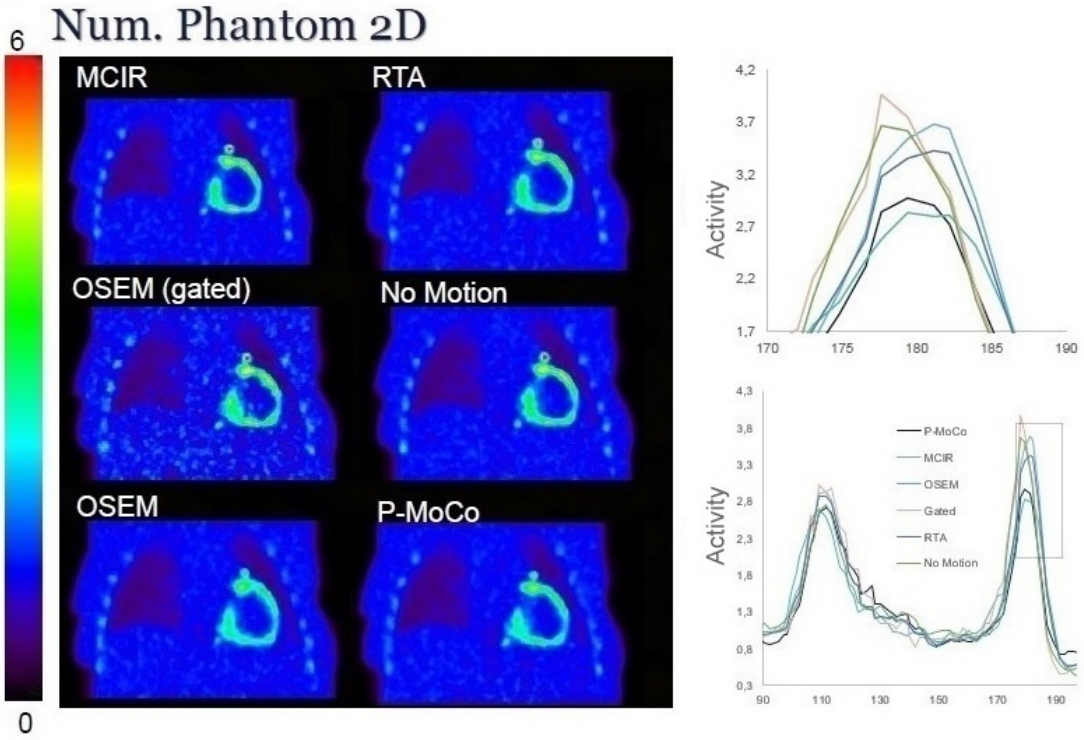

Figure 4.6: Numerical Phantom - Comparison of OSEM, RTA, MCIR, P-MoCo, Gated and No-Motion for 2D movement with corresponding Line Profile

qualitative statements:

- Throughout all motion-patterns (1D-3D) Gated and No-Motion give best results in terms of noise and contrast.
- MCIR and RTA provide good and comparable image quality throughout all motion-patterns. This is mainly seen in a sharp and clear activity distribution in the lesions and the myocardium
- One can see a reduction of image quality for P-MoCo when increasing motion complexity. This is mainly seen by the fact, that by increasing the dimensionality of motion, P-Moco matches OSEM more and more, which in all cases gives the least image quality.

All qualitative statements that are mentioned above can be validated by the quantitative analysis of cardiac line profiles that can be found besides the reconstructed images in figures 4.5, 4.6 and 4.7.

As expected, the maximum activity in all motion patterns is achieved by Gated

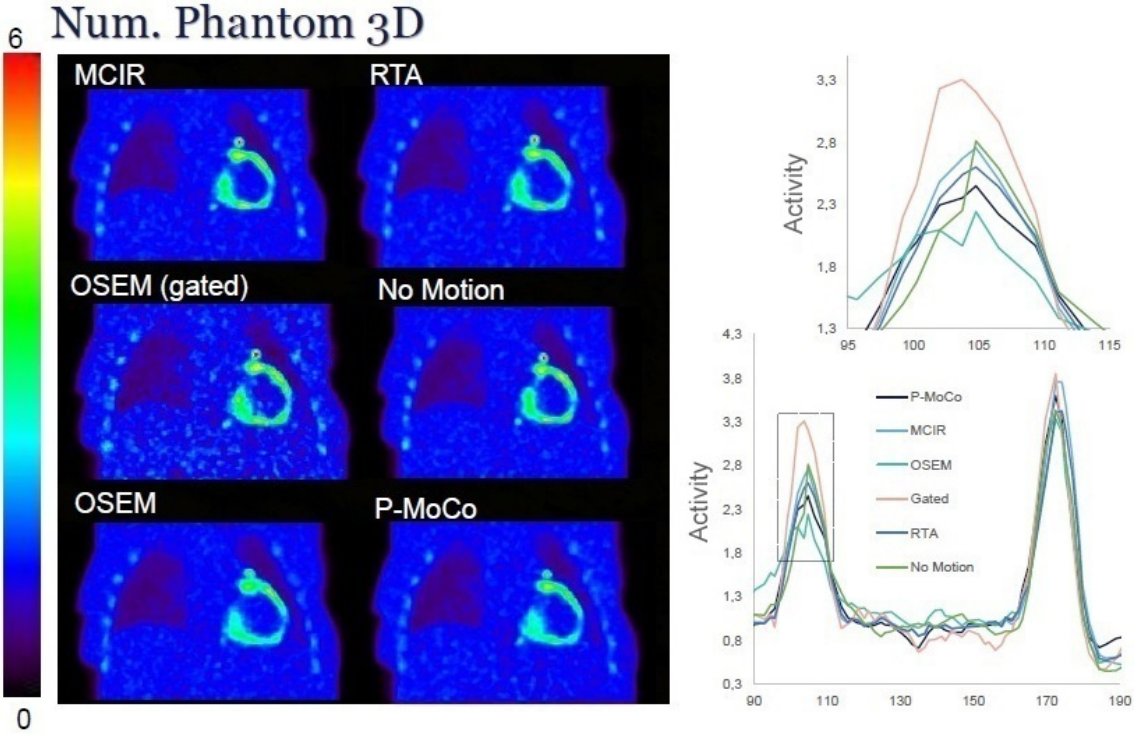

Figure 4.7: Numerical Phantom - Comparison of OSEM, RTA, MCIR, P-MoCo, Gated and No-Motion for 3D movement with corresponding Line Profile

and No-Motion, followed by MCIR and RTA. The stated reduction of image quality for P-MoCo for complex motion patterns is clearly visible in the line profiles. While the maximum activity of P-MoCo and OSEM differs significantly for 1D motion (0.6 SUV), this difference reduces drastically for 2D (0.2 SUV) and 3D motion (0.1 SUV). The FWHM of line profiles can directly be connected to the blurring of the activity distribution in a given region of the image. Especially for 1D motion, one can see a clear effect of image blurring in OSEM reconstruction, when comparing FWHM of the activity distribution of OSEM to the one of MCIR, RTA or P-MoCo. A total change of FWHM of up to 46 % was seen when comparing the three MoCo approaches for 1D motion. For 2D and 3D motion, this change reduces to 10 %.

4.2.2 Bias Analysis

The Maximum Lesion to Background (LBR_{max}) ratio can be found in figure 4.8. The Lesion-to-Background Ratio (LBR) of the hot Lesions as well as the Bias Analysis for the numerical phantom can be found in figure 4.9. The results for 1D, 2D and 3D motion reflect the observed behaviour described in section 4.2.1.

Besides the unsurpassed performance of Gated and No-Motion images, MCIR and RTA reconstruction yield comparable and stable LBR in respiratory and cardiac motion. As can be seen in the bias analysis, especially for respiratory motion (1D), the image quality of P-MoCo leads to a bias in the range of MCIR and RTA. It further turned out that when adding components of cardiac motion (2D and 3D), P-MoCo cannot keep up to MCIR and RTA performance, dropping to a bias in the range of OSEM.

Also the Maximum Lesion to Background ratio (LBR_{max}) was measured that solely compares the maximum activity within a given region to the background activity. The exclusive incorporation of maximum activity clearly yields to a narrow range of LBR_{max} for respiratory motion (figure 4.8 top). Since

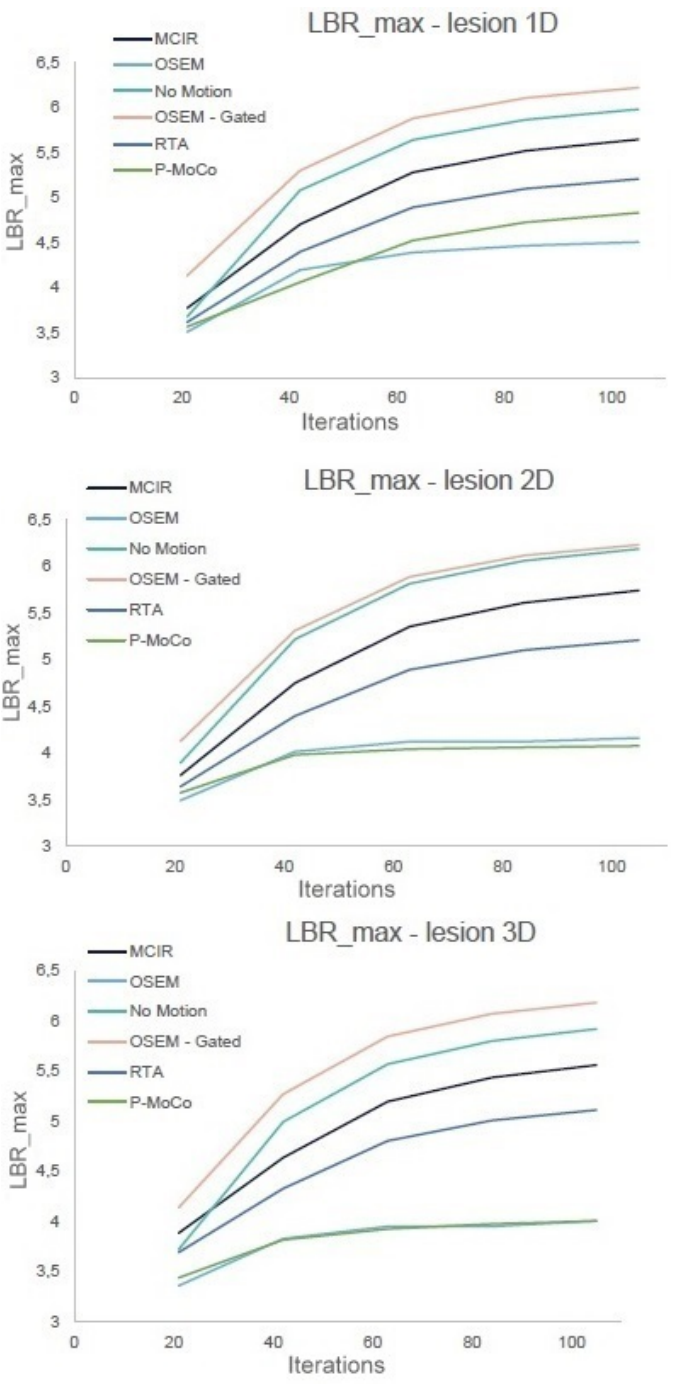

Figure 4.8: Numerical Phantom - Maximum Lesion to Background (LBR_{max}) for 1D, 2D and 3D movement of OSEM, RTA, MCIR, P-MoCo, Gated and No-Motion

OSEM is afflicted with fluctuations, it seems, that the performance for respiratory motion is higher, than it actually is (compare to figure 4.9 top left). Nevertheless, by increasing motion complexity to a mixture of respiratory and cardiac motion (2D and 3D motion), LBR_{max} for P-MoCo is comparable to the one of OSEM (figure 4.8).

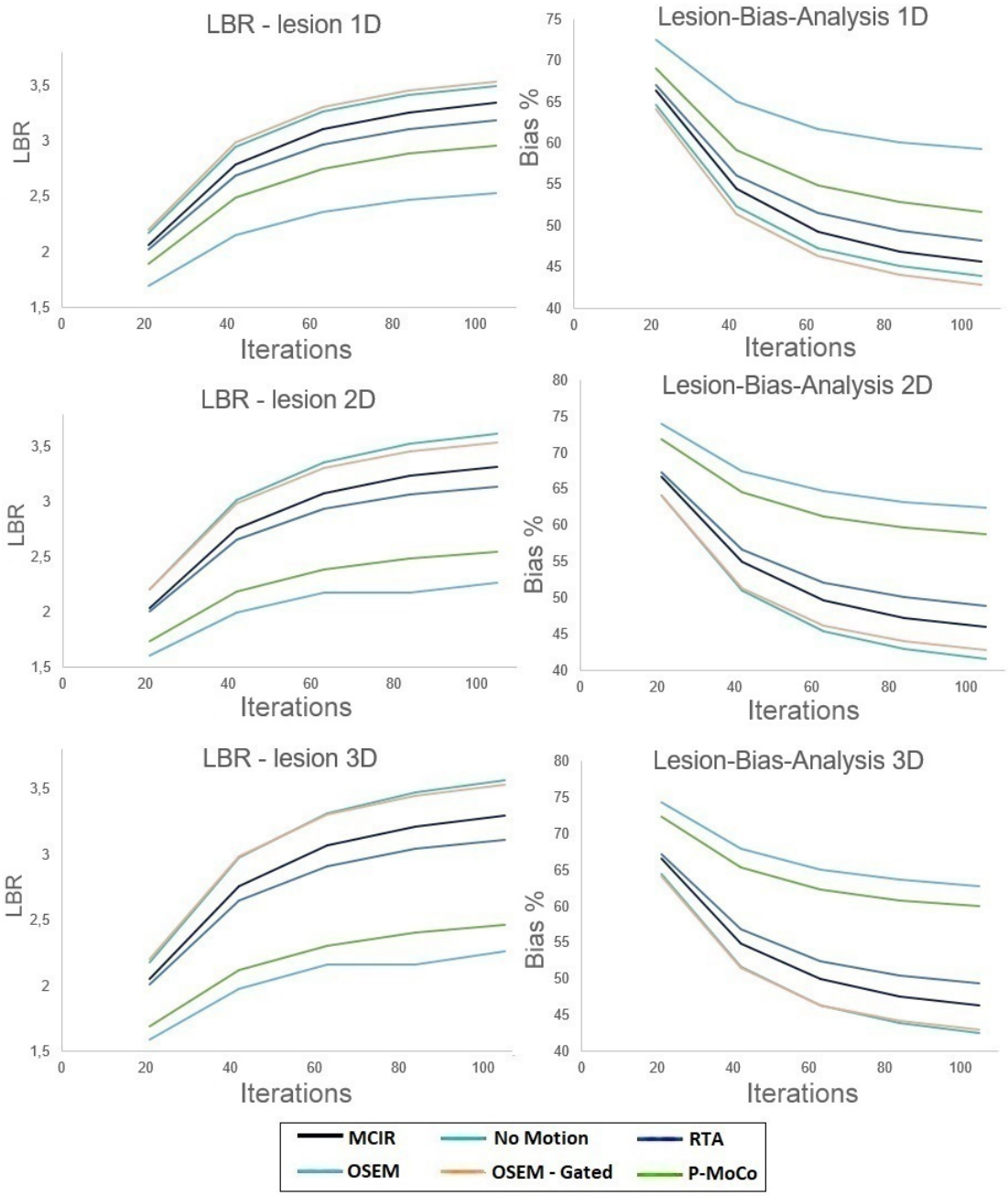

Figure 4.9: Numerical Phantom - Lesion to Background and Bias analysis for 1D, 2D and 3D movement of OSEM, RTA, MCIR, P-MoCo, Gated and No-Motion

4.2.3 Stability Analysis

A direct comparison of the performance of P-MoCo, MCIR and RTA throughout the full range of motion complexity (1D-3D) can be seen in figure 4.10. The left plot illustrates LBR for hot lesions only, the right illustrates LBR for myocardium only.

When analysing the performance of motion compensation of small hot lesions, e.g.

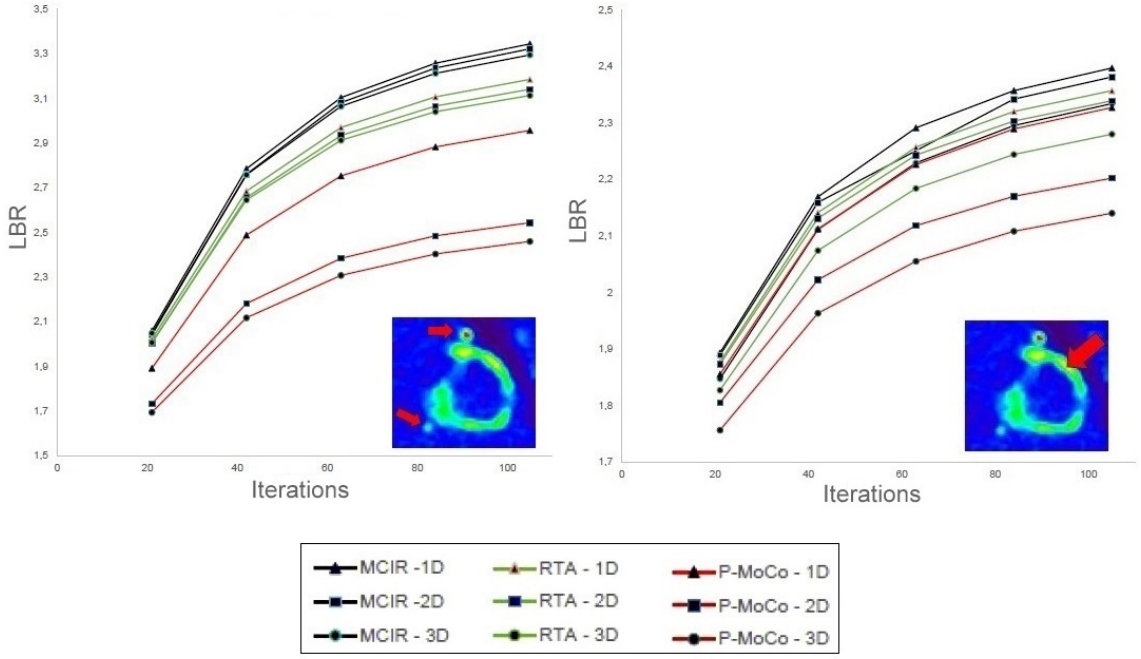

Figure 4.10: Numerical Phantom - Comparison of stability of Lesion to Background (LBR) of RTA, MCIR and P-MoCo for Lesion and Myocardium with 1D, 2D and 3D movement

solely lesion-reconstruction, MCIR and RTA reconstructions yield stable image quality in the lesion region for cardiac and respiratory motion. This is seen by a total difference of LBR_{1D} and LBR_{3D} of $49 \cdot 10^{-3}$ for MCIR, of $72 \cdot 10^{-3}$ for RTA but of $497 \cdot 10^{-3}$ for P-MoCo. Nevertheless, P-MoCo leads to images quality in the range of MCIR and RTA for respiratory motion (1D).

A performance breakdown was seen when focusing on small hot lesions in combination with respiratory- and cardiac motion effects. For reconstructions of the myocardium, including the same motion-inputs, slightly different results were obtained. MCIR still leads to the best image quality, but besides this, a nearly identical performance of 1D P-MoCo, 1D and 2D RTA and 3D MCIR was measured.

4.2.4 Separability Analysis

Another important measure in coronal imaging is the separability of different areas of the image associated with different levels of activity. This is of great importance when considering lesions close to the myocardium. In figure 4.11, one can see two hot lesions of different sizes near the myocardium, highlighted with 'Lesion NR. 1' and 'Lesion NR. 2' together with their corresponding Coronal Line Profiles of Myocardium Activity without motion.

Besides the sharp separation of Myocardium and Lesion areas without motion,

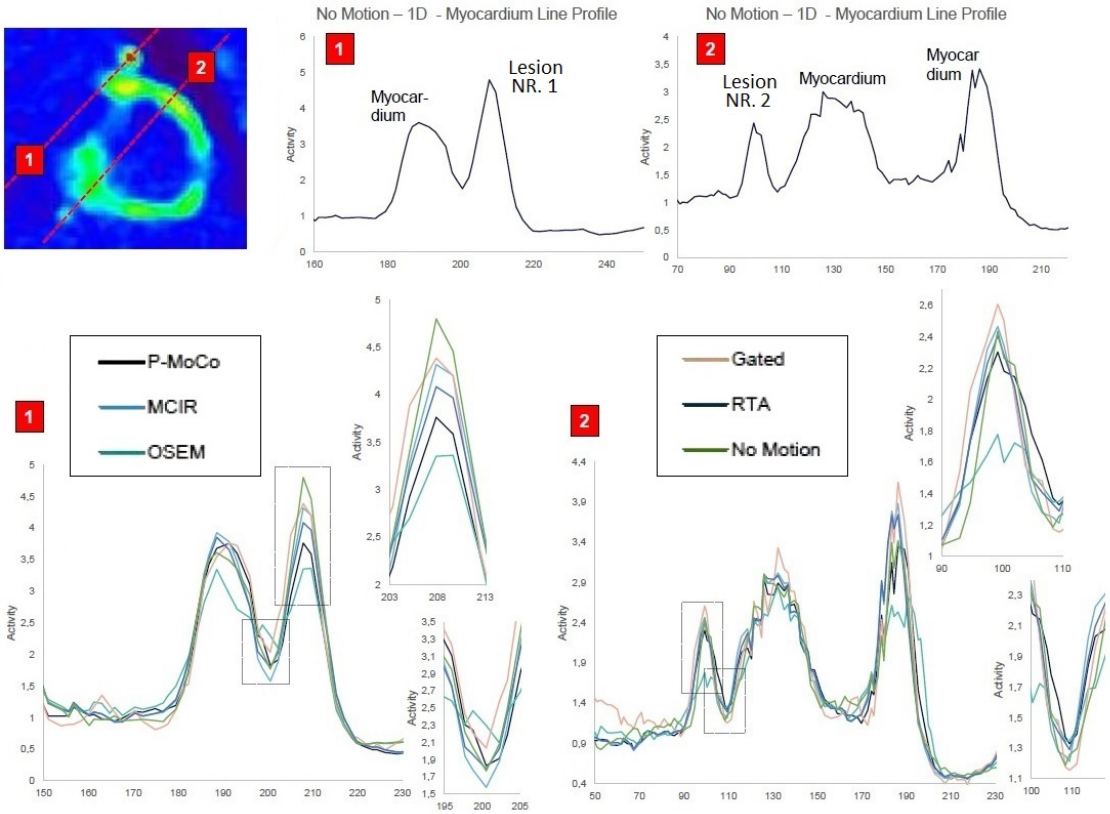

Figure 4.11: Numerical Phantom - Separability study using Myocardium Line Profiles for 1D, 2D and 3D movement of OSEM, RTA, MCIR, P-MoCo, Gated and No-Motion

MCIR gives the best separation of this areas while respiratory motion for both scales of lesion size. For big lesions, afflicted with high activity, the quality of separation of P-MoCo is comparable to the one of RTA.

4.3 Patient Data

In this section, a comparison of reconstructed images of four patient datasets is presented. In detail, a comparison of Ordered Subset Expectation Maximization (OSEM), Reconstruct-Transform-Average (RTA) and Projection-Based Motion Compensation (P-MoCo) as well as Single Gate Reconstruction (OSEM-gated) is presented (section 4.3.1). Furthermore, the performance of the different MoCo approaches is tested by means of Myocardium-to-Background analysis and noise properties (section 4.3.2).

4.3.1 Reconstructed Images

Figure 4.12 and 4.13 illustrate coronal and transversal views of the reconstructed images of patient A and patient B for the two different tracers FDG and Ammonia (NH_3).

In a first analysis step, visual inspection and comparison of the reconstructed images leads to subjective and qualitative statements, that are then, in a second analysis step, supported by the quantitative analysis of obtained Myocardium to Background Ratio and Noise Properties (for quantitative analysis see section section 4.3.2).

Figure 4.12 shows reconstructed images of patient A. One can clearly see motion artefacts in the region of the diaphragm (highlighted with a yellow arrow in figure 4.12 for the static OSEM reconstruction. A clear reduction of these artefacts can be seen, when comparing this region to P-MoCo and RTA. When analysing the myocardium definition, also a clear improvement can be seen for P-MoCo, RTA and Gated reconstructions. In terms of noise, single-gate reconstructions are afflicted with the most noise. This can clearly be seen when analysing the liver or the myocardium.

Figure 4.13 shows reconstructed images of patient number B. The yellow arrow in figure 4.13 highlights an infarcted area within the myocardium with reduced tracer uptake. When comparing the infacted region of the static OSEM reconstruction to the one of P-MoCo, RTA and Gated reconstruction, one can clearly see improvements in image quality. When analysing the overall myocardium definition, also a clear improvement can be seen for P-MoCo, RTA and Gated reconstructions. In terms of noise, single-gate reconstructions are afflicted with the most noise. This can clearly be seen when analysing the liver or the myocardium.

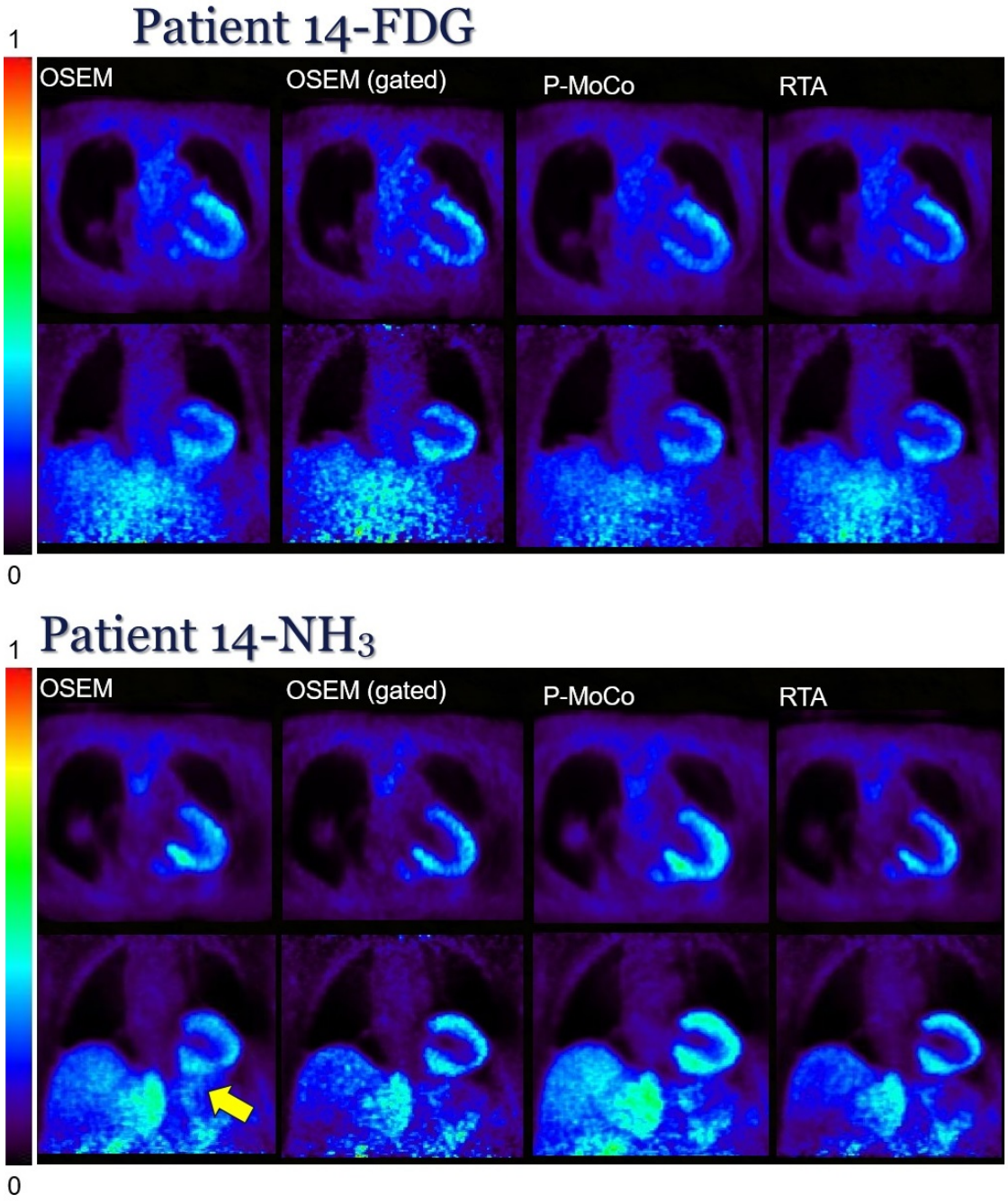

Figure 4.12: Patient A - Comparison of OSEM, RTA, P-MoCo and Gated Reconstruction for the two tracers FDG (top) and NH_3 (bottom) - The yellow arrow highlights motion artefacts in the region of the diaphragm in the static OSEM reconstruction.

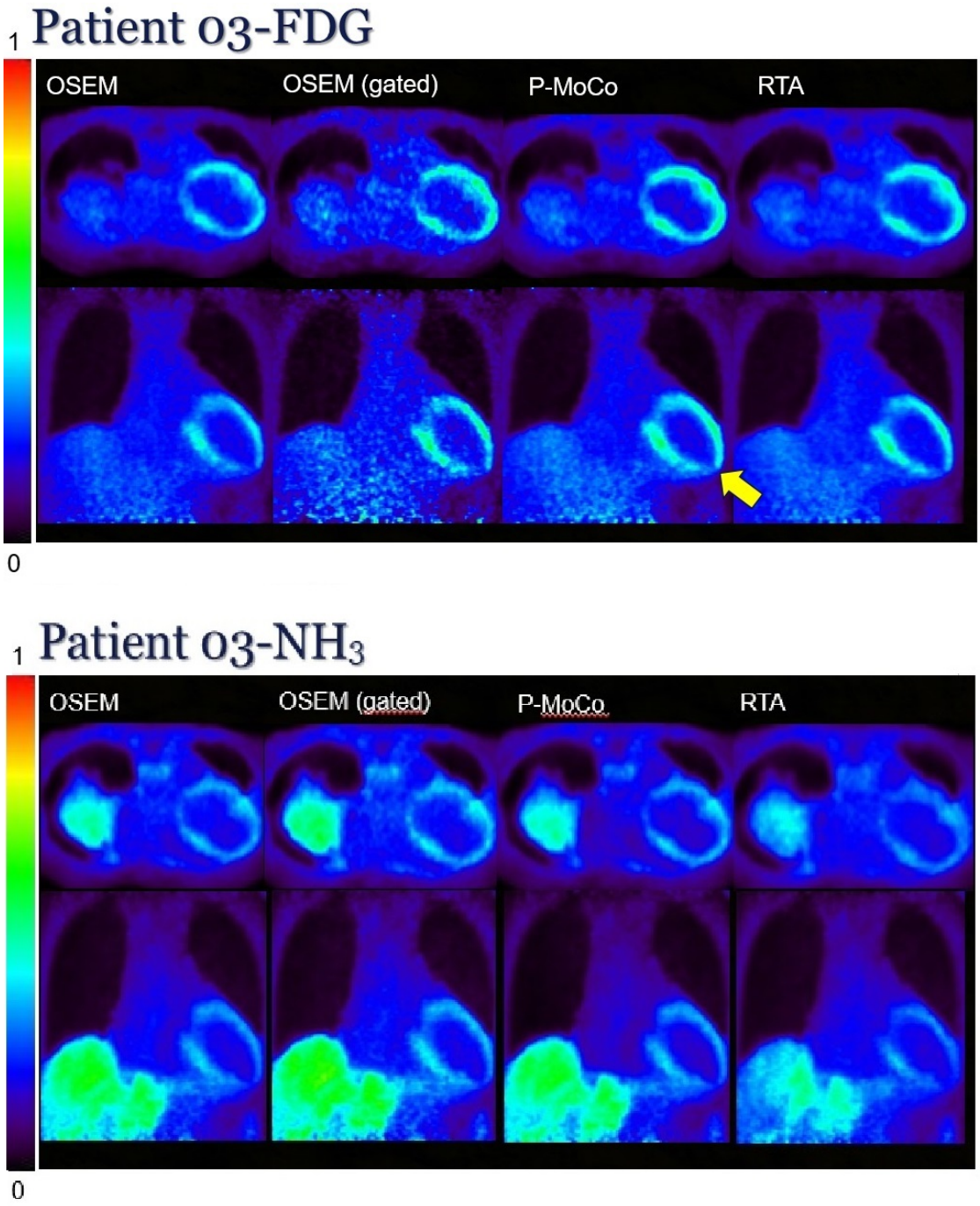

Figure 4.13: Patient B - Comparison of OSEM, RTA, P-MoCo and Gated Reconstruction for the two tracers FDG (top) and NH_3 (bottom) - The yellow arrow highlights an infarcted area within the myocardium with reduced tracer uptake for the P-MoCo image.

4.3.2 Myocardium to Background Ratio and Noise Properties

This section gives a brief overview of the quantitative analysis performed on the reconstructed images of the four patient datasets discussed in section 4.3.1. In a first step, a comparative analysis of the myocardium definition in terms of Myocardium to Background Ratio (M2B) will be performed. Further, the noise properties of the images will be analysed.

Figure 4.14 shows the Myocardium to Background (M2B) Ratio for Patient A and B for the two tracers FDG and NH_3. Besides the unsurpassed performance of Gated reconstructions for both patients and all tracers, P-MoCo and RTA lead to overall higher M2B ratios than static OSEM reconstructions for both patients and both tracers. For patient A with FDG tracer, RTA reconstructed images yield M2B ratios in the range of Gated reconstructions with a relative drop of 12.58 % M2B in the maximum iteration compared to Gated. In contrast to this, patient A including NH_3 tracer, P-MoCo yield M2B ratios in the range of Gated reconstructions with a 28.18 % drop of M2B in the maximum iteration relative to Gated (see table 4.1). In all cases static OSEM reconstructed images show clear losses of image quality, with

Table 4.1: Patient Datasets A and B - Myocardium to Background Ratio measured at the maximum iteration number of 105 iterations ($M2B_{It.NR.\ 105}$) and the respective percentage of noise measured in the image of OSEM, RTA, P-MoCo and Gated Reconstruction for FDG and NH_3 tracers

Patient/Tracer	MoCo apr.	$M2B_{It.NR.\ 105}$	Noise [%]
A/FDG	OSEM	1.22	13.2
	OSEM (Gated)	2.01	20.1
	P-MoCo	1.71	12.7
	RTA	1.91	13.0
A/NH_3	OSEM	2.51	13.3
	OSEM (Gated)	3.20	20.6
	P-MoCo	3.01	12.9
	RTA	2.77	13.9
B/FDG	OSEM	1.32	8.16
	OSEM (Gated)	1.67	11.5
	P-MoCo	1.51	9.62
	RTA	1.57	8.44
B/NH_3	OSEM	1.57	7.61
	OSEM (Gated)	2.54	13.8
	P-MoCo	2.29	8.23
	RTA	1.72	7.36

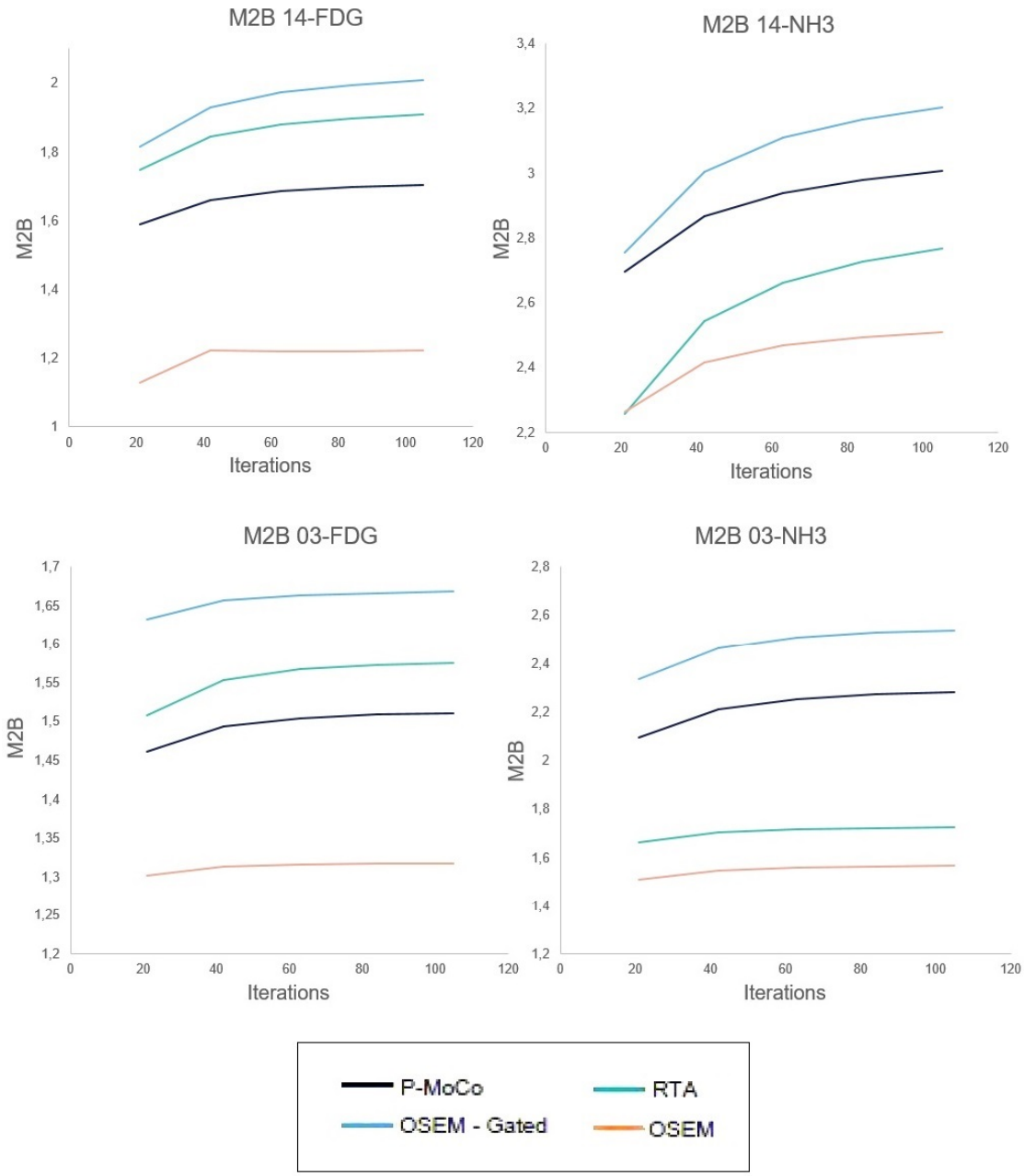

Figure 4.14: Myocardium to Background (M2B) for Patient A and B of OSEM, RTA, P-MoCo and Gated Reconstruction for FDG and NH_3 tracers

significant losses in the M2B ratios.

For patient B with FDG tracer, RTA reconstructed as well as P-MoCo reconstructed images yield M2B ratios with respective 26.49 % and 44.73 % drops of M2B in the maximum iteration compared to Gated. Patient B including NH_3 tracer, P-MoCo

yield M2B ratios in the range of Gated reconstructions with a relative drop of 26.44 % M2B in the maximum iteration compared to Gated. Again, in all cases static OSEM reconstructed images show clear losses of image quality with significant losses in the M2B ratios.

In a further analysis step, the noise properties of the images were analysed. Table 4.1 illustrates the Myocardium to Background Ratio measured at the maximum iteration number of 105 iterations ($M2B_{It.NR.\ 105}$) and the respective percentage of noise measured in the image.

Table 4.2: Patient Datasets A and B - Mean Myocardium to Background Ratio measured at the maximum iteration number of 105 iterations ($M2B_{mean}$) with corresponding standard deviation and the respective mean percentage of noise ($Noise_{mean}$) with corresponding standard deviation.

	OSEM	OSEM (Gated)	P-MoCo	RTA
$M2B_{mean}$	1.65	2.35	2.12	1.99
$M2B_{stdv}$	0.51	0.58	0.58	0.46
$Noise_{mean}$ [%]	10.5	16.3	10.9	10.7
$Noise_{stdv}$ [%]	2.72	3.77	2.01	2.83

For both patients and all tracers, single-gate reconstructions yield on average 6 % higher noise than P-MoCo, RTA and static OSEM reconstructions (see table 4.2).

5. Summary and Discussion

This chapter provides a brief summary (section 5.1) and an in-depth discussion of the results of the thesis. In detail, section 5.2 focusses on the discussion of the results related to the XCAT-Phantom, section 5.3 discusses results related to the Numerical phantom and section 5.4 provides discussion on the results related to patient data. Furthermore, a comparison of XCAT-Phantom and Numerical-Phantom is given in section 5.5. To conclude this chapter, 5.6 provides a comparison of Phantom- and Patient Data studies.

5.1 Summary of Results

The study, conducted in this thesis, focuses on the comparative evaluation of the performance and accuracy of different motion compensation techniques in PET acquisitions with simulated respiratory and cardiac motion. The main focus was set on the performance of the motion compensation approaches Ordered Subset Expectation Maximization (OSEM), Motion-Compensated Image Reconstruction (MCIR), Reconstruct-Transform-Average (RTA) and Projection-Based Motion Compensation (P-MoCo). All MoCo approaches were tested in different levels of motion complexity using XCAT phantom, that is capable of mimicking respiratory motion (1D-2D), and a numerical phantom, that is capable of mimicking respiratory and cardiac motion (1D-3D). A proof-of-concept analysis of four patient datasets completed the evaluation.

XCAT Phantom results - For the XCAT phantom, P-MoCo, MCIR and RTA yield good image quality that is comparable to Gated reconstructions and No-Motion images in terms of image contrast, noise and the blurring of the activity distribution. OSEM reconstructed images show clear losses of image quality (see figure 4.1), with significant losses in contrast and noise. This was directly validated by the comparison of the width of the line profiles of the different MoCo methods. OSEM differs up to 44 % in FWHM of the myocardium peak in the 1D line profile and up to 63 % of the myocardium peak in the 2D line profile, paired with a nearly halved maximum

activity in comparison to the other MoCo approaches. The performance of the different MoCo approaches was further tested by means of reference to different tissue types, namely lumen and liver for 1D and 2D respiratory motion (see figure 4.2 and 4.3). In this measurement set-up, image quality of MCIR surpasses the nearly identical image quality of P-MoCo and RTA. Finally, a direct comparison of the performance of P-MoCo, MCIR and RTA throughout the full range of respiratory motion complexity (1D-2D) was conducted, giving comparable absolute differences of $15 \cdot 10^{-3}$, $16 \cdot 10^{-3}$ and $19 \cdot 10^{-3}$ in terms of $M2Li_{1D}$ and $M2Li_{2D}$ for MCIR, RTA and P-MoCo.

Numerical Phantom results - For the Numerical phantom, Gated reconstructions and No-Motion images give best results in terms of noise and contrast throughout the whole motion-spectrum (1D-3D), followed by MCIR and RTA that both provide good and comparable image quality (see figures 4.5, 4.6 and 4.7). A reduction of image quality for P-MoCo was identified when increasing motion complexity. This was validated by means of $L2B$-analysis (see figure 4.9), a breakdown analysis involving $L2B_{max}$ (see figure 4.8) as well as a direct comparison to OSEM, which in all cases gives the least image quality. While the maximum activity of P-MoCo and OSEM differs significantly for 1D motion (0.6 SUV), this difference reduces drastically for 2D (0.2 SUV) and 3D motion (0.1 SUV). A total change of FWHM of up to 46 % was seen in when comparing OSEM to MCIR, RTA or P-MoCo for 1D motion. For 2D and 3D motion, this change reduces to 10 %. A bias analysis revealed that P-MoCo leads to a bias in the range of MCIR and RTA for simple 1D movement patterns but dropping to a bias in the range of OSEM for complex 2D and 3D movement. Further, stability of the MoCo approaches was tested by means of total difference of LBR_{1D} and LBR_{3D} of $49 \cdot 10^{-3}$ for MCIR, of $72 \cdot 10^{-3}$ for RTA but of $497 \cdot 10^{-3}$ for P-MoCo, that cannot be compared to the latter two MoCo approaches (see figure 4.10). Finally, performance was tested in terms of a separability analysis for two hot lesions of different sizes near the myocardium (see figure 4.11). MCIR gave the best overall separation of this areas while respiratory motion. For big lesions, afflicted with high activity, the quality of separation of P-MoCo was comparable to the one of RTA.

Patient Data results - Besides the unsurpassed performance of Gated reconstructions for both patient datasets A and B including the tracers FDG and NH_3, P-MoCo and RTA lead to an overall better image quality in terms of myocardium definition, M2B ratios as well as noise properties, than static OSEM reconstructions (see figures 4.12 and 4.13). For patient A with FDG tracer, motion artefacts in the region of the diaphragm were reduced by RTA reconstruction yielding M2B ratios in the range of Gated reconstructions with a relative drop of 12.58 % M2B in the maximum iteration compared to Gated. For patient A with NH_3 tracer, motion artefacts in the region of the diaphragm were reduced by P-MoCo yielding M2B ra-

tios in the range of Gated reconstructions with a relative drop of 28.18 % M2B in the maximum iteration compared to Gated (see figure 4.14 and table 4.1). For patient B with FDG tracer, RTA reconstructed as well as P-MoCo reconstructed images yield M2B ratios with respective 26.49 % and 44.73 % drops of M2B in the maximum iteration compared to Gated. For Patient B including NH_3 tracer, P-MoCo yield M2B ratios in the range of Gated reconstructions with a relative drop of 26.44 % M2B in the maximum iteration compared to Gated (see figure 4.14 and table 4.1). Further, noise properties of the images were analysed leading to an average noise increase of 60% in single gate reconstructions when comparing with P-MoCo, RTA and static OSEM reconstructions (see table 4.2)

5.2 Discussion of XCAT-Phantom Results

When analysing the performance of the different MoCo approaches, that can be seen in figure 4.1, it turned out that for the XCAT phantom throughout all motion-patterns and all ROIs MCIR gave best results and OSEM gave worst results. The performance of MCIR was even comparable to a static image (No Motion) that was not afflicted by motion. This has also shown to be true when solely analysing myocardium and liver or myocardium and lumen (see figure 4.2) for both simple 1D-or complex 2D-respiratory motion. These findings were expected.

As we saw by the comparison of the performance of MCIR, P-Moco and RTA for 1D and 2D respiratory motion in terms of bias analysis (see figure 4.3) and ROI analysis, we can conclude that all MoCo approaches can handle respiratory motion. Further, the comparable range of absolute difference of $15 \cdot 10^{-3}$ for RTA, $16 \cdot 10^{-3}$ and $19 \cdot 10^{-3}$ for P-MoCo in the conducted stability analysis (see figure 4.4) undoubtedly implies that MCIR, RTA and P-MoCo performance is not affected by simple 1D and complex 2D respiratory motion.

These findings suggest that P-MoCo is a good tool for respiratory motion compensation, yielding to comparable results as standard methods like MCIR or RTA.

5.3 Discussion of Numerical-Phantom Results

As expected, when analysing the performance of the different MoCo approaches, that can be seen in figure 4.5, 4.6 and 4.7, it turned out that for the Numerical phantom throughout all motion-patterns and all ROIs MCIR gave best results and OSEM gave worst results.

When the bias analysis was conducted, we realized significant impact of the motion-complexity on the performance of the different MoCo approaches. As can be seen in figure 4.8, especially for respiratory motion (1D), the image quality of P-MoCo leads to a bias in the range of MCIR and RTA. By increasing motion complexity to a mixture of complex respiratory and cardiac motion (2D and 3D motion), the bias for P-MoCo is comparable to the one of OSEM (see figure 4.9). With this observation, we were able to show that when adding components of cardiac motion (2D and 3D), P-MoCo cannot keep up to MCIR and RTA performance.

We were able to validate the observed sensitivity of P-MoCo to complex 2D and 3D cardiac motion by a stability analysis (see figure 4.10). Comparable differences of lesion-to-background ratios of $49 \cdot 10^{-3}$ for MCIR and $72 \cdot 10^{-3}$ for RTA, but of $497 \cdot 10^{-3}$ for P-MoCo were found. Therefore, it needs be stated that the P-MoCo is a good tool for respiratory motion compensation, yielding to comparable results as approved methods like MCIR or RTA, but cannot handle complex motion like a mixture of respiratory and cardiac motion.

With a separability analysis (see figure 4.11), we were able to show that MCIR gives the best separation of myocardium and lesions while respiratory motion. Especially for big lesions, afflicted with high activity, the quality of separation of P-MoCo is comparable to the one of RTA.

Further analysis of the minimum activity in the area between Myocardium and Lesion implies that P-MoCo is capable of separating small lesions in a comparable quality to MCIR, when considering solely respiratory (1D) motion.

5.4 Discussion of Patient Data Results

As expected, when analysing the performance of the different MoCo approaches, that can be seen in figures 4.12 and 4.13, it turned out that for patient A and B for both tracers FDG and NH_3, Gated reconstructions gave best results and static OSEM reconstructions gave worst results.

When the Myocardium-to-Background (M2B) ratio analysis was conducted, we realized that for both patients with FDG tracer, RTA images gave better performance than P-MoCo images. For both patients with NH_3 tracer it turned out to be the directly opposite scenario in which P-MoCo images gave better performance than RTA images (see figure 4.14). This behaviour can be explained by a higher number of breath-holding involved while ammonia-scans, compared to the amount of breath-holding while FDG scans. Furthermore, the number of counts in the different gates varied a lot. Performance losses of RTA can therefore also be explained

by the similar weighting of the RTA algorithm of all the gates, without taking the count-rate into account. At the moment, the observed trend for different tracers has no statistical relevance since only four datasets were analysed.

With an analysis of the noise properties of the reconstructed images (see tables 4.2 and 4.1), we were further able to show that single-gate reconstructions are afflicted with on average 60 % higher noise than P-MoCo, RTA and static OSEM reconstructions. Again it needs to be stressed that at the moment, this finding has limited statistical relevance since only four datasets were analysed.

Motion Compensated Image Reconstruction (MCIR) evaluations were not included in this work. The reason for not including MCIR is the occurrence of unexpected artefacts in two of the four reconstructed datasets. Nonetheless, in the cases were the MCIR worked well, we observed a similar behaviour than in the simulated phantom acquisitions, with slight superior performance of the MCIR when comparing with RTA or P-MoCo. The understanding of the origin of these artefacts and their correction is still work in progress.

5.5 Comparison of XCAT-Phantom and Numerical-Phantom

One of the primary goals of the investigations presented in this thesis was to find out how far we can increase motion complexity without impairing the performance of the Projection-Based Motion Compensation (P-MoCo) approach.

By simulating two levels of complexity of solely respiratory motion (1D and 2D) via the XCAT phantom and three levels of motion complexity via the numerical phantom, including 1D respiratory motion and complex 2D and 3D respiratory and cardiac motion, we were able to directly observe the impact of the different motion-patterns on the performance of P-MoCo and validate the findings against approved methods like MCIR or RTA.

The stability analysis of the different MoCo approaches for XCAT phantom and Numerical Phantom in all simulated motion patterns (see figures 4.4 and 4.10) gave clear insight in how far motion complexity can be increased without impairing the performance of P-MoCo. On the one hand, we showed that the absolute differences of $15 \cdot 10^{-3}$ for RTA, $16 \cdot 10^{-3}$ and $19 \cdot 10^{-3}$ for P-MoCo satisfy the stability criteria 3.15 for XCAT phantom. On the other, we showed that the absolute differences of $49 \cdot 10^{-3}$ for MCIR and $72 \cdot 10^{-3}$ for RTA satisfy the stability criteria 3.14 for Numerical phantom, but the absolute difference of $497 \cdot 10^{-3}$ for P-MoCo do not satisfy the stability criteria 3.14 for Numerical phantom.

These findings highly suggest that P-MoCo is a good tool for respiratory motion compensation, yielding to comparable results as approved methods like MCIR or RTA, but cannot handle complex motion like a mixture of respiratory and cardiac motion.

5.6 Comparison of Phantom-Data studies and Patient Data studies

In a further attempt of investigating how far we can increase motion complexity without impairing the performance of the P-MoCo approach, we analysed patient datasets.

With the Patient-Data studies, the two already existing stages of motion complexity, namely (i) solely respiratory motion (simulated with XCAT phantom) and (ii) a mixture of respiratory motion (simulated with numerical phantom), have been raised by a third stage. The reconstructed Patient Data consist of respiratory and cardiac motion, but were solely analysed with respiratory gating. Therefore patient data acts as an intermediate stage of motion complexity between XCAT phantom and numerical phantom and tops off the investigation of P-MoCo.

With the Patient-Data studies, that basically reflect the findings of the Phantom-Data studies, we were able to show that for FDG tracer, RTA images gave better performance than P-MoCo images and for NH_3 tracer P-MoCo images gave better performance than RTA images. Nevertheless, up to now, due to a low number of datasets, these findings have limited statistical relevance and more datasets need to be analysed.

These findings suggest that the P-MoCo approach is capable of reconstructing patient-data, yielding to comparable results as standard methods like RTA. According to the findings of the first datasets, the performance of P-MoCo may vary with different tracers. However, this statement is lacking statistical relevance and needs to be further investigated.

6. Conclusion and Outlook

In a general attempt of investigating how far we can increase motion complexity without impairing the performance of the data-driven Projection-Based Motion Compensation (P-MoCo) approach, we studied the performance of P-MoCo in different levels of motion complexity. By simulating different levels of motion complexity including solely 1D and 2D respiratory motion and a mix of complex 1D, 2D and 3D respiratory and cardiac motion, we were able to directly observe the impact of the different motion-patterns on the performance of P-MoCo and validate the findings against approved methods like MCIR or RTA. In a further step we studied the P-MoCo approach with real patient data. We found significant sensibility of the P-MoCo performance regarding to the prevalent motion complexity.

Final Conclusion

The findings in this paper highly suggest that P-MoCo is a good and useful tool for respiratory motion compensation, yielding to comparable results as standard methods like MCIR or RTA, but cannot handle complex motion like a mixture of respiratory and cardiac motion in two and three dimensions. Especially for hot lesions, the quality of separation of P-MoCo was found to be comparable to the one of RTA and when considering solely respiratory motion even comparable to MCIR. Finally, P-MoCo is capable of reconstructing patient-data, yielding to comparable results as approved methods like RTA. According to the findings of the first datasets, the performance of P-MoCo may vary with different tracers.

Outlook

In order to adequately cover the wide range of simulated motion complexity, the P-MoCo also needs to be tested with XCAT simulations that involve a mixture of respiratory and cardiac motion. Further, the findings of the first patient datasets suggest that the performance of P-MoCo may vary with different tracers. These findings needs to be validated using a larger number of patient datasets.

Bibliography

Akamatsu G., Ishikawa K.,Mitsumoto K., Taniguchi T., Ohya N., Baba S., Abe K. and Sasaki M. Improvement in PET/CT Image Quality with a Combination of Point-Spread Function and Time-of-Flight in Relation to Reconstruction Parameters. Journal of Nuclear Medicine, 53(11): 1716-1722, nov 2012. ISSN 0161-5505. doi: 10.2967/jnumed.112.103861. URL `http://www.ncbi.nlm.nih.gov/pubmed/22952340`

Alauddin M.M. Positron emission tomography (PET) imaging with 18F-based radiotracers. American Journal of Nuclear Medicine and Molecular Imaging. 2012

Alessio A. and Kinahan P. PET image reconstruction. In R. Henkin, editor, Nuclear medicine. 2nd edition, 2006a. URL http://faculty.washington.edu/aalessio/papers/alessioPETRecon.pdf.

Alvarez-Diez T.M., deKemp R., Beanlands R. and Vincent J. Manufacture of strontium-82 /rubidium-82 generators and quality control of rubidium-82 chloride for myocardial perfusion imaging in patients using positron emission tomography. Applied Radiation and Isotopes, 1999.

Anderson C.D. "The Positive Electron". 1933. Physical Review. 43 (6): 491–494.

Bailey D.L., Meikle S.R. A convolution-subtraction scatter correction method for 3D PET. Phys Med Biol 1994;39:411–424.

Bailey D.L., Townsend D.W., Valk P.E. and Maisey M.N. Positron Emission Tomography. Springer-Verlag, London, 2005. ISBN 1-85233-798-2. doi: 10.1007/b136169. URL http://link.springer.com/10.1007/b136169.

Barney J.S., Rogers J.G., Harrop R., Hoverath H. Object shape dependent scatter simulations for PET. IEEE Trans. Nucl. Sci. 1991;NS-38:719–725.

Bengel F.M., Higuchi T., Javadi M.S. and Lautamäki R. Cardiac Positron Emission Tomography, 2009. ISSN 07351097.

Bergmann S.R., Fox K.A., Rand A.L. et al. Quantification of regional myocardial blood flow in vivo with H215O. Circulation. 1984;70:724–733. doi: 10.1161/01.CIR.70.4.724.

Bergstrom M., Eriksson L., Bohm C., Blomqvist G., Litton J. Correction for scattered radiation in a ring detector positron camera by integral transformation of the projections. J. Comput. Assist. Tomogr. 1983;7:42–50.

Beyer T., Townsend D.W., Brun T., Kinahan P.E., Charron M., Roddy R., Jerin J., Young J., Byars L. and Nutt R. A combined PET/CT scanner for clinical oncology. J Nucl Med, 41(8):1369-1379, 2000. ISSN 0161-5505. URL `http://www.ncbi.nlm.nih.gov/pubmed/10945530.`

Beyer T., Townsend D., Czernin J., Freudenberg L. (2011). The future of hybrid imaging—part 2: PET/CT. Insights into imaging. 2. 225-34. 10.1007/s13244-011-0069-4.

Birks J.B. The Theory and Practice of Scintillation Counting. Pergamon Press, Oxford. 1964. eBook ISBN: 9781483156064

Cabello J, Ziegler SI. Advances in PET/MR instrumentation and image reconstruction. Br J Radiol. 2016;89. doi:10.1259/bjr.20160363.

Cal-González J. Positron range and prompt gamma modelling in PET imaging, 2014. URL http://www.tdx.cat/handle/10803/356552.

Cal-González J., Tsoumpas C., Lassen M.L., Rasul S., Koller L., Hacker M., Schäfers K. and Beyer T. "Impact of motion compensation and partial volume correction for 18F-NaF PET/CT imaging of coronary plaque," Phys. Med. Biol., vol. 63, no. 1, p. 15005, 2017.

Catana C. (2015). Motion correction options in PET/MRI. Seminars in Nuclear Medicine. 45. 10.1053/j.semnuclmed.2015.01.001.

Cherry S.R., Meikle S.R., Hoffman E.J. Correction and characterization of scattered events in three-dimensional PET using scanners with retractable septa. J. Nucl. Med. 1993;34:671–678.

Cherry S.R., HuangS.C. Effects of scatter on model parameter estimates in 3D PET studies of the human brain. IEEE Trans Nucl Sci 1995;NS-42:1174–1179.

Conti M. Focus on time-of-flight PET: the benefits of improved time resolution. Eur J Nucl Med Mol Imaging. 2011;38(6):1147-1157. doi:10.1007/s00259-010-1711-y.

Crowe M.E, Larson A.C., Zhang Q. et al. Automated rectilinear self-gated cardiac cine imaging. Magn Reson Med. 2004;52:782–788.

Dawood M., Buther F., Lang N. et al. Respiratory gating in positron emission tomography: a quantitative comparison of different gating schemes. Med Phys. 2007;34:3067–3076.

Degenhardt C, Prescher G, Frach T, et al. The digital silicon photomultiplier - A novel sensor for the detection of scintillation light. IEEE Nucl Sci Symp Conf Rec. 2009:2383-2386. doi:10.1109/NSSMIC.2009.5402190.

Dirac P.A.M. "The quantum theory of the electron". 1928. Proceedings of the Royal Society A. 117 (778): 610.

Feng T., Wang J., Fung G., Tsui B. Non-rigid dual respiratory and cardiac motion correction methods after, during, and before image reconstruction for 4D cardiac PET. Phys Med Biol. 2016;61(1):151-168. doi:10.1088/0031-9155/61/1/151.

Fermi E., "Versuch einer Theorie der β-Strahlen". Zeitschrift für Physik, Volume 88, Issue 3-4, pp. 161-177; 1934. doi: 10.1007/BF01351864

Frach T, Prescher G, Degenhardt C, De Gruyter R, Schmitz A, Ballizany R. The digital silicon photomultiplier - Principle of operation and intrinsic detector performance. IEEE Nucl Sci Symp Conf Rec. 2009:1959-1965. doi:10.1109/NSSMIC.2009.5402143.

Gillman A., Rose S., Smith J., Thomas P., Dowson N. PET motion correction in context of integrated PET/MR: current techniques, limitations, and future projections. Med Phys. 2017. doi:10.1002/mp.12577.

Goertzen AL, Bao Q, Bergeron M et al. NEMA NU 4-2008 Comparison of Preclinical PET Imaging Systems. Journal of nuclear medicine: official publication, Society of Nuclear Medicine. 2012. 53(8):1300-1309. doi:10.2967/jnumed.111.099382.

Gopal B.S., Basics of PET Imaging - Physics, Chemistry, and Regulations. 2010. Springer-Verlag New York. DOI: 10.1007/978-1-4419-0805-6

Green 1990a P.J. Bayesian reconstructions from emission tomography data using a modified EM algorithm. IEEE Trans. Med. Imaging 9. 84–93

Green 1990b P.J. On use of the EM algorithm for penalized likelihood estimation R. Stat. Soc. 52. 443–52

Grupen C. Introduction to Radiation Protection. Practical Knowledge for Handling Radioactive Sources. Springer-Verlag Berlin Heidelberg (2010). ISBN 978-3-642-02585-3. DOI 10.1007/978-3-642-02586-0

Harrison R.L, Haynor D.R., Lewellen T.K. Dual energy window scatter corrections for positron emission tomography. In: Conference Record of the 1991 IEEE Nuclear Science Symposium and Medical Imaging Conference; 1991; Santa Fe, NM: IEEE; 1991. p. 1700–1704.

Hasegawa T., Tanaka E., Yamashita T., Watanabe M., Yamaya T., Murayama H. A Monte Carlo simulation study on coarse septa for scatter correction in 3-D PET. IEEE Trans Nucl Sci 2002;49(5):2133–2138.

Hoh C.K. Clinical use of FDG PET. Nuclear Medicine and Biology, 34:737–742, 2007.

Hubbel J.H. "Photon Cross Sections, Attenuation Coefficients, and Energy Absorption Coefficients from 10 keV to 100 GeV; 'National Bureau of Standads report NSRDS-NSB 29 (August 1969)

Hudson H.M., Larkin R.S. Accelerated image reconstruction using ordered subsets of projection data. IEEE Trans Med Imaging. 1994;13(4):601-609. doi:10.1109/42.363108.

Jadvar H., Parker J.A. Clinical PET and PET/CT. Springer-Verlag London. 2005. DOI 10.1007/b138777. ISBN 978-1-85233-838-1

Jani S.S., Robinson C.G., Dahlbom M. et al. A Comparison of Amplitude-based and Phase-based Positron Emission Tomography Gating Algorithms for Segmentation of Internal Target Volumes of Tumors Subject to Respiratory Motion. International journal of radiation oncology, biology, physics. 2013;87(3):562-569. doi:10.1016/j.ijrobp.2013.06.2042.

Judenhofer M.S., Wehrl H.F., Newport D.F. et al. Simultaneous PET-MRI: a new approach for functional and morphological imaging, Nat Med. 2008;14(4):459-465.

Kesner A.L., Schleyer P.J., Büther F., Walter M.A., Schäfers K.P., KooP.J. On transcending the impasse of respiratory motion correction applications in routine clinical imaging – a consideration of a fully automated data driven motion control framework. EJNMMI Phys. 2014;1(1):8. doi:10.1186/2197-7364-1-8.

Kinahan P.E., Townsend D.W., Beyer T. and Sashin D. Attenuation correction for a combined 3D PET/CT scanner. Med. Phys., 25:20462053, 1998.

Kolbitsch C., Ahlman M.A., Venn C.D. et al. Cardiac and respiratory motion correction for simultaneous cardiac PET - MR. J Nucl Med. 2017;Epub ahead. doi:10.2967/jnumed.115.171728.

Konya J., Nagy N.M. Nuclear and Radio-chemistry. 2012. Elsevier. pp. 74–75. ISBN 978-0-12-391487-3.

Krane K.S. Introductory Nuclear Physics. John Wiley and Sons, 1988. ISBN 047180553X.

Kuhle W.G., Porenta G., Huang S.C., Buxton D., Gambhir S.S., Hansen H., Phelps M.E. and Schelbert H.R. Quantification of regional myocardial blood flow using 13N ammonia and reoriented dynamic positron emission tomographic imaging. Circulation, 1992.

Ladefoged C.N., Law I., Anazodo U. et al. A multi-centre evaluation of eleven clinically feasible brain PET/MRI attenuation correction techniques using a large cohort of patients. Neuroimage. 2017;147:346-359.

Larson A.C., White R.D., Laub G., McVeigh E.R., Li D., Simonetti O.P. 2004. Self-gated cardiac cine MRI. Magn. Reson. Med., 51: 93–102. doi:10.1002/mrm.10664

Lassen M.L., Cal-Gonzalez J., Hacker M. and Beyer T. 2015 Markerless motion correction of myocardial plaque scans using [18F]-FDG PET improves spatial outline of hot-spots, J Nucl Med 56: S3, 1816.

Lassen M.L., Rasul S., Beitzke D., Stelzmüller ME, Cal-Gonzalez J., Hacker M., Beyer T. 2017. Assessment of attenuation correction for myocardial PET imaging using combined PET/MRI. Journal of Nuclear Cardiology. https://doi.org/10.1007/s12350-017-1118-2

Lassen M.L., Beyer T., Beitzke D., Büther F., Hacker M., Rasul F., Schäfers K. and Cal-González J. Evaluation of a data-driven, projection-based respiratory motion compensation of PET data. 2018. In preparation for the Journal of Nuclear Medicine

Liu C., Pierce L.A., Alessio A.M., Kinahan P.E. The impact of respiratory motion on tumor quantification and delineation in static PET/CT imaging, Phys. Med. Biol. 54 (2009) 7345–7362.

Livieratos L., Stegger L., Bloomfield P.M., Schafers K., Bailey D.L., Camici G. Rigid-body transformation of list-mode projection data for respiratory motion correction in cardiac PET. Phys Med Biol. 2005;50(14):3313-3322. doi:10.1109/NSSMIC.2003.1352313.

Lucignani G., Paganelli G., Bombardieri E. (2004). "The use of standardized uptake values for assessing FDG uptake with PET in oncology: A clinical perspective". Nuclear Medicine Communications. 25 (7): 651–656. doi:10.1097/01.mnm.0000134329.30912.49. PMID 15208491.

Maddahi J., Packard R.B.S. Cardiac PET Perfusion Tracers: Current Status and Future Directions. Seminars in nuclear medicine. 2014;44(5):333-343. doi:10.1053/j.semnuclmed.2014.06.011.

McClelland J.R., Hawkes D.J., Schaeffter T. et al. Respiratory motion models: A review. Med Image Anal. 2013;17:19–42. `https://www.ncbi.nlm.nih.gov/pubmed/23123330`

McRobbie D.W. 2007. MRI from picture to proton. Cambridge, UK; New York: Cambridge University Press. ISBN 0-521-68384-X.

Mehranian A., Arabi H., Zaidi H. Vision 20/20: Magnetic resonance imaging-guided attenuation correction in PET/MRI: Challenges, solutions, and opportunities. Med Phys. 2016;43(3):1130-1155.

Munoz C., Kolbitsch C., Reader A.J., Marsden P., Schaeffter T., Prieto C. MR-Based Cardiac and Respiratory Motion-Compensation Techniques for PET-MR Imaging. PET Clin. 2016;11(2):179-191. doi:10.1016/j.cpet.2015.09.004.

Muzic R.F., DiFilippo F.P. PET/MRI – Technical Review. Seminars in roentgenology. 2014;49(3):242-254. doi:10.1053/j.ro.2014.10.001.

Myronenko A. and Song X. 2010. Intensity-based image registration by minimizing residual complexity IEEE Trans. Med. Imaging. 29. 1882–91

Nehmeh S.A., Erdi Y.E. Respiratory Motion in Positron Emission Tomography/Computed Tomography: A Review. Semin Nucl Med. 2008;38(3):167-176. doi:10.1053/j.semnuclmed.2008.01.002.

National Institute of Standards and Technology: `http://www.nist.gov/`. Accessed Mar. 2018.

Otte N., Dolgoshein B., Hose J., Klemin S., Lorenz E., Mirzoyan R., Popova E., Teshima M. The SiPM — A new Photon Detector for PET. Nuclear Physics B - Proceedings Supplements, Volume 150, 2006, Pages 417-420. ISSN 0920-5632. URL: `https://doi.org/10.1016/j.nuclphysbps.2004.08.048.`

Ouyang J., Li Q., El Fakhri G., Magnetic Resonance-Based Motion Correction for Positron Emission Tomography Imaging, Semin. Nucl. Med. 43 (2013) 60–67.

Pepin A., Daouk J., Bailly P. et al. Management of respiratory motion in PET/computed tomography: the state of the art. Nucl Med Commun. 2014;35:113–122. [PMC free article]

Phelps M.E., Hoffman E.J., Mullani N.A. and Ter-Pogossian M.M. Application of annihilation coincidence detection to transaxial reconstruction tomography. Journal of nuclear medicine : official publication, Society of Nuclear Medicine, 16(3):210-224, 1975. ISSN 0161-5505.

Piatek S. A technical guide to silicon photomultipliers (SiPM). webpage of company Hamamatsu. URL: `https://www.hamamatsu.com/us/en/community/optical_sensors/articles/technical_guide_to_silicon_photomultipliers_sipm/index.html` Accessed Mar. 2018.

Picard T.C.J. Motion correction of PET images using multiple acquisition frames. IEEE Trans Med Imaging. 1997;16(2):137-144.

Pichler B.J., Judenhofer M.S., Catana C. et al. Performance test of an LSO-APD detector in a 7-T MRI scanner for simultaneous PET/MRI. J Nucl Med. 2006;47(4):639-647.

Polycarpou I., Tsoumpas C., Marsden P.K. Analysis and comparison of two methods for motion correction in PET imaging. Med Phys. 2012;39(10):6474. doi:10.1118/1.4754586.

Rahmim A., Bloomfield P., Houle S., Lenox M., Michel C., Buckley K.R., Ruth T.J., Sossi V. Motion Compensation in Histogram-Mode and List-Mode EM Reconstructions: Beyond the Event-Driven Approach. 2004. IEEE TRANSACTIONS ON NUCLEAR SCIENCE, VOL. 51, NO. 5. URL: `http://pages.jh.edu/~rahmim/research_work/MotionPaperFinal.pdf`

Rahmim A., Tang J., Zaidi H. Four-Dimensional Image Reconstruction Strategies in Cardiac-Gated and Respiratory-Gated PET Imaging. PET Clin. 2013;8(1):51-67. doi:10.1016/j.cpet.2012.10.005.

Rausch I., Quick H.H., Cal-Gonzalez J., Sattler B., Boellaard R., Beyer T. Technical and instrumentational foundations of PET/MRI. Eur J Radiol. 2017;94.

Schlemmer H.P.W., Pichler B.J., Schmand M., Burbar Z., Michel C., Ladebeck R., Jattke K., Townsend D., Nahmias C., Jacob P.K., Heiss W.D. and Claussen C.D. Simultaneous MR/PET imaging of the human brain: feasibility study. Radiology, 2008. 248(3):1028-1035, 2008. ISSN 0033-8419. doi: 10.1148/radiol.2483071927.

Scott A.D., Keegan J., Firmin D.N. Motion in Cardiovascular MR Imaging. Radiology. 2009;250:331–351.

Segars W.P., Sturgeon G., Mendonca S., Grimes J., Tsui B.M.W. 4D XCAT phantom for multimodality imaging research. Medical Physics. 2010;37(9):4902-4915. doi:10.1118/1.3480985.

Sengupta P.P., Korinek J., Belohlavek M. et al. (2006) Left Ventricular Structure and Function: Basic Science for Cardiac Imaging. Journal of the American College of Cardiology, 48, 1988-2001. http://dx.doi.org/10.1016/j.jacc.2006.08.030

Shepp L.A., Vardi Y. Maximum Likelihood Reconstruction for Emission Tomography. IEEE Trans Med Imaging. 1982;1(2):113-122.

Sonzogni A. NuDat2, 2016. URL http://www.nndc.bnl.gov/nudat2/.

Surti S. Update on Time-of-Flight PET Imaging. Journal of Nuclear Medicine, 56(1):98-105, jan 2015. ISSN 0161-5505. doi: 10.2967/jnumed.114.145029.

Surti S, Karp JS. Advances in time-of-flight PET. Phys Medica. 2016;32(1):12-22. doi:10.1016/j.ejmp.2015.12.007.

Tai Y.F. and Piccini P. Applications of positron emission tomography (PET) in neurology. Journal of neurology, neurosurgery, and psychiatry, 75(5):669-676, 2004. ISSN 0022-3050. doi: http://dx.doi. org/10.1136/jnnp.2003.028175. URL http://15090557.

Ter-Pogossian M.M, Phelps M.E., Hoffman E.J. and Mullani N.A. *A positron-emission transaxial tomograph for nuclear imaging (PETT).* Radiology, 114(5):89-98, 1975. ISSN 0033-8419. doi: 10.1148/114.1.89.

Thielemans K., Tsoumpas C., Mustafovic S., Beisel T., Aguiar P.,Dikaios N. and Jacobson M.W.. 2012. STIR: software for tomographic image reconstruction release 2. Phys. Med. Biol. 57. 867

Thompson C.J. The problem of scatter correction in positron volume imaging. IEEE Trans Med Imaging 1993;MI-12:124–132.

Townsend D.W., Beyer T., Blodgett T.M. PET/CT scanners: A hardware approach to image fusion. Semin Nucl Med. 2003;33(3):193-204. doi:10.1053/snuc.2003.127314.

Tsoumpas C., Buerger C., Mollet P. and Marsden P.K. "Fast analytic simulation toolkit for generation of 4D PET-MR data from real dynamic MR acquisitions," in Journal of Physics: Conference Series, 2011, vol. 317, no. 1, p. 12020.

Tsoumpas C, Buerger C, King A P, et al. 2011a Fast generation of 4D PET-MR data from real dynamic MR acquisitions Phys. Med. Biol. 56 6597–613

Tsoumpas C., Polycarpou I., Thielemans K., Buerger C., King A.P., Schaeffter T. and Marsden P.K. 2013. The effect of regularization in motion compensated PET image reconstruction: a realistic numerical 4D simulation study. Phys. Med. Biol. 58. 1759–73

Uribe S., Muthurangu V., Boubertakh R. et al. Whole-heart cine MRI using real-time respiratory self-gating. Magn Reson Med. 2007;57:606–613.

Vandenberghe S, Mikhaylova E, D'Hoe E, Mollet P, Karp JS. Recent developments in time-of-flight PET. EJNMMI Phys. 2016;3(1):3. doi:10.1186/s40658-016-0138-3.

Vandenberghe S, Mikhaylova E, D'Hoe E, Mollet P, Karp JS. Recent developments in time-of-flight PET. EJNMMI Phys. 2016;3(1):3. doi:10.1186/s40658-016-0138-3.

Watson C.C. 2000 New, faster, image-based scatter correction for 3D PET IEEE Trans. Nucl. Sci. 47 1587–94

Webb P.P., McIntyre R.J. and Conradi J. Properties of avalanche photodiodes. RCA Rev, 1974.

Wikimedia Commons, 2018. URL https://de.wikipedia.org/wiki/Datei:APD3_German.png

Williams W.S.C. 1991. Nuclear and Particle Physics. Clarendon Press, Oxford (UK), ISBN 0-19-852046-8